

THE LOCAL PILE OSCILLATOR  
AS A DEVICE FOR MEASURING TEMPERATURE DEPENDENCE  
IN EPITHERMAL-NEUTRON ABSORPTION

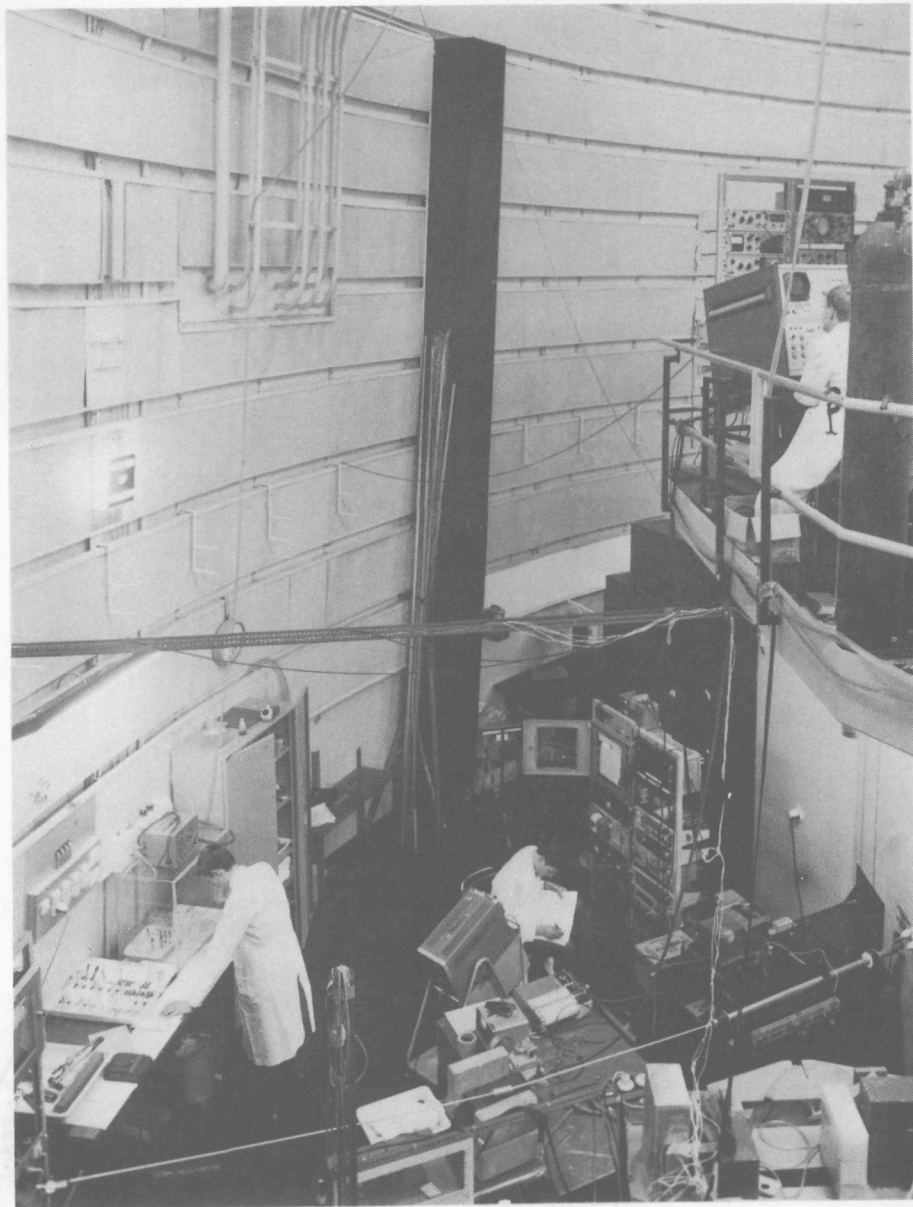


Fig. a  
Local pile oscillator in the reactor hall

THE LOCAL PILE OSCILLATOR  
AS A DEVICE FOR MEASURING TEMPERATURE DEPENDENCE  
IN EPITHERMAL-NEUTRON ABSORPTION

PROEFSCHRIFT

TER VERKRIJGING VAN DE GRAAD VAN DOCTOR IN DE  
TECHNISCHE WETENSCHAPPEN AAN DE TECHNISCHE  
HOGESCHOOL DELFT, OP GEZAG VAN DE RECTOR  
MAGNIFICUS DR. IR. C. J. D. M. VERHAGEN, HOOGLERAAR  
IN DE AFDELING DER TECHNISCHE NATUURKUNDE,  
VOOR EEN COMMISSIE UIT DE SENAAT TE VERDEDIGEN  
OP WOENSDAG 9 JULI 1969  
TE 16 UUR

DOOR

ARIJ LEENDERT DEKKER  
NATUURKUNDIG INGENIEUR  
GEBOREN TE DORDRECHT

1969

DELFTSCHE UITGEVERS MAATSCHAPPIJ N.V. DELFT



7204 7341

69-007018

DIT PROEFSCHRIFT IS GOEDGEKEURD DOOR DE PROMOTOR  
PROF. DR. J. J. WENT.



*Dat komt door de trillingen in de eh... dinges.  
Vat je, makker?*

Terpen Tijn



## CONTENTS

1. GENERAL INTRODUCTION	11
1.1. Motivation of the work	11
1.2. Existing experimental methods	14
1.3. Outline of the following chapters	15
2. EXPERIMENTAL METHODS AND EQUIPMENT	17
2.1. Description of the local pile oscillator	17
2.1.1. Neutron detector	19
2.1.2. Definition of measured quantities	22
2.1.3. Technical data	24
2.1.3.1. Oscillator drive and sample housing	24
2.1.3.2. Signal flow	25
2.1.3.3. Switching logic	27
2.1.3.4. Oven construction and temperature regulation	28
2.2. Corrections to be applied to the measurements	31
2.2.1. Empty-oven correction	31
2.2.2. Slowing down correction	32
2.3. Determination of the effective cadmium boundary	34
2.4. Determination of the epithermal spectrum along the axis of the oscillator channel	36
2.4.1. Strip activation	36
2.4.2. Single foils	37
2.4.3. The plural foil	40
3. CALIBRATION OF THE EPITHERMAL LOCAL PILE OSCILLATOR	43
3.1. Introduction	43
3.2. Standard samples used for testing	44
3.2.1. Type of the standard samples	44
3.2.2. Shape of the standard samples	44
3.3. Determination of the resonance integrals of the standard samples	44
3.3.1. Description of the activation method	44
3.3.2. Chemical separation	46
3.3.3. Measurement of the activity	46
3.4. Oscillator test	46
3.5. Results	47
3.5.1. Resonance integrals	47
3.5.2. Oscillator testing	48
3.6. Conclusion	49

4. CALCULATION METHODS	51
4.1. ERIC-II and ZUT	52
4.1.1. The ERIDEL-code	58
4.2. The RIFF RAFF'-code	61
4.3. Comparison of the codes	63
4.3.1. Discussion of some special computation results	63
4.3.2. Temperature dependence	66
4.3.2.1. ERIDEL temperature dependence	66
4.3.2.2. RIFF RAFF' temperature dependence	67
5. CALCULATIONS OF RESONANCE INTEGRALS AND DOPPLER COEFFICIENTS; COMPARISON WITH REFERENCE VALUES	71
5.1. Materials and rod-dimensions which have been considered	71
5.2. Resonance integrals and Doppler coefficients for uranium, uraniumdioxide and thorium	72
5.2.1. Application of the codes	72
5.2.2. Input data	74
5.2.3. Room-temperature resonance integrals	75
5.2.4. Doppler coefficients	78
5.3. Error margins	83
5.3.1. Resonance integrals at room temperature	83
5.3.2. Doppler coefficients	87
5.3.3. The influence of a non-zero Debije temperature	87
6. COMPARISON BETWEEN COMPUTATION RESULTS AND LOCAL OSCILLATOR MEASUREMENTS	91
6.1. Computation of chamber integrals and temperature coefficients	91
6.2. Thermal expansion effect	93
6.3. Room temperature chamber integrals	94
6.4. Temperature dependence	96
6.4.1. Natural uranium	96
6.4.2. Thorium	98
6.4.3. Uraniumdioxide	99
6.5. Some controls	101
6.5.1. The connection between leakage and absorption	102
6.5.2. On possible electronical errors	103
6.5.3. On possible anisotropy effects	104
6.6. Discussion of the results and conclusions	104
6.7. Possible future work	105

APPENDIX	109
REFERENCES	113
LIST OF ABBREVIATIONS	117
SUMMARY	119
SAMENVATTING (DUTCH SUMMARY)	123
ACKNOWLEDGEMENTS	127
LIST OF SYMBOLS	



CHAPTER 1 GENERAL INTRODUCTION

1.1. *Motivation of the work*

At the International Conference on Fast Critical Experiments and Their Analysis, held at the Argonne National Laboratory, U.S.A., October 1966, Table 1.1 was published in a paper by W.G. Davey (7).

Table 1.1. Comparative study of calculated Doppler effects of  $^{238}\text{U}$  and  $^{239}\text{Pu}$  in ZPR III Assembly 48, Oct. 1966 (from 7)

Organisation	k for $^{238}\text{U}$ Reactivity Doppler (300°K-1100°K) $\times 10^6$	k for $^{239}\text{Pu}$ Reactivity Doppler (300°K-1100°K) $\times 10^6$	change in $^{238}\text{U}$ - Activation Doppler (300°K-750°K) %
AEEW FD 2	-3.15		
AEEW Adjusted			
AI	-4.8	+1.04	
ANL	-5.16	+2.90	
APDA	-4.9	+3.7	
BNWL			+4.0
B & W			
Cadarache (H-R)			
Cadarache (USSR)			+3.3
Cadarache (25GRP)	-6.1	+7.7	+3.4
GE	-4.1	+0.58	+3.4
Karlsruhe	-3.22	+4.69	
LASL(H-R)			
LASL(USSR)			
W			
Experiment (a)	-4.9±0.2	-1.3±0.1	

(a) Not corrected for expansion effects

This table contains the results which an international group of leading research establishments got from their independent calculations of the *Doppler effects* of certain samples in the ANL ZPR-3 assembly 48, "a plutonium-fueled, soft-spectrum, simple geometry critical assembly, with a neutron spectrum similar to that of proposed fast power reactors". This *Doppler effect* concerns the influence on the reactivity of a nuclear reactor originated by the temperature dependence of neutron reaction rates. The effect is quite important as it is the only *prompt* phenomenon following a sudden temperature change which occurs in the fuel of the reactor core. A negative total Doppler effect is essential for the inherent safety of a fast reactor, and therefore the effect must be properly known before the reactor is constructed. That this knowledge is problematic follows from Table 1.1 for  $^{238}\text{U}$  and  $^{239}\text{Pu}$ . A similar situation exists for other fertile and fissionable isotopes as  $^{232}\text{Th}$ ,  $^{233}\text{U}$ ,  $^{235}\text{U}$  and other Pu-isotopes.

The temperature dependence of the neutron reaction rates is caused by the resonance structure (Fig. 1.1) which the cross-sections of the majority of heavy nuclides exhibit in the resonance region ( $\sim 1$  eV -  $\sim 50$  keV). At elevated temperatures the resonances seem to broaden (due to thermal motion of the absorber atoms) and neutron capture as well as scattering and fission, if any, increase as a result of decreased self-shielding.

The calculation of neutron reaction rates in the resonance region, and even more of the temperature dependence thereof, is a matter of study due to the complicated cross-section structures. The problem, essential for fast reactors, does occur in thermal reactor computations too. Here the resonance escape probability  $p$  is involved, which  $p$  represents the probability for a neutron to escape parasitic absorption during the moderation process. Temperature dependence is again present, but is less important for the reactor safety in view of a much longer prompt-neutron generation time ( $\sim 10^{-3}$  s as compared with  $\sim 10^{-7}$  s in fast reactors). Therefore in thermal reactors sudden large reactivity increases followed by a temperature rise of the fuel are also controlled by the generally large, but slow-operating, negative temperature coefficient due to moderator expansion. Yet a number of parallels exist between fast and thermal work in theoretical and experimental investigations on the subject of resonance absorption.

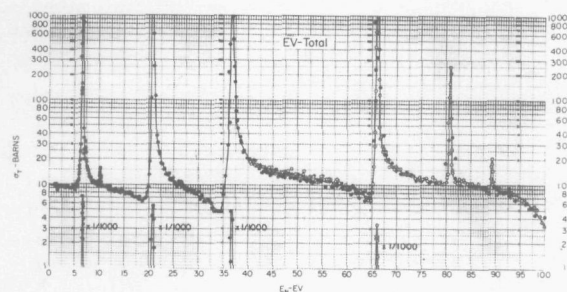
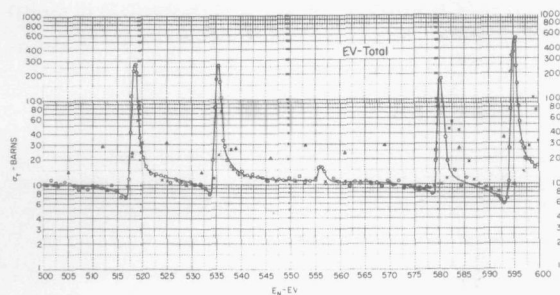


Fig. 1.1.

Total cross-section of  $^{238}\text{U}$  as a function of neutron energy (?)



The combination of our interest in resonance absorption phenomena and the existence of a thermal reactor facility, the HOR (Hoger Onderwijs Reactor) in Delft, lead to the decision to commence investigations on resonance absorption in a neutron spectrum as is characteristic for thermal reactors. The results can be used as a basis for future fast reactor Doppler work.

The "thermal" problem has attracted the attention of theorists as well as experimentalists for quite some time (2,3,4,5,6), but has not yet been solved satisfactorily. Nevertheless our work could be carried out on the basis of already existing theoretical knowledge. For the experiments a new tool was developed - the epithermal local pile oscillator (13). The method in question is considered in

detail, and its results are compared where possible with optimised computer codes in the following parts of this thesis. It is our belief that this method is not restricted to a specific neutron spectrum, and therefore in principle could be used in a fast reactor spectrum too.

### 1.2. Existing experimental methods

The phenomenon of epithermal-neutron absorption in thermal reactors is often compressed in one effective absorption cross-section for the whole resonance energy region, using a  $\frac{1}{E}$  neutron flux distribution as the weighing function. This cross-section is called the resonance integral RI (sect. 2.1.2); it can be determined experimentally by activation or reactivity techniques. Both methods have been described several times (8,9), (10,11), and a detailed discussion thereof will not be given here, although some remarks have to be made.

In both cases the measurements are usually performed on single cylindrical rods of varying diameters. When temperature dependence is considered, the samples are usually heated to a uniform radial temperature distribution. This is sufficient for safety studies when primarily prompt effects have to be considered, which occur before a new equilibrium temperature distribution has been reached. Some exceptions to these rules and a more detailed survey of experimental methods are given by Hellstrand (12). A small central foil of the cylinder is used as the measuring object in *activation experiments*. The activation of the foil has to be compared with that of a standard foil, from which information about the absorption properties of the cylinder material can be distilled. Careful alignment and rods of sufficient length are basic requirements for reliable results. In the determination of resonance integrals the uncertainty in the RI of the standard that has to be used ( $^{197}\text{Au}$ : 2.5%) is often the main source of error (which is also the case for reactivity methods). Extreme caution has to be taken when temperature dependence (Doppler-effect) measurements are carried out as the reproducibility of the measurements must be within 1%. Furthermore we must not forget that activation methods are applicable only to isotopes in which neutron capture leads to radioactive products. In *reactivity experiments* the reactivity effect upon insertion in the reactor of a sample

rod is compared with the effect caused by a standard absorber. Danger coefficient measurements (simple insertion, (10)) and global oscillator techniques (periodic insertion and extraction, (11)) have been used. A most important problem is to keep the reactor power sufficiently constant during these measurements. Apart from a good knowledge of the neutron flux spectrum - which is essential for all resonance absorption experiments - the energy dependence of the importance function must also be known in the case of reactivity methods. This function has a bearing on the fact that neutrons which are absorbed in the sample at different energies do not represent an equal reactivity loss. When the sample and the oven, in the cases where this latter is used, are surrounded by cadmium - to prevent the thermal neutrons from entering - the importance function will be reduced at lower energies (10). Finally it has to be noted that moderation in the equipment or the sample may give rise to extra absorptions in the cadmium surroundings, which effect requires correction.

The *local oscillator technique* for epithermal-neutron absorption measurements as discussed in this thesis offers some distinct advantages with respect to the existing methods. Of these mention may be made of a simple "importance" relation which is reduced to an ionisation chamber efficiency function, and the fact that sample and detector are not separated by a cadmium thermal-neutron barrier.

### 1.3. *Outline of the following chapters*

Chapter 2 deals with the experimental techniques applied in the measurements, and the determination of the effective cadmium boundary. A specific method which was used to determine the epithermal-neutron spectrum is described. In the next Chapter the calibration procedure of the oscillator with gold-lead rods, the nuclear properties of which are well-known, is reported.

In Chapter 4 an outline is given of several computer codes which were used in comparison with the measurements. Calculated results for resonance integrals and Doppler-coefficients of the sample rods are given in Chapter 5 and are compared with literature data.

Chapter 6 contains the principle experimental results of the local oscillator, and a critical comparison with calculated predictions. A number of experimental verifications on possible systematic error sources is reported. The Chapter also deals with an evaluation of the usability of the method based on the results of the work. Some remarks concerning the application in spectra which are normal for intermediate or fast reactors are included.

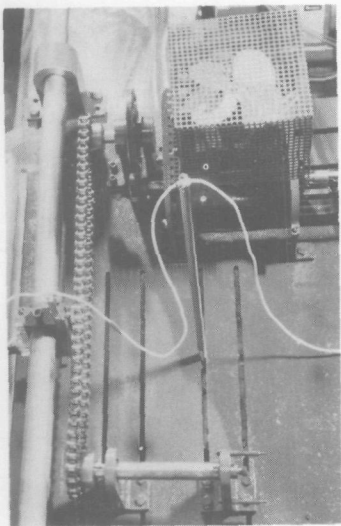


Fig. b.  
Rotating-chain  
mechanism and  
oscillator tube  
(from above)

## CHAPTER 2      EXPERIMENTAL METHODS<sup>1</sup>

### 2.1. *Description of the local pile oscillator*

The local pile oscillator is well-known as a device for determining thermal neutron absorption cross-sections (14,15). The principle on which it is based is that the magnitude of the local flux depression caused by an oscillating sample can be used as a measure for the total sample absorption. Usually by comparison with boronated standard samples, "pile type" neutron cross-sections for thermal reactors can be obtained.

We decided to use the instrument to study epithermal-neutron absorption in a  $\frac{1}{E}$ -spectrum, and therefore constructed a local pile oscillator completely surrounded with a cadmium shield. Practically only neutrons with epithermal

<sup>1</sup>Partially described earlier in (13)

energies can now reach the detector region. The apparatus was placed in the thermal column of the Delft HOR-reactor (Figs. 2.1 and 2.2). The neutron spectrum in the thermal column has a form approximate to  $\frac{1}{E}$ , the verification of which will be reported in section 2.4.

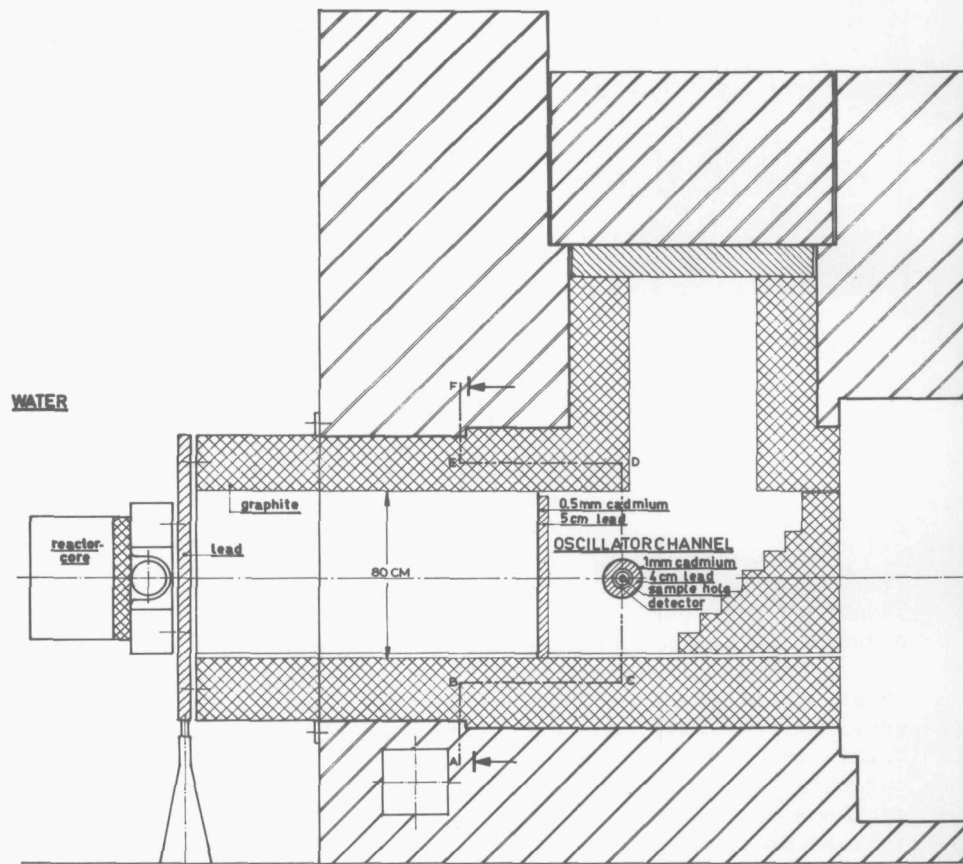


Fig. 2.1.

Vertical cross-section along the axis of the thermal column of the HOR

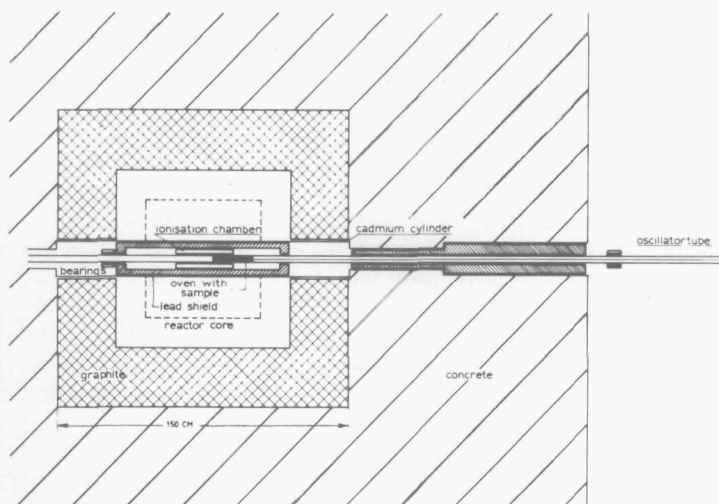


Fig. 2.2. Radial cross-section of the thermal column of the HOR (A-B-C-D-E-F, see Fig. 2.1.)

#### 2.1.1. Neutron detector

In fact it is the change in detector current, when the sample is moved in and out of the ionisation chamber, which is presumed to be representative for the neutron absorption in the sample. It is therefore necessary to have a clear knowledge of the detector output signal as a function of the energy of an incident neutron, so as to make it possible to relate detector response and neutron absorption in the sample correctly. For this purpose the well-defined  $\frac{1}{4}$ -cross-section of the boron lining on the electrodes of the current type ionisation chamber is favourable. Furthermore this boron layer with less than  $0.48 \text{ mg/cm}^2$  does not seriously disturb the flux distribution for epithermal neutrons inside the chamber. This can be easily checked by simple calculation.

An experimental problem which arises in this concept is due to the fact that the detector is also sensitive to gamma rays, via conversion electrons which are released, e.g., from the

electrode material. The disturbing effect in the detector current caused by response to gamma rays, and the distortion of this current by an oscillating sample, may become important (see (18), appendix). The phenomenon is strengthened by the increased gamma intensity following the numerous neutron captures in the cadmium shield. The use of an ionisation chamber with gamma compensation electrode is inadequate in case of a moving absorber, because this compensation will be direction-dependent. The gamma-ray problem is less severe for measurements on thermal neutron cross-sections. This is illustrated by the fact that the total detector current was reduced to about 1% of its initial value by the introduction of the cadmium shield, being a consequence, of course, of the disappearance of the thermal component of the neutron flux<sup>1</sup>.

Two measures were taken to suppress the gamma signals:

1. gamma shielding material was placed between the cadmium layer and the detector, by positioning a 4 cm lead annulus around the ionisation chamber (Fig. 2.2);
2. a detector with a large neutron - to gamma sensitivity-ratio was developed (Fig. 2.3).

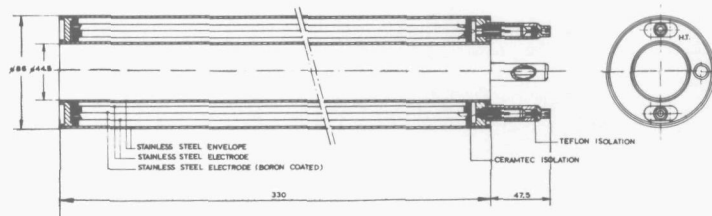


Fig. 2.3. Annular ionisation chamber

<sup>1</sup>The cadmium ratio for a 100 $\mu$  gold strip was determined as  $12.1 \pm 0.2$  before the cadmium shield was placed.

The detector as indicated under 2) is a variation on the annular ionisation chamber used by Small and Spurway (75) for their thermal local oscillator. For the design it was taken into consideration that the electrons, which are released by gamma radiation, normally spread their ionisations over an appreciable volume. Thus the gamma signal is roughly proportional to the sensitive volume of a detector. The products of the  $^{10}_5\text{B}(n,\alpha)^7_3\text{Li}$  reaction have a much shorter range, and the number of ionisations caused by these will quickly decrease from a maximum at a position near the coated electrode. Therefore, in order to improve the usability of the Small and Spurway detector for our purpose, the specifications were changed, resulting in more desirable properties (Table 2.1).

Table 2.1. Ionisation chamber properties

design	electrode coating	electrode spacing	gas filling	sensitivity	
				gamma	neutron
(75)	natural boron 0.5 mg/cm <sup>2</sup>	6 mm	76 cm A	1.5 10 <sup>-10</sup> A/R hr	1.8 10 <sup>-14</sup> A/nv
new	90% enriched in <sup>10</sup> B 0.48 mg/cm <sup>2</sup>	4 mm	25 cm H <sub>2</sub>	0.8 10 <sup>-11</sup> A/R hr	3.6 10 <sup>-14</sup> A/nv

The gamma sensitivity of an ionisation chamber is roughly proportional to the product of detecting volume and filling gas stopping power, the latter being for 25 cm H<sub>2</sub> about 15 times smaller than for 76 cm A. If selfshielding is disregarded, the neutron sensitivity is roughly proportional to the boron enrichment. However, due to the decreased stopping power of the hydrogen, an appreciable portion of the energy of the products of the  $^{10}_5\text{B}(n,\alpha)^7_3\text{Li}$ -reaction is dissipated outside of the sensitive volume of the newly designed chamber, which decreases its neutron sensitivity. A 0.3 MeV alpha-particle for example has a range of about 3 cm in 25 cm H<sub>2</sub>, compared with about 0.2 cm in 76 cm A. Ranges are, of course, smaller for the <sup>7</sup>Li-ion; it must also be mentioned that most particles leave the <sup>3</sup>boron layer only after an appreciable energy decrease. It may be stated as a general rule that the neutron - to gamma sensitivity-ratio of an ionisation chamber of this type will increase with diminishing electrode spacing and gas stopping power, at the expense of a decreasing absolute neutron sensitivity.

An extra advantage of the new design is that the high voltage can be kept as low as 200 V without losing full saturation. This diminishes leak currents.

A suitable sample was oscillated in order to check the absence of gamma-absorption response in the detector and also that of possible neutron-scattering signals. We used lead, which absorbs neutrons weakly ( $\Sigma_a(2200) = 0.006 \text{ cm}^{-1}$ ) and which has neutron-scattering and gamma-absorbing characteristics resembling those of the materials we wish to study, viz. fissionable and fertile isotopes. A relatively weak oscillator response to the oscillation of lead samples means that the disturbing effects play a minor role. In fact, measurements showed them to be reduced to a negligible level ( $\ll 1\%$  for uranium and thorium).

A discussion about the effect of slowing down by lighter materials is given in section 2.2.2.

#### 2.1.2. Definition of measured quantities

The measured results of the local pile oscillator are not directly proportional to the absorption in the samples due to the interfering detector-efficiency function. For a discussion of this phenomenon we consider a situation where disturbing effects of any kind are negligible (like non  $\frac{1}{E}$ -flux, moderation effects). Furthermore the detector current is assumed to be proportional to the boron-reaction rate, independent of the kinetic energy of the reacting neutrons, which commonly is negligible compared to the 2.30 MeV or 2.78 MeV ( $^{16}$ ) that are released in the  $^{10}_5\text{B}(n,\alpha)^7_3\text{Li}$ -reaction. For the coating thicknesses which are considered, the reaction rate is roughly uniform over the whole coating depth for neutrons of different energies.

It can be stated under these conditions that the reduction of the reaction rate in the ion chamber after insertion of the sample can be represented by

$$\Delta R = C \int_{\text{sample vol.}} \int_{E_{\text{Cd}}}^{\infty} \sigma_a(E) \left\{ \frac{\phi}{\phi_{\infty}}(E, \bar{r}) \right\} \frac{1}{E} \frac{1}{\sqrt{E}} dE d\bar{r} \quad (2.1)$$

where  $\phi/\phi_{\infty}(E, \bar{r})$  is the flux depression in the sample  
 $C$  is a proportionality constant

This expression must be compared with the formula for the

resonance integral (17):

$$RI = \frac{1}{V} \int_{\text{sample vol.}} \int_{0.55}^{\infty} \sigma_a(E) \left\{ \frac{\Phi}{\Phi_{\infty}}(E, \bar{r}) \right\} \frac{1}{E} dE d\bar{r} \quad (2.2)$$

This is, in fact, that cross-section which, when multiplied by the flux that would be present in the absence of resonances, gives the true reaction rate. The difference between Eq. (2.1) and Eq. (2.2) lies mainly in the factor  $1/\sqrt{E}$  occurring in Eq. (2.1), which represents the detector efficiency. A quantity which can be directly compared to RI is the "chamber integral" CHI, which reads:

$$CHI = \frac{\Delta R}{CV} = \frac{1}{V} \int_{\text{sample vol.}} \int_{E_{Cd}}^{\infty} \sigma_a(E) \left\{ \frac{\Phi}{\Phi_{\infty}}(E, \bar{r}) \right\} \frac{1}{E^{3/2}} dE d\bar{r} \quad (2.3)$$

Both RI and CHI can be computed from known resonance parameters and/or cross-sections. For the materials and rod dimensions we studied, a linear relationship between the two was found from computations (Fig. 6.1). Therefore measurements with the local oscillator, providing CHI, may in principle be used to determine resonance integrals and Doppler coefficients. Moreover, a more direct comparison with theory becomes possible by computing and measuring CHI as a function of sample geometry and temperature. The investigations which are described here, as an application of the epithermal local pile oscillator, concern this type of work. Measurements and computations are made on uranium, thorium and uranium dioxide rods. Of course, in view of the specific detector sensitivity, the resonances at lower energies (which are generally better known than resonances at higher energies) will play a fairly dominant role.

Although the interfering detector efficiency as such is an unfavourable aspect of the local oscillator method, it may be rementioned (sect. 1.2, see also sect. 5.2.4, marked paragraph) that some compensating advantages exist:

1. the normally troublesome computations of the importance as a function of energy at the absorber position are simplified to the required knowledge of the detector efficiency;
2. the disturbing effect of the absorption in the cadmium shield of neutrons slowed down in the sample is greatly diminished with a detection instrument inside the cadmium shield;

3. the local oscillator will occupy only a modest part of the reactor which is used in this case as a neutron source.

When the interest of the investigator is concentrated on low energy resonance absorption, the specific sensitivity of the local oscillator will, of course, be advantageous.

#### 2.1.3. *Technical data*

##### 2.1.3.1. *Oscillator drive and sample housing*

The samples are placed in a stainless steel or aluminium cylindrical oscillator tube (37 x 40 mm) which has a length of about 6 m so that it extends on both sides of the thermal column. This tube is oscillated by a rotating chain with a frequency of about 0.25 Hz and an amplitude which may be varied from 30 cm to 100 cm; normally the amplitude is 60 cm. When measurements at *room temperature* are made, it is usual to oscillate *two samples* at the same time, one acting as a standard. In this case the result, being the quotient of the output for the two samples, becomes independent of reactor power, oscillator frequency, etc. The samples are then housed in simple aluminium cans, which are interconnected and attached to the end of the oscillator tube by thin aluminium rods with bayonet catches so that they can be quickly maintained in case of activation. If it is necessary *to heat* the sample it is placed in a *furnace* (sect. 2.1.4). In this case the oscillator output, originating from only one sample, is normalised by dividing it through the integration result for a small part of the current of the main ionisation chamber during the oscillation time. The integrated voltage is even for the strongest absorbers only slightly (< 0.5%) diminished by the absorber-induced dips in the chamber current and therefore gives a proper indication of the reactor power.

The oscillator drive is schematicly represented in Fig. 2.4.

Position feed back (electronic timer) has been used to maintain a constant oscillation period. Furthermore, velocity feed back is also applied (servo generator) in order to smoothen the chain movements over the complete cycle.

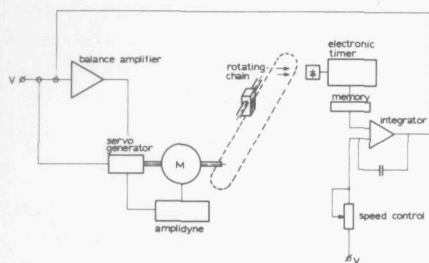


Fig. 2.4. Oscillator drive

### 2.1.3.2. Signal flow

The modulated current originates from the negative voltage, "main", ionisation chamber (Fig. 2.5). The DC-component, generated by the gross reactor flux, is compensated by the current of an other "monitor" ionisation chamber with positive high voltage, situated at some distance from the oscillator. After passage of the current(s) through the manually adjusted compensator, the absorber induced

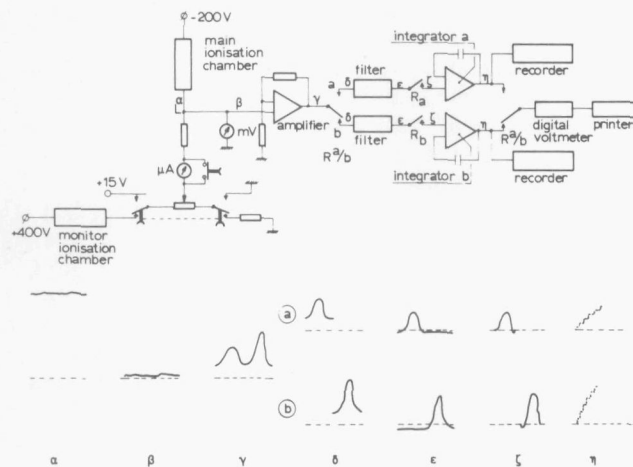


Fig. 2.5. Signal flow and pulse shapes

fluctuations survive whilst overall power fluctuations have lost much of their influence (pulse shape  $\beta$ ). The pulses resulting from the subtraction process, originally only about 0.1% of the detector current, are then fed into a DC-amplifier.

When room temperature measurements are carried out, the current is fed into one of the two channels according to the position of the relay  $R^{a/b}$ , after which it passes through a bandpass filter tuned to the oscillation frequency; the pulses are then integrated during the time that the relays  $R_a$  or  $R_b$  are closed. These adjustable integration intervals render scattering-compensation possible in certain cases, e.g. if a flux gradient exists along the axis of the oscillator channel (see (15)), however, it was not necessary to use this method for our measurements.

The output voltages of the integrators, representing the oscillator results for the two absorbers, are read out and printed after an adjustable number of oscillations has been carried out. When oven measurements are carried out it is not advisable to oscillate two samples simultaneously. This is because the oven is attached by a 3 m long tube (the evacuation tube) to one side of the oscillator tube. To prevent thermal expansion of this evacuation tube - which would move the sample out of position - the direction of flow of cooling air must be from the side of the evacuation tube in the direction of the oven. Since the reference sample can be placed only on the other side, it is not easy to prevent some unintentional heating of this sample. Therefore preference was given to a solution with oscillation of the oven sample only. Therefore  $R^{a/b}$  (Fig. 2.5) is always connected to channel a, and  $R_a$  is replaced by a gate element which allows only one polarity of the signal to pass (Fig. 2.6). This replacement proved to be useful in minimising the influence on the oscillator output of remaining small sample displacements due to thermal expansions at high temperatures. The effect is illustrated in Fig. 2.7, which shows the oscillator output as a function of the distance between the midpoint of the oscillation trajectory and the midpoint of the detector. As already was mentioned (sect. 2.1.3.1), a small part of the main chamber current is directly integrated in integrator b so that the reactor power is monitored. This is necessary, of course, in order to normalise the result when a standard sample is lacking.

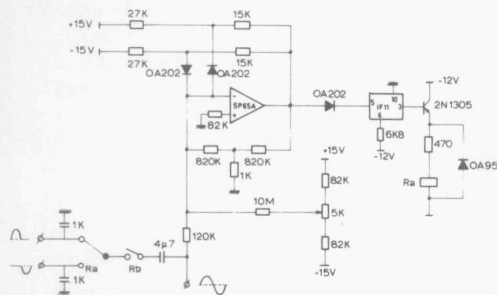
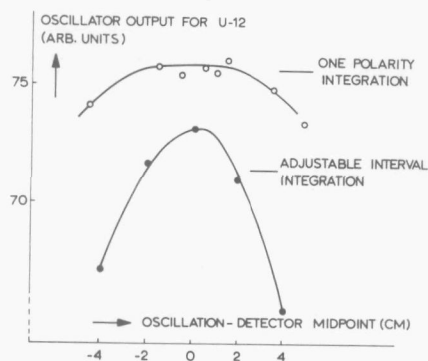


Fig. 2.6. One-polarity gate

Fig. 2.7. Effect of sample displacement



### 2.1.3.3. Switching logic

The principles of the switching logic can be seen from Figs. 2.5 and 2.8.

The room-temperature measurements (two-channel) procedure is as follows. The relay R11 (contacts U, V, W and X) is energised when the synchronous motor M, acting as a clock, produces a pulse. When the contacts U and V have been opened the relays R<sub>a</sub> and R<sub>b</sub> (telegraph type relays with a mid-position) are able to close when a pulse is received from the phototransistors F1 or F3. These transistors, just as F2 and F4 do, which determine the position of the R<sup>a/b</sup> relay in the oscillation path, get signals from a light attached to the moving oscillator tube, and their positions can be adjusted. The pulses from F1 and F3 are lengthened to blocks, variable from 300 ms to 700 ms in the integration time one-shot. The relay R<sub>a</sub> is opened by F1 when R<sup>a/b</sup> is in upper position, and relay R<sub>b</sub> by F3 when R<sup>a/b</sup> is in the down position.

At the time that R11 was energised, it actuated (contacts W and X) the operation of the three decades register simultaneously, so every integration is counted until a preset number is reached, after which relay R10 is closed. This causes R11 to fall off again, the  $R_a$  and  $R_b$  relays can not be closed anymore, and the register is reset to zero, as a result of which R10 opens again. The integrator voltages are now printed out. The process repeats itself when the clock supplies a new starting pulse.

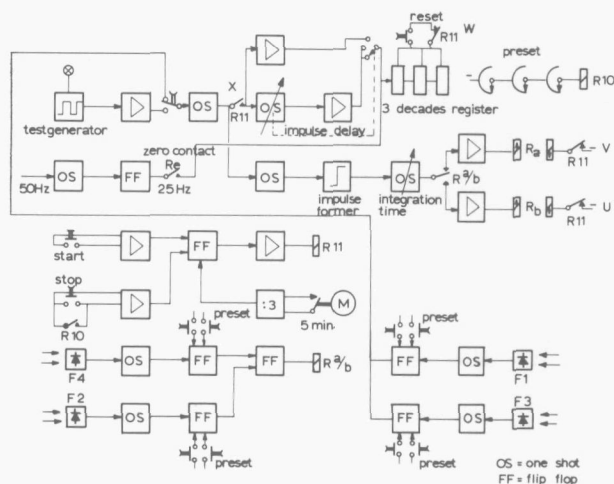


Fig. 2.8. Switching circuit of the oscillator (R stands for relay, M for motor and F for phototransistor; for  $R_a$ ,  $R_b$  and  $R^a/b$  see also Fig. 2.5.)

The measurement is automatically repeated until the investigator decides to insert one or two new samples.

When oven measurements are carried out, the changes indicated in the measuring circuit (see foregoing section) make the program run in a more simple way. Temperature changes can be made while the measurements are being carried out continuously.

#### 2.1.3.4. Oven construction and temperature regulation

To heat the cylindrical sample rods which are 90 mm long

and which have diameters between 6 and 20 mm, an oven has been constructed (Fig. 2.9). The oven is made mainly from the low neutron-absorbing material zircaloy-30 (0.46 - 0.66% Cu, 0.50 - 0.60% Mo, remainder Zr).

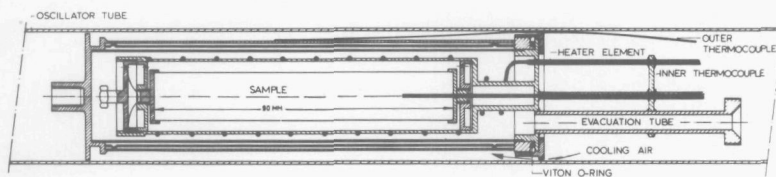


Fig. 2.9. Fuel furnace

The thin radiation shields of 0.2 mm, however, are from stainless steel. The rod in question is placed in a zircaloy or stainless-steel canning in the middle of the furnace. The sample is heated with an isolated bipolar miniature heater element (with a maximum dissipation of about 300 W) to maximum 800°C. The temperature is recorded by a Cr-Al thermocouple which is inserted in a 15 mm deep and 1.2 mm wide hole in the sample. The external temperature of the oven is recorded by an identical thermocouple. The calibration data of the thermocouples were controlled in freezing zinc (419.5°C) as well as lead (327.5°C). The two temperatures of phase transition of uranium metal (668°C and 774°C, (19)), which could be easily recognized in a test heating (recrystallisation heat), provided other check points.

Table 2.2. Some properties of possible oven materials

	$\Sigma_a$ (2200) ( $\text{cm}^{-1}$ )	$\Sigma_s$ (2200) ( $\text{cm}^{-1}$ )	melting point (°C)
zircaloy-30	0.0115	0.0074	1850
Fe	0.222	0.0329	1535
Ni	0.420	0.0536	1453
Al	0.015	0.0061	660

To prevent possible appreciable oxidation of the samples or the oven, the furnace is continuously evacuated except during the cooling period when helium gas is allowed to enter up to a pressure of about 2 atmospheres. The external cooling of the oven is brought about by sucking a stream of air at room temperature through the space between oven wall and inner side of the oscillator tube.

The temperature of the oven is maintained at a prescribed value by a simple steering unit (Eurotherm, model PID/SCR 10 FET/EH). The heating of the oven is automatically stopped if one of the following conditions is fulfilled:

1. gas pressure in the oven  $> 5 \cdot 10^{-1}$  Torr;
2. oven inside or outside temperature exceed manually adjusted boundary conditions;
3. one of the thermocouples breaks down;
4. heating element current exceeds preset maximum.

The uniformity of the heating was controlled along the axis of the cylinders, as heat leakage will take place mainly in this direction due to the construction of the oven. An axial hole of 1.5 mm wide was drilled through two monel rods, 8 mm and 18 mm in diameter respectively and both 90 mm long. The properties of this material compared to uranium metal are: specific heat 0.127 cal/g°C - 0.028, heat conductivity 0.045 cal/s cm°C - 0.063 (79).

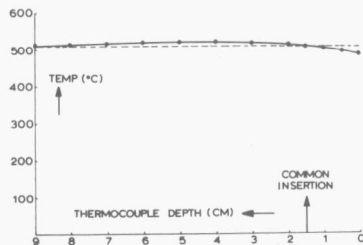


Fig. 2.10. Axial temperature plot for monel-18

----- average temperature  $\bar{T}$

Fig. 2.10 shows the temperature plot for the second monel rod (diam. 18 mm), which gives, as might have been expected, the more pronounced curvature. The effect of heat leakage is visible near the place where the sample holder is connected to the roof of the oven. The approximate average sample temperature  $\bar{T}$  exists at the place where the temperature is

normally detected (about 15 mm inside the sample, vertical arrow Fig. 2.10). In fact instead of  $\sqrt{T}$  we should know the value of  $\sqrt{\bar{T}}$  (sect. 5.2.4). However, apart from the question whether the thermocouple indicates under all conditions exactly  $\bar{T}$ , the difference between the two values is small in view of the error margins involved in the Doppler measurements (sect. 5.3.2).

## 2.2. Corrections to be applied to the measurements

### 2.2.1. Empty oven correction

Although the oven is constructed mainly from zircaloy-30, which has a  $\Sigma_a(2200)$  of no more than about  $0.012 \text{ cm}^{-1}$ , it weighs circa 300 g, resulting in a considerable neutron absorption. This will be of appreciable influence, especially in measurements on small absorber rods. We tried to minimise this effect by lengthening the oven on both sides with stainless steel bars which had about the same absorption per unit length as the furnace. The result of this method could be judged by visualising the signal form with the use of a 400-channel analyser in the "multiscaler" mode, which is illustrated in Fig. 2.11.

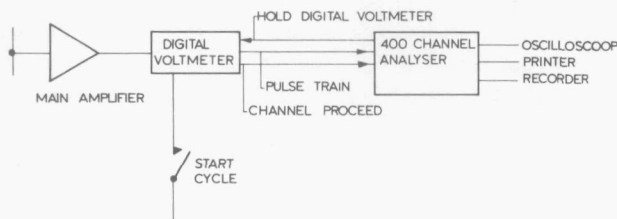
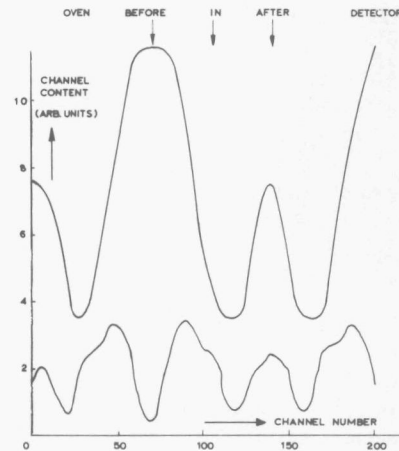


Fig. 2.11. Block-diagram of multiscaler assembly

The voltage on the output of the main amplifier of the oscillator is monitored continuously by a digital voltmeter, after a cycle start relay has been closed. The voltmeter, which is of the integrating type, determines the voltage 33 times per second with an integration time of 20 ms. The result of each measurement is in the form of a pulse train fed into a channel of the analyser memory. After one measurement has been finished, the next channel is opened. When all the available memory channels have been opened, the measurements are stopped until a new cycle start pulse is received. The process is repeated during a predetermined number of cycles. In the analyser a reproduction of the signal form is built up, which is less and less disturbed by statistics.

Fig. 2.12.  
Multiscaler response for empty oven without (upper line) and with (lower line) lengthening steel bars



In Fig. 2.12 the effect on the signal of the introduction of absorbing steel bars can be seen. The upper line shows the analyser result, when no bars are used. The absorption is minimal (current maximal) when the oven plus supply wires, etc. are completely withdrawn from the hollow cylindrical detector. The situation as sketched in the lower line is obtained with the absorber bars present. In this way the empty oven result is diminished to 20% of that of Th10, the sample with the lowest absorption (this is 1.6% of the U20 absorption).

### 2.2.2. Slowing down correction

Because neutrons which scatter in the sample loose part of their energy, it may be expected that the presence of the sample will create a number of neutrons having energies below the cadmium threshold. This will give rise to an extra detector response, compensating for possible absorption effects. As will be illustrated, the effect is negligible for pure heavy absorbers such as  $^{238}\text{U}$  and  $^{232}\text{Th}$ , but becomes important when a ceramic material, e.g.,  $\text{UO}_2$  is oscillated. To judge the magnitude of the effect a number of special rods was oscillated; the results normalised on the reactor power (O/P) are given in Table 2.3. All rods had a length of 90 mm and a diameter of 20 mm.

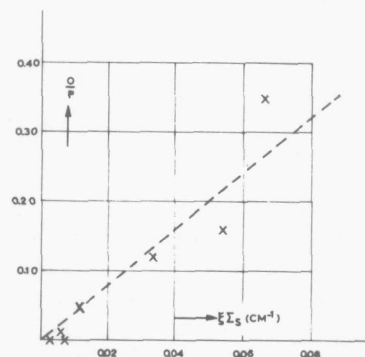
Table 2.3. Determination of the slowing down correction

material	$\xi \Sigma_s (2200)$ ( $\text{cm}^{-1}$ )	$\Sigma_a (2200)$ ( $\text{cm}^{-1}$ )	calculated absorption effect(O/P)	oscillator result (O/P)		
				measure- ment	apparent moderator effect	temp. effect 30-600°C
C	0.066	0.000	-	- 0.35	- 0.35	- 2%
Mg	0.012	0.003	+ 0.01	- 0.04	- 0.05	- 3% <sup>1</sup>
Al	0.006	0.015	+ 0.02	-	- 0.02	-
Pb	0.003	0.006	-	-	-	-
Zr	0.007	0.008	+ 0.01	-	- 0.01	-
Fe	0.033	0.222	+ 0.31	+ 0.19	- 0.12	+ 4%
Ni	0.054	0.420	+ 0.59	+ 0.43	- 0.16	+ 2%
Ti	0.009	0.328	+ 0.47	+ 0.47	-	< 1%

<sup>1</sup>30-400°C

From Fig. 2.13 it can be seen that there is a roughly linear relation between the slowing down power of the sample and the oscillator response.

Fig. 2.13.  
Oscillator response corrected for neutron absorption and normalised on the reactor power, as a function of the slowing down power of moderating samples



An interesting effect is the temperature dependence in the moderation response. It originates in the thermal motion of the atoms, which influences the mean lethargy gain per collision  $\xi$  in the neighbourhood of the cadmium boundary

according to (68):

$$\xi \approx \frac{2}{(A+\frac{2}{3})} \frac{(E-2kT)}{E} \quad (A>10). \quad (2.4)$$

When the temperature rises  $\xi$  diminishes, which causes a smaller "moderation signal". This effect is responsible for the apparent "Doppler effect" in the approximate  $\frac{1}{v}$ -absorbers in Table 2.3. The relative magnitude of the temperature effect grows, of course, when absorption and moderation signals are more in equilibrium.

A check on the proper functioning of the oscillator is the result for titanium. This  $\frac{1}{v}$ -absorber with a small slowing down power may be expected to exhibit no temperature effect, which was shown to be true in the measurements.

The oscillator results for uraniumdioxide rods are corrected for the moderation component in the signal. This is done by comparing their slowing down power  $\xi\Sigma_s$  with that of the graphite sample, and adding a pro-rata compensation to the oxide data. This procedure, based on the graphite result, is selected for the following reasons:

1.  $^{12}\text{C}$  has reactor-physical properties similar to those of  $^{16}_8\text{O}$ ;
2. the measurement of the graphite moderation effect is the most accurate one for the scatterers considered;
3. from Fig. 2.13 follows an approximately linear relation between the slowing down power and  $O/P$ ;<sup>1</sup>
4. the correction leads to good agreement between the oxide and the metal results (Chapter 6).

The slowing down correction ranges from 15% to 20% for  $\text{UO}_2$ -rods with diameters from 10 mm to 20 mm. For uranium and thorium metal the slowing down powers are both about  $0.003 \text{ cm}^{-1}$ , which means that corrections are not necessary.

### 2.3. Determination of the effective cadmium boundary

One of the oscillator parameters is the effective cadmium cut-off energy. The assumption is made that above this energy the neutron flux spectrum is unaffected by the presence of

<sup>1</sup>It is interesting to compare this with the different conclusion of Moore et al. (11), and the similar result of Tattersall et al. (69).

the cadmium shield, whilst below the boundary the flux is supposed to be zero. Of course this rather crude assumption will yield only equal effective boundaries for materials which have about the same dependence between cross-section and energy in the cut-off region, e.g.  $\frac{1}{V}$ -absorbers. This category includes approximately the important isotopes  $^{197}\text{Au}$ ,  $^{238}\text{U}$  and  $^{232}\text{Th}$ . The rather complex geometry of the assembly makes it difficult to compute the effective boundary energy. Therefore we applied an experimental method, using gold-poisoned and boron-poisoned lead samples. The quotient of the measured chamber integrals of these will be strongly dependent on the cadmium cut-off energy, and can be used to determine it from Table 2.4 where some computed results for the cylindrical samples (length 90 mm, diam. 10 mm) are listed. The gold-lead sample contained 2.04 g  $^{197}\text{Au}$  in a  $7.07 \text{ cm}^3$  volume ( $0.288 \text{ g/cm}^3$ ).

Table 2.4. CHI as a function of  $E_{\text{Cd}}$

$E_{\text{Cd}}$ (eV)	CHI (barn/eV $^{\frac{1}{2}}$ )		$\text{CHI}_{\text{Pb-Au}}/\text{CHI}_{\text{Pb-B}}$
	Pb-B	Pb-Au	
0.3	400	201	0.50
0.4	300	187	0.62
0.5	240	178	0.74
0.6	200	172	0.86
0.7	172	167	0.97
0.8	150	164	1.09
0.9	133	161	1.21

The boron amount in the boron-lead cylinder was 83 mg, in the form of fine natural boronoxide powder. This mixture could be considered to be "infinitely diluted", so for boron the unshielded resonance integral  $\text{RI}_{\infty}$  could be used.

For the computation of the chamber integral of the Pb-Au rod the computer code ERIDEL (sect. 4.1.1) was used above 37 eV. For lower energies the computations were carried

out with RIFF RAFF' (sect. 4.2). The homogeneity of the mixture was checked as described in sect. 3.2.2. The result of the measurements was:  $E_{Cd} = 0.80 \pm 0.05$  eV.

#### 2.4. Determination of the epithermal spectrum along the axis of the oscillator channel

##### 2.4.1. Strip activation

The epithermal-neutron spectrum in the oscillator channel was determined by means of resonance foil activation. The spectrum was determined more accurately at one specific position - halfway in the ionisation chamber - but before this it was checked whether strong spectrum shifts were present in the channel. This was done by activating 150 cm long strips of Au, W, Mn and Cu, bare as well as under cadmium, providing thermal and epithermal flux plots over the whole length of the oscillator channel. The bandscanner which was developed for this work is shown schematically in Fig. 2.14. The decay of the activated strip during the

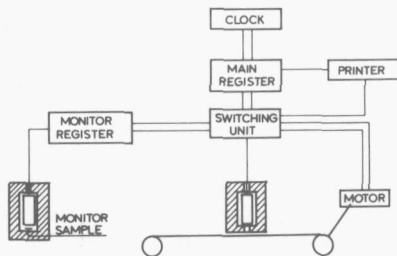


Fig. 2.14.

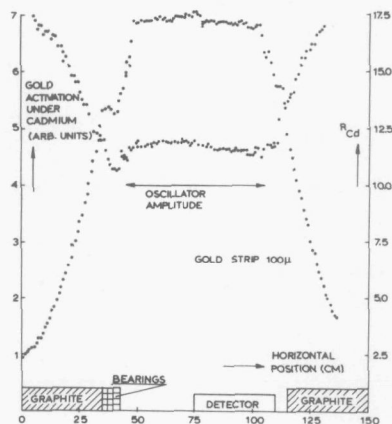
Automatic bandscanner with compensation for decay during measurement

measurements is compensated for by measuring with a monitor counter the (decaying) activity of a sample of the same strip material. The measuring time for each band position is determined by the time the monitor needs to fill its register up to a predetermined value: the more the activity decreases, the longer the measuring time (70).

From Fig. 2.15 it can be seen that in the case of gold the flux as well as the cadmium ratio are approximately flat between the graphite linings. This result was also found for the W, Mn and Cu strips. A necessary condition for the absence

Fig. 2.15.

Epithermal activation (convex) and cadmium ratio (concave) for a 100  $\mu\text{m}$  thick gold strip



of spectral shift is that the form of the curves be more or less identical. This condition is fulfilled. As to Fig. 2.15 it must be remarked that for the real oscillator measurements the bearings as well as the detector have been shifted to the left (see Fig. 2.2).

Another measurement was carried out with strip activation in order to control the absence of thermal neutrons inside the cadmium shielding. A wolfram strip (50  $\mu\text{m}$  thick) was activated in the normal oscillator tube (cadmium cylinder present), and some days later under identical conditions but in a special cadmium lined oscillator tube. In the latter case the activation was a few percent lower over the entire oscillator channel. This could be attributed to a small cadmium cut-off increase due to the increased thickness of the cadmium cover with another 0.5 mm.

#### 2.4.2. Single foils<sup>1</sup>

The cadmium-difference method has again been used to study the epithermal-neutron spectrum in the middle of the oscillator channel. Seven resonance detector foils (see Table 2.5) were used, permitting the epi-cadmium spectrum to be divided into eight groups, seven of which are centered around the

<sup>1</sup>Earlier described in (20)

main resonance of each foil, the eighth being an additional high energy group. Two specific features were introduced in order to improve the usability of the method, viz.:

1. the use of ultra thin foils (thickness less than 0.1% of the mean free path at the top cross-section);
2. computation of the absorption for each foil in each energy group.

The ultra-thin foils were manufactured by vacuum evaporation on a "zapon" film.

Table 2.5. Computed partial resonance integrals

Materials	Energy groups							
	1	2	3	4	5	6	7	8
Partial resonance integrals (barns)								
<sup>115</sup> In	2976	59.8	52.5	6.0	0.26	0.116	0.052	0.041
<sup>197</sup> Au	40.2	1437	11.7	35.7	7.6	11.8	9.2	1.08
<sup>186</sup> W	6.15	2.6	400	0.9	2	1.7	0.5	0.03
<sup>139</sup> La	1.43	0.54	0.53	7.0	0.1	0.07	0.05	0.08
<sup>59</sup> Co	6.62	2.5	2.4	0.96	31.5	0.76	0.11	0.29
<sup>55</sup> Mn	2.30	0.86	0.84	0.24	0.22	6.2	0.3	1.10
<sup>63</sup> Cu	0.78	0.3	0.29	0.08	0.05	0.03	2.05	0.39

Energy groups

1 : 0.8 - 3.06 eV	5 : 82.5 - 183.6 eV
2 : 3.06 - 7.5 eV	6 : 183.6 - 408.6 eV
3 : 7.5 - 37.1 eV	7 : 408.6 - 909.5 eV
4 : 37.1 - 82.5 eV	8 : 909.5 - 32000 eV

For each foil can be stated

$$\sum_{i=1}^7 a_i \frac{\Phi(i)}{\Phi_{th}} = b \quad (2.5)$$

where  $a_i = \Delta R I_{E_{i-1}-E_i}$  = effective resonance integral in energy group  $E_{i-1}-E_i$ ,

$$b = \frac{\sqrt{\pi}}{2} \frac{\sigma_{\text{act}}(2200)g(T) \sqrt{\frac{293}{T}}}{R_{\text{Cd}} - F_{\text{Cd}}} - a_8 \frac{\phi^{(8)}}{\phi_{\text{th}}} \quad (2.6)$$

$\phi^{(i)}$  = epithermal-neutron flux per lethargy unit in group  $i$ ,  
 $\phi_{\text{th}}$  = thermal-neutron flux,  
 $\sigma_{\text{act}}(2200)$  = activation cross-section for 2200 m/s neutrons,  
 $g(T)$  = Westcott parameter,  
 $R_{\text{Cd}}$  = cadmium ratio,  
 $F_{\text{Cd}}$  = cadmium correction factor.

Since the contribution to the total resonance integral from the high energy group will be small for all foils, a rough estimation can be made of  $\phi^{(8)}/\phi_{\text{th}}$ , and after the measurements have been carried out the seven unknowns  $\phi^{(i)}/\phi_{\text{th}}$  can be computed from Eq. (2.5) and cross-section data. The use of thin detectors obviates the need for self-screening calculations, therefore "infinite dilution" partial resonance integrals suffice; they can be computed directly from the existing data. The detector materials  $^{115}\text{In}$ ,  $^{197}\text{Au}$ ,  $^{186}\text{W}$ ,  $^{55}\text{Mn}$  and  $^{63}\text{Cu}$  could be used in this form of thin foils. This was not possible for  $^{59}\text{Co}$  and  $^{139}\text{La}$  because the activation in the thermal column would have been too low. Therefore cobalt was used in the form of a 50  $\mu\text{m}$  thick foil, and lanthanum as a 500  $\mu\text{m}$  thick pellet, containing  $\text{LaO}_2$  (10 wt%) mixed with an organic material. Effective resonance integrals in the eight energy groups were computed for all detectors with the code ERIDEL (sect. 4.1.1). The results obtained are presented in Table 2.5, and are based mainly on BNL-data (?).

The results of the measurements can be seen in Fig. 2.16, where the results for the various groups are plotted at the main resonance energy of the foils. The best straight line fit yields:

$$\phi \div 1/E^{0.99 \pm 0.04} .$$

However, it should be noted that a slight upward curvature seems to be present. The reason for this may well be neutron leakage and absorption during the moderation process.

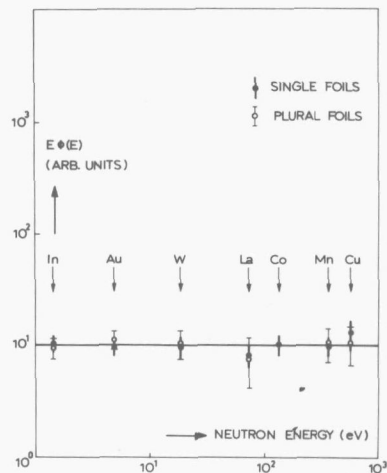


Fig. 2.16. Neutron spectrum in the middle of the oscillator channel

The main sources of error, in order of decreasing importance, are:

1. resonance parameter uncertainties;
2. inaccuracy in the effective cadmium cut-off determination;
3. statistical errors in activation counting.

These three together amount to uncertainties of 10% to 20% in the epithermal fluxes in the various energy groups.

The conclusion that can be drawn from these measurements is that, in spite of the rather complex structure of the thermal column as regards geometry and materials, a clear deviation of a  $\frac{1}{E}$ -spectrum cannot be found.

#### 2.4.3. *The plural foil*<sup>1</sup>

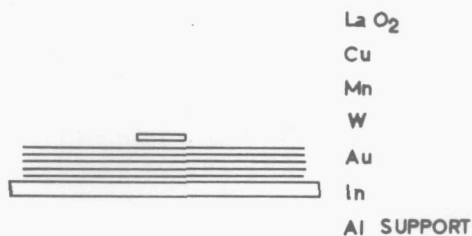
In order to further develop the spectrum method described in the preceding section, an experiment was conducted with a "plural" foil i.e. a combination of detector materials,

<sup>1</sup>Earlier described in (21)

evaporated one on top of the other, on one support (Fig. 2.17). The advantage of this technique is that only two irradiations (or even one with a calibrated foil) would be required to carry out a measurement.

Fig. 2.17.

Plural foil construction



The evaporated foils are not subject to any appreciable mutual interference effect, due to their limited thicknesses. This applies also to the isotope  $^{139}\text{La}$  - which is again used as a small-radius  $\text{LaO}_2$  pellet - due to its single, narrow and pronounced resonance peak.  $^{59}\text{Co}$  was not used in this case because of the long half life of its activation product  $^{60}\text{Co}$  (5.27y). The non-activating "zapon" film which was used for the single foil measurements as foil-bearing material had to be rejected as being too vulnerable and was replaced by aluminium.

The results are consistent with those of the single foil measurements (Fig. 2.16) although for several isotopes the error margins in the plural foils are greater. This is due to the fact that the complicated character of the gamma spectrum which is produced by a plural foil after irradiation (Fig. 2.18) makes the activation

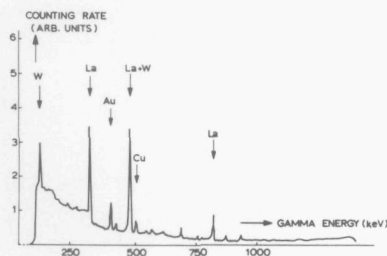


Fig. 2.18.

Gamma spectrum of a plural foil, 24 h after irradiation under a cadmium cover

analysis (semi-conductor spectrometry was used) less accurate than for individual foils. Furthermore the threshold reaction  ${}_{13}^{27}\text{Al}(n,\alpha){}_{11}^{24}\text{Na}$  of the foil-bearing material plays a role in this respect. The isotope  ${}_{11}^{24}\text{Na}$  decays with a  $T_{1/2}$  of 15.4 h to  ${}_{11}^{24}\text{Mg}$ , emitting an electron and several gamma rays (1.27 MeV, 2.75 MeV), which in turn lead to pair production and annihilation radiation. Because the  ${}_{29}^{64}\text{Cu}$  activity ( $T_{1/2} = 12.8$  h) is measured by means of the annihilation radiation, this activation of the support material is undesirable. In our present opinion magnesium or quartz would be better. There is good evidence that the error margins can be reduced by:

1. using a better foil-bearing material;
2. better optimising nuclide quantities;
3. computer analysis of the gamma spectra.

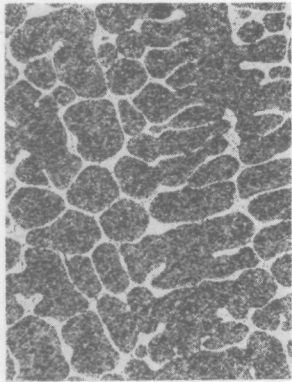


Fig. c.

Microscopic view of sample rod  
Pb-Au-10-2.6, showing Pb-grains  
(dark) separated by  $\text{AuPb}_2$   
precipitates (magnification 100x)

### CHAPTER 3 CALIBRATION OF THE EPITHERMAL LOCAL PILE OSCILLATOR<sup>1</sup>

#### 3.1. *Introduction*

For the interpretation of the measurements on epithermal-neutron absorption, the relationship between the oscillator results and the product N.CHI has to be determined. As an alternative it is also possible - due to the fact that calculations showed that there is a linear dependence between resonance integral and chamber integral for the samples considered (sect. 6.1) - to investigate the linearity (and ratio) between oscillator results and N.RI.

This is done with certain standard samples and is carried out in two steps:

- a. the determination of the RI of the standard samples by activation;
- b. the determination of the oscillator result for each such sample.

<sup>1</sup>This chapter was also previously published (18)

### 3.2. *Standard samples used for testing*

#### 3.2.1. *Type of the standards*

For the standard sample material which has to be an appreciable neutron absorber, the nuclide  $^{197}\text{Au}$  was selected. This isotope is not useful only because of its large resonance integral, but it has also a suitable decay-scheme. Gold has about 50 resonance peaks for neutron absorption below 1000 eV, starting from 4.9 eV. The decay of  $^{198}\text{Au}$  leads to a gamma ray with an energy of 411 keV and an intensity of more than 99% which is used in activation measurements. The half-life of  $^{198}\text{Au}$  is 2.7 days. Therefore short living activations which might still be present in the sample can be given the opportunity of decaying.

#### 3.2.2. *Shape of the standard samples*

The standard samples were made in the form of cylinders consisting of a gold-lead alloy. Rods with 90 mm length and varying diameters and gold content were used. They are encoded in Table 3.1 as Au-Pb-rod diameter (mm)-approximate weight percentage of the gold.

Lead was chosen as the diluent because it has:

- a. small neutron absorption;
- b. nearly isotropic neutron-scattering properties in the laboratory system;
- c. small slowing-down power;
- d. good alloying properties with gold.

The homogeneity of the alloy was checked by means of a microscopic analysis and by neutron-activation analysis. There was a standard deviation of about 1% in the number density of gold atoms per gram alloy, which had a negligible effect on the resonance integrals.

### 3.3. *Determination of the resonance integral of the standard samples*

#### 3.3.1. *Description of the activation method*

The resonance integrals of the gold samples were determined by means of activation analysis. For this purpose the sample

Table 3.1. Gold-lead sample data

no.	designation	atom density ( $10^{24}$ at/cm <sup>3</sup> )		diam. (mm)	RI(b)	
		Au	Pb		computed	measured (±4%)
1	Au-Pb- 6-3	0.001030	0.0321	6	431	431
2	Au-Pb-10-3	0.001030	0.0321	10	348	323
3	Au-Pb-14-3	0.001030	0.0321	14	303	288
4	Au-Pb-18-3	0.001030	0.0321	18	277	273
5	Au-Pb-24-3	0.001030	0.0321	24	245	229
6	Au-Pb-10-0.5	0.000171	0.0328	10	747	727
7	Au-Pb-10-1.0	0.000342	0.0327	10	559	558
8	Au-Pb-10-1.5	0.000513	0.0325	10	468	469
9	Au-Pb-10-2.0	0.000684	0.0324	10	414	432
10	Au-Pb-10-2.6	0.000884	0.0323	10	372	370
11	Au-Pb-10-5.0	0.001680	0.0319	10	279	282

was exposed simultaneously with a gold foil to the neutron flux in the oscillator tube, which foil, being very thin, could be considered to be "infinitely diluted". The activations of the two were compared. The foils were composed of a 15  $\mu\text{m}$  thick aluminium disk with a diameter of 28 mm, on top of which a thin gold coating of about 30  $\text{\AA}$  with a diameter of 12 mm. For the determination of each resonance integral three foils were irradiated simultaneously. The foils were placed in a lead rod in order to equalize the irradiation circumstances with those of the sample.

The foil thickness has to be compared with a mean free path of about  $5 \times 10^4 \text{\AA}$  at the energy of the top cross-section of the 4.9 eV gold resonance. When the number of the gold atoms in the foil is known the neutron flux can be determined from the activation. With this value and the activation of the unknown sample the resonance integral can be found from

$$RI_s = \{(\epsilon_s A_s N_\infty V_\infty) / (\epsilon_\infty A_\infty N_s V_s)\} RI_\infty, \quad (3.1)$$

where  $\epsilon$  represents detection efficiency and  $A$  indicates activity. The subscripts  $s$  and  $\infty$  refer to the sample and the foil respectively. A value of  $1563 \pm 4$  b was selected as being the "infinite dilution" resonance integral for gold.

### 3.3.2. *Chemical separation*

The methods to determine  $A_{\infty}$  and the product  $N_{\infty}V_{\infty}$  are rather well-known. Special attention, however, had to be paid to the determination of  $A_s$ .

First the activated gold in the sample was mixed by melting and properly stirring the alloy. Thereafter separation of gold and lead was required in order to prevent absorption in lead of gamma rays emitted by the activated gold. For that purpose the gold-lead alloy was dissolved in a mixture of nitric and hydrochloric acid. Part of the lead was precipitated by means of sulphuric acid. Then the gold was separated from the nitric hydrochloric solution by repeated extraction with ethyl acetate. In this organic solution the activity of the gold was determined. Thereafter the result was corrected for the difference in the geometry between foil and sample counting, which correction is expressed by the factor  $\epsilon_s/\epsilon_{\infty}$  in Eq. (3.1).

### 3.3.3. *Measurement of the activity*

The activities of the foils and samples were measured by means of a gamma scintillation counter connected to a 400 channel analyser. The number of counts under the photo-peak in the interval from 290 keV till 480 keV was presumed to be a measure of the activity. The number of counts under this peak was always greater than  $2 \times 10^4$ .

### 3.4. *Oscillator test*

The oscillator linearity could be investigated after the resonance integrals of the samples had been determined. In order to eliminate the influence of a possible variation in the neutron intensity caused by a change of power of the reactor each sample was oscillated together with the same standard sample. The number of oscillations for each result was about 1000, requiring a measuring time of half an hour. During the oscillation the two samples were interchanged at half-time:

- a. because the two integrator channels will have slightly different electrical properties;
- b. so as to equalize the geometrical circumstances for both samples.

Now the normalized oscillator result is given by

$$X/S = \{(X_A X_B)/(S_A S_B)\}^{1/2}, \quad (3.2)$$

where  $X_A$  and  $X_B$  are the integrator readings for the investigated sample in the two different oscillator channels and  $S_A$  and  $S_B$  the oscillator results for the standard sample.

When a gold-lead sample is oscillated, corrections have to be introduced for:

- a. the signal due to the gamma ray absorption in the lead,  $X_{pb}$ ;
- b. the signal due to the presence of the sample holder,  $X_o$ ;
- c. the cross-talk from the sample in one channel to another,  $X_i$ .

Then the corrected signal becomes

$$X = X_{ms} - X_{pb} - X_o - X_i, \quad (3.3)$$

where  $X_{ms}$  is the measured integrator result.

### 3.5. Results

#### 3.5.1. Resonance integrals

Firstly the results of activation measurements on the resonance integrals of the standard samples are compared with those of computations made with the computer codes ERIDEL and RIFF RAFF' (Chapter 4).

Again the rather time-consuming numerical resonance code RIFF RAFF' is used in the important region from 0.8 eV to 37.1 eV whilst computations from 37.1 eV to 1000 eV are made with ERIDEL. Resonance parameters for the resolved region were taken from (22). For the lowest resonance these are  $E_R = 4.906$  eV,  $g = 0.625$ ,  $\Gamma_n = 0.0156$  and  $\Gamma_\gamma = 0.124$  eV. For the contribution of the unresolved

region above 1000 eV a constant value of 6.5 b was added to the resonance integrals (48). The measured and computed values are shown in Fig. 3.1.

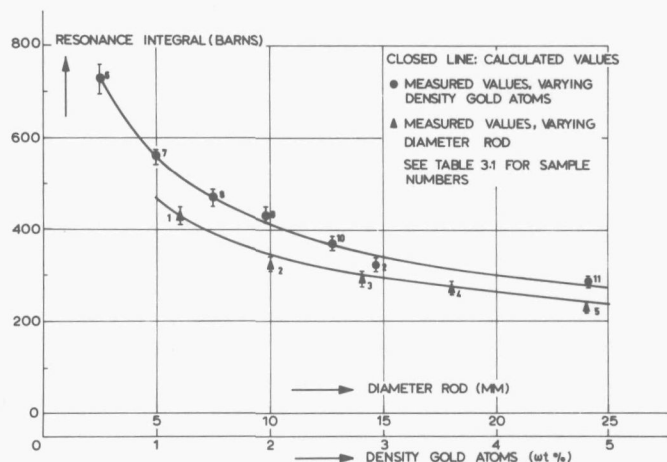


Fig. 3.1. Measured and computed resonance integrals of gold

A satisfying agreement is found on comparison of the values of the resonance integrals in Fig. 3.1. In the measured values the most important error comes from the determination of the number of atoms in the foil. Since this number is relatively small - in the order of  $10^{16}$  atoms - it proved to be difficult to determine it more accurately than to a few percent. This was done by comparing the neutron activation with that of a weighable foil. The errors in the values of  $A_S$  and  $N_S V_S$  are smaller than 0.5%. Therefore the total possible error will be about 4%.

### 3.5.2. Oscillator testing

The results of the oscillator test are given in Fig. 3.2. The values were corrected in accordance with Eq. (3.3). The correction for gamma ray absorption was obtained by oscillating pure lead rods and proved to be about 15%<sup>1</sup>.

The cross-talk from one channel to the other was checked by oscillating an empty sample holder together with one filled

<sup>1</sup>For these early measurements a less optimised neutron detector had to be used.

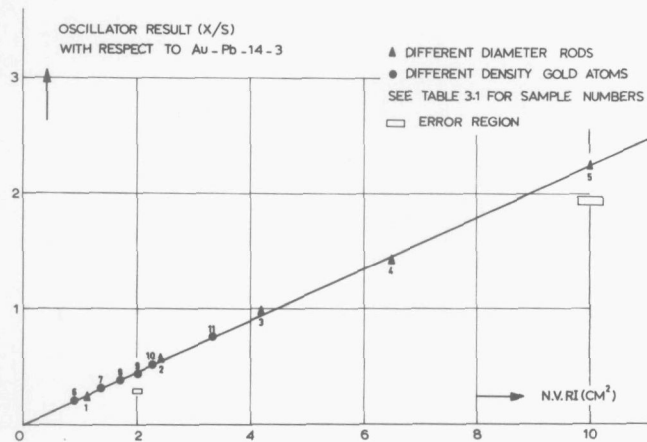


Fig. 3.2. Oscillator results as a function of  
*measured* macroscopic resonance integrals

with a strong absorber. The effect is less than 1% of the contribution of a sample to its own channel. The chamber integral of an empty sample holder is less than 2% of the result for the smallest Au-Pb sample.

### 3.6. Conclusion

The linearity of the apparatus for the test samples is established between the limits given by the measured results. No deviation could be noticed between the result for rods with the same gold-lead composition and different radii and that for rods with the same diameter and varying gold atom densities.



## CHAPTER 4      CALCULATION METHODS

The calculation of resonance absorption and Doppler coefficients with neutron transport codes is handicapped by the enormous number of energy groups needed for a correct representation of the problems. The groups have to be narrow with respect to the mean energy loss in a collision with the heaviest atoms present, as well as to the resonance widths. Moreover a pronounced space dependence of the flux exists at a number of energies. A rough estimate indicates that  $10^5$  or  $10^6$  groups are necessary, which consigns this type of computations to futuristic computer generations.

There are two ways, however, of tackling the problem:

1. the use of transport codes with extensive simplifications;
2. the application of Monte Carlo methods.

Our choice, viz., the first possibility, will be treated in this Chapter. This choice was influenced by the fact that this is the usual way of carrying out these computations, and by the limitations of the available TR-4 computer. As to the Monte Carlo methods, some results for resonance absorption at room temperature could be found in literature sources (23,24,25), but only scarce and partial information could be traced about the computation of Doppler effects (26). Excessive use of computation time will be a limiting factor for more general application of these codes. Since the Monte Carlo method, however, may be considered as being

a rather essential tool for the verification of other codes, we think it will need further attention.

#### 4.1. ERID-II and ZUT

We will first discuss a family of codes in which, as a common approximation, the space dependence of the flux in each cell region is completely disregarded. In a cylindrical two-region cell as shown in Fig. 4.1, the flux in moderator as well as absorber is therefore considered to be *spatially flat* for all energies. Of course, these two flux levels need not be equal.

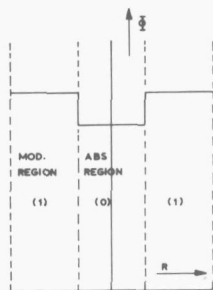


Fig. 4.1.

Two-region cell with flat fluxes

Under these conditions a simplified formula for the resonance integral can be used:

$$RI = \int_0^{\infty} \frac{\Phi}{\Phi_{\infty}}(E) \sigma_a(E) \frac{dE}{E}, \quad (4.1)$$

where  $\frac{\Phi}{\Phi_{\infty}}$  represents the space-independent flux depression in the absorber rod.

In case of well-known cross-sections, the main problem in these computations is therefore to solve the energy-dependent flux depression problem correctly. For this purpose collision density methods are often used.

For a two-region cell, assuming isotropic scattering in the laboratory system, the following collision balance can be used as a starting point

$$V_o F_o(E) = V_o P_{oo} \left\{ \frac{1}{1-\alpha_a} \int_E^{E/\alpha_a} \frac{F_o(E') \Sigma_{sa}}{\Sigma_{to}} \frac{dE'}{E'} + \frac{1}{1-\alpha_{mo}} \int_E^{E/\alpha_{mo}} \frac{F_o(E') \Sigma_{mo}}{\Sigma_{to}} \frac{dE'}{E'} \right\} + V_1 P_{10} \frac{1}{1-\alpha_{m1}} \int_E^{E/\alpha_{m1}} F_1(E') dE', \quad (4.2)$$

with  $F_0$  and  $F_1$  representing collision densities in absorber and moderator region,  
 $P_{00}$  the non-escape probability from the inner region,  
 $P_{10}$  the escape probability from the outer region,  
 $\alpha_a$ ,  $\alpha_{m0}$  and  $\alpha_{m1}$  the factors  $\left(\frac{A-1}{A+1}\right)^2$  for absorber, rod moderator and outer moderator,  
 $\Sigma_{sa}$  the macroscopic scattering cross-section of the absorber material,  
 $\Sigma_{mo}$  the macroscopic scattering cross-section of the rod moderator material,  
and  $\Sigma_{to}$  the macroscopic total cross-section in the rod.

Eq. (4.2) is valid for cells with one absorbing nuclide in the rod, which is mixed with one *non-absorbing* moderator nuclide. In the reflector region one *non-absorbing* nuclide is present. It is easily possible to extend the formula to cells with more isotopes.

Well-known approximations are often used to simplify the integral forms in Eq. (4.2), in the case where the cross-sections exhibit resonances (constant or  $\frac{1}{v}$ -cross-sections allow trivial solutions).

These approximations are:

1. the NR (narrow resonance) solution.

It is assumed that the maximum energy decrease of a neutron after collision ( $= (1-\alpha)E'$ ) is large compared to the resonance width. For  $F_0(E')$  the undisturbed value  $\frac{\Sigma_{to}}{E'}$  may be used, whilst  $\Sigma_{sa} \rightarrow \Sigma_{pa}$ . In this case

$$\frac{1}{1-\alpha_a} \int_E^{E/\alpha_a} \frac{F_0(E') \Sigma_{sa}}{\Sigma_{to}} \frac{dE'}{E'} \approx \frac{\Sigma_{pa}}{1-\alpha_a} \left[ -\frac{1}{E'} \right]_E^{E/\alpha_a} = \frac{\Sigma_{pa}}{E} \quad (4.3)$$

2. the IM (infinite mass) solution.

It is supposed that a scattering hardly changes the neutron energy, so the energy decrease is really small compared to

the resonance width. In that case  $F_0(E')$  as well as  $\Sigma_{sa}$  may be considered to be constant, hence

$$\begin{aligned} \frac{1}{1-\alpha_a} \int_E^{E/\alpha_a} \frac{F_0(E') \Sigma_{sa}}{\Sigma_{to}} \frac{dE'}{E'} &\sim \lim_{\alpha_a \rightarrow 1} \frac{F_0 \Sigma_{sa}}{\Sigma_{to}} \frac{1}{1-\alpha_a} \left[ \ln E \right]_E^{E/\alpha_a} \\ &\sim \frac{F_0 \Sigma_{sa}}{\Sigma_{to}} \lim_{\alpha_a \rightarrow 1} \frac{1}{1-\alpha_a} \ln \frac{1}{\alpha_a} \\ &\sim \frac{F_0 \Sigma_{sa}}{\Sigma_{to}} \cdot \end{aligned} \quad (4.4)$$

For the contribution of the moderator region to the collision density in the rod, the NR-approximation is nearly always used (ZUT, ERIDEL). This is correct in view of the normally low mass numbers of the moderating atoms (H,O,C).

In the computer code ZUT (27,28) a total number of one absorbing and two moderating isotopes is allowed in the absorber rod. For each integral in Eq. (4.2) the desired solution method can be selected: NR-, IM-treatment or an "exact" solution in which the integration region is divided into small energy groups. Therefore we may say that with this code a nearly perfect solution of Eq. (4.2) can be obtained. As has been mentioned, this formula is based, however, on a number of approximations. The ZUT-code, originally written in the FORTRAN computer language was translated by us into ALGOL for use on the Delft TR-4 computer (29).

In the code ERIC-II (30) an unlimited number of moderator materials is allowed as well in the rod as in the moderator region. The NR-approximation is applied to all of these. Eq. (4.2) becomes

$$\begin{aligned} V_0 F_0(E) = V_0 P_{00} &\left\{ \frac{1}{1-\alpha_a} \int_E^{E/\alpha_a} \frac{F_0(E') \Sigma_{sa}}{\Sigma_{to}} \frac{dE'}{E'} \right\} + \frac{V_0 P_{00}}{E} \sum_{i=1}^n \Sigma_{moi} + \\ &+ \frac{V_1 P_{10}}{E} \sum_{j=1}^m \Sigma_{mlj} \cdot \end{aligned} \quad (4.5)$$

If the reciprocity theorem is introduced, which reads (37)

$$V_0 \Sigma_{01} P_{01} = V_1 \Sigma_{10} P_{10} \quad (4.6)$$

and the Dancoff effect, describing the mutual interference

between different absorber rods is supposed to be negligible, hence,

$$P_{01} = 1 - P_{00} , \quad (4.7)$$

Eq. (4.5) can be simplified to

$$\phi_0(E) = \frac{P_{00}}{\Sigma_{to}} \int \frac{E/\alpha_a}{E} \frac{\Sigma_{sa} \phi_0(E')}{1-\alpha_a} \frac{dE'}{E'} + \frac{P_{00}}{E \Sigma_{to}} \sum_{i=1}^n \Sigma_{mi} + \frac{1-P_{00}}{E} , \quad (4.8)$$

where the subscript moi is replaced by mi for simplicity.

Writing  $\phi_1 = \frac{1}{E}$ , and applying the NR-approximation to the absorber:

$$\frac{\phi_0}{\phi_1} = \frac{P_{00}}{\Sigma_{to}} (\Sigma_{pa} + \sum_{i=1}^n \Sigma_{mi}) + 1 - P_{00} . \quad (4.9)$$

The IM-approximation for the absorber applied to (4.8) yields

$$\begin{aligned} \phi_0 &= \frac{P_{00}}{\Sigma_{to}} \phi_0 \Sigma_{sa} + \phi_1 \left( \frac{P_{00}}{\Sigma_{to}} \sum_{i=1}^n \Sigma_{mi} + 1 - P_{00} \right) , \\ \frac{\phi_0}{\phi_1} &= \frac{\frac{P_{00}}{\Sigma_{to}} \sum_{i=1}^n \Sigma_{mi} + 1 - P_{00}}{1 - \frac{P_{00}}{\Sigma_{to}} \Sigma_{sa}} . \end{aligned} \quad (4.10)$$

In both Eqs. (4.9) and (4.10) we substitute the Wigner rational approximation for  $P_{00}$ , which reads

$$P_{00} = \frac{\Sigma_{to} \bar{l}}{1 + \Sigma_{to} \bar{l}}$$

(5,6), where  $\bar{l}$  represents the average chord length in the absorber rod ( $\bar{l} = \frac{4V}{S}$ , (37)). Equation (4.9) can then be rewritten as

$$\frac{\phi_0}{\phi_1} = \frac{\sigma_{pa} + \sum_{i=1}^n \frac{N_i}{N} \sigma_{mi} + \frac{1}{N\bar{l}}}{\sigma_{to} + \frac{1}{N\bar{l}}} \quad (4.11)$$

(N is the absorber atom density) and Eq. (4.10) becomes

$$\frac{\phi_0}{\phi_1} = \frac{\sum_{i=1}^n \frac{N_i}{N} \sigma_{mi} + \frac{1}{N\bar{1}}}{\sigma_{to} - \sigma_{sa} + \frac{1}{N\bar{1}}} . \quad (4.12)$$

Introducing a dimensionless auxiliary quantity  $\lambda$  ( $0 \leq \lambda \leq 1$ ), the so-called Goldstein-Cohen parameter (32) permits us to combine Eqs. (4.11) and (4.12) giving

$$\frac{\phi_0}{\phi_1} = \frac{\lambda \sigma_{pa} + \sum_{i=1}^n \frac{N_i}{N} \sigma_{mi} + \frac{1}{N\bar{1}}}{\sigma_a + \lambda(\sigma_{pa} + \sigma_{rsa} + \sigma_{int}) + \sum_{i=1}^n \frac{N_i}{N} \sigma_{mi} + \frac{1}{N\bar{1}}} . \quad (4.13)$$

with  $\sigma_{int}$  representing the interference between the potential scattering ( $\sigma_{pa}$ ) and the resonance scattering term of the absorber ( $\sigma_{rsa}$ ), whilst  $\sigma_a$  denotes the absorption cross-section of the absorber material.

For  $\lambda=1$ , Eq. (4.13) is reduced to the NR-approximation for  $\frac{\phi_0}{\phi_1}$  (Eq. (4.11)); with  $\lambda=0$  we get the IM-approximation (Eq. (4.12)). Furthermore when

$$\sigma_m = \lambda \sigma_{pa} + \sum_{i=1}^n \frac{N_i}{N} \sigma_{mi} + \frac{1}{N\bar{1}} , \quad (4.14)^1$$

Eq. (4.13) can be simplified to

$$\frac{\phi_0}{\phi_1} = \frac{\sigma_m}{\sigma_a + \lambda(\sigma_{rsa} + \sigma_{int}) + \sigma_m} . \quad (4.15)$$

In the ERIC-II code an intermediate  $\lambda$ -value is determined for each individual resonance, the absorption of which has to be computed. For the methods which may be used to determine this factor  $\lambda$ , reference is made to the original publication (32). It is worthwhile to note that ERIC-II includes no direct possibility of computing resonance overlapping effects.

Inserting Eq. (4.15) in Eq. (4.1) we get

$$RI = \int_0^{\infty} \frac{\sigma_a \sigma_m}{\sigma_a + \lambda(\sigma_{rsa} + \sigma_{int}) + \sigma_m} \frac{dE}{E} . \quad (4.16)$$

<sup>1</sup>The factor  $\frac{1}{N\bar{1}}$  is sometimes referred to as  $\sigma_{ex}$ .

The well-known expressions for the Doppler-broadened cross-sections of a non fissionable absorber are (6,30):

$$\sigma_a = \sigma_o \frac{\Gamma_\gamma}{\Gamma} \sqrt{\frac{|E_R|}{E}} \psi(\xi, x) \quad \left\{ x = \frac{E-E_R}{\Gamma/2}, \xi = \frac{\Gamma}{\sqrt{\frac{4kTE}{M}}} = \frac{\Gamma}{\Delta} \right\}$$

$$\sigma_{rs} = \sigma_o \frac{\Gamma_n}{\Gamma} \psi(\xi, x) \quad (4.17)$$

$$\sigma_{int} = \sqrt{\sigma_{pa} \sigma_o g \Gamma_n / \Gamma} \chi(\xi, x)$$

$$\sigma_o = \frac{2.6 \cdot 10^6}{E_R} g \frac{\Gamma_n}{\Gamma}$$

$\sigma_o$  represents the top cross-section of the unbroadened resonance (T=0 K), at the energy  $E_R$ .

$\Gamma_\gamma$ ,  $\Gamma_n$  and  $\Gamma$  are the resonance gamma-, neutron- and total widths.

Three approximations are introduced at this point:

$$A. \quad \int \frac{\sigma_a \sigma_m}{\sigma_a + \lambda(\sigma_{rsa} + \sigma_{int}) + \sigma_m} \frac{dE}{E} \approx \frac{1}{E_R} \int \frac{\sigma_a \sigma_m}{\sigma_a + \lambda(\sigma_{rsa} + \sigma_{int}) + \sigma_m} dE \quad (4.18)$$

$$B. \quad \sigma_a = \sigma_o \frac{\Gamma_\gamma}{\Gamma} \sqrt{\frac{|E_R|}{E}} \psi(\xi, x) \approx \sigma_o \frac{\Gamma_\gamma}{\Gamma} \psi(\xi, x) \quad (4.19)$$

Both approximations may be used for narrow resonances at higher energies, but may produce errors for wide low-energy resonances (sect. 4.3).

C. Interference between potential and resonance scattering is disregarded.

Equation (4.16) can now be developed to:

$$RI \approx \frac{\sigma_m \Gamma}{2E} \int_{-E_R/\Gamma}^{\infty} \frac{\sigma_o \frac{\Gamma_\gamma}{\Gamma} \psi}{\sigma_o \frac{\Gamma_\gamma}{\Gamma} \psi + \lambda \sigma_o \frac{\Gamma_n}{\Gamma} \psi + \sigma_m} d(E-E_R)/\frac{\Gamma}{2} \quad (4.20)$$

$$\begin{aligned}
&\approx \frac{\sigma_m \Gamma}{2E_R} \int_{-\infty}^{+\infty} \frac{\psi \Gamma_\gamma}{\psi \Gamma_\gamma + \lambda \Gamma_n \psi + \frac{\sigma_m}{\sigma_o} \Gamma} dx \\
&\approx \frac{\sigma_m \Gamma_\gamma \Gamma}{2E_R (\Gamma_\gamma + \lambda \Gamma_n)} \int_{-\infty}^{+\infty} \frac{\psi}{\psi + \frac{\sigma_m}{\sigma_o} \frac{\Gamma}{\Gamma_\gamma + \lambda \Gamma_n}} dx \\
&\approx \frac{\sigma_m \Gamma_\gamma \Gamma}{2E_R (\Gamma_\gamma + \lambda \Gamma_n)} \int_{-\infty}^{\infty} \frac{\psi(x, \xi)}{\psi(x, \xi) + \beta'} dx \quad (\beta' = \frac{\sigma_m}{\sigma_o} \frac{\Gamma}{\Gamma_\gamma + \lambda \Gamma_n}) \quad (4.21)
\end{aligned}$$

$$\approx \frac{\sigma_m \Gamma_\gamma \Gamma}{E_R (\Gamma_\gamma + \lambda \Gamma_n)} J(\xi, \beta') \quad (J(\xi, \beta') = \frac{1}{2} \int_{-\infty}^{+\infty} \frac{\psi(x, \xi)}{\psi(x, \xi) + \beta'} dx) \quad (4.22)^1$$

The function  $J$  has been tabulated by several authors (6, 27, 33). We used the method of Amster (34) and Ferziger et al. (35) for the computation of  $J$ , the results of which we compared with those of a method based on the  $\psi$ -calculation by O'Shea and Thacher (36) and with the tabulated results mentioned above. A deviation of not more than 1% was found for  $0.01 < \xi < 10$  and  $10^{-5} < \beta' < 10^4$ .

Fig. 4.2 shows some of our computed results. ERIC-II has been programmed in the FORTRAN language. Our ALGOL transcription can be obtained on request (30).

#### 4.1.1. The ERIDEL-code<sup>3</sup>

The supposition in the ERIC-II code that all moderator materials may be considered as NR-scatterers, is not valid in a number of cases. Most important examples in this respect

<sup>1</sup>The parameter  $\xi$  is taken at  $E = E_R$ .

<sup>2</sup>There is one exception: the tabulated values of Kuncir (27) for  $J(0.01, 0.00062)$ ,  $J(0.01, 0.00045)$  and  $J(0.01, 0.00032)$  are about 4% higher than the values computed by us with both methods. These extreme low parameters of  $J$  will, however, not appear in any realistic case of resonance absorption.

<sup>3</sup>ERIDEL is an abbreviation of ERIC-DELFT.

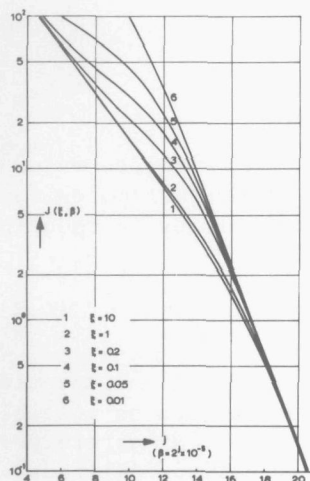


Fig. 4.2.

The Doppler broadening function  $J(\xi, \beta)$

are the wide low-energy resonances in  $^{238}\text{U}$ , which are not narrow compared with the energy decrease following a neutron collision with the oxygen atoms in  $\text{UO}_2$ , which means that  $\lambda$  will be smaller than 1. Therefore in our code ERIDEL (37), we included a second Goldstein-Cohen parameter computation for moderator atoms in the absorber region (Table 4.1). This possibility was already indicated by Sumner (30). Another point which attracted our attention was the validity of the "rational approach". The

Table 4.1. Goldstein-Cohen parameters for  $^{238}\text{U}$  en O in  $\text{UO}_2$ , diam. rod 6 mm

$E_R$ (eV)	$\Gamma_n$ (eV)	$\Gamma_\gamma$ (eV)	$\lambda(\text{U})$	$\lambda(\text{O})$
6.68	0.001486	0.026	0.020	0.622
21.0	0.009	0.026	0.060	0.799
36.8	0.0334	0.026	0.064	0.805
66.3	0.0234	0.026	0.297	0.930
102.8	0.066	0.026	0.266	0.923
190.5	0.144	0.026	0.346	0.939

formula

$$P_{01} = \frac{1}{1 + \Sigma_{t0} \bar{l}}$$

is correct in the extreme cases, but for intermediate values of  $\Sigma_{t0} \bar{l}$ , the escape probabilities will be underestimated for maximally 20%. Bell (38) tried to correct this by introducing a constant factor  $a$ ,

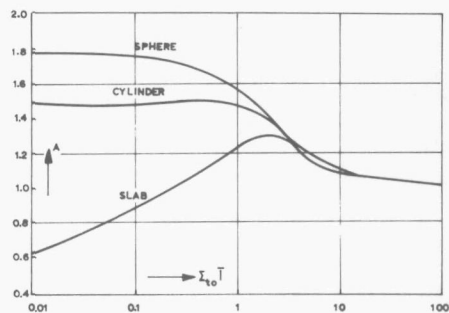
$$P_{01} = \frac{1}{1 + \Sigma_{t0} \bar{l}/a} \quad (4.23)$$

This "a" is chosen in such a way that the analytical computation results for resonance absorption coincide as much as possible with those of Monte Carlo codes. Leslie c.s. (39) determine this Bell-factor "a" as 1.20 for isolated cylindrical rods. A more sophisticated method has been suggested by Kelber (40), who introduced a function  $A(\Sigma_{t0} \bar{l})$  such that  $P_{01}$  for unbroadened cross-section contours is given exactly by

$$P_{01} = \frac{1}{1 + \Sigma_{t0} \bar{l}/A(\Sigma_{t0} \bar{l})} \quad (4.24)$$

This function is drawn in Fig. 4.3. By combining a number of values for the exact escape probability at carefully selected points in the resonance peak, a mean value for  $A$  can be determined which differs, of course, from peak to peak. We incorporated this method in ERIDEL. It is emphasised that this method is not yet perfect, as it is based on unbroadened cross-sections, or in other words, determines a temperature-independent Bell-factor.

Fig. 4.3.  
Bell-function for three geometries (38)



The ERIDEL-code was used for a number of computations which are described in the following sections. Apart from some deviations at lower neutron energy (sect. 4.3), agreement was found between the predictions of the code and the experimental results within the respective error margins. However, the ERIDEL Doppler-effects tend to be systematically on the higher side.

#### 4.2. The RIFF RAFF'-code

Some limitations of the foregoing codes are eliminated in the RIFF RAFF code which was developed by Kier (41). The flat-flux representation is replaced by an approximate representation of the flux as

$$\phi_i(r) = \sum_{n=0}^2 \phi_{in} \left(\frac{r}{a}\right)^{2n}, \quad \begin{array}{l} i = 0 \text{ for the rod,} \\ i = 1 \text{ for the} \\ \text{moderator,} \end{array} \quad (4.25)$$

with  $a$  representing the rod radius.

Furthermore the number of resonance absorbers is theoretically unlimited, and overlapping effects are included as will become obvious later in this chapter. In this method the energy region under consideration is divided into very small parts ( $<0.002$  lethargy units), so that the probability of a neutron colliding two times in one and the same group is practically zero. Beginning with an energy region where an asymptotic (flat) flux is assumed, the source distribution in the nearest small group is determined using the simple model of *isotropic scattering in the laboratory system*. In the small group the several cross-sections are read in, or computed using Eqs. (4.17) for each individual resonance and summing up the results for different peaks and absorbing isotopes. Thus overlap of resonances is fully included. Then the source distribution is converted into a flux distribution, following the method of Cady and Clark (42), who, by taking the spatial moments of the flux that results from a particular source distribution, have been able to obtain  $\phi_{on}$  in the form:

$$\phi_{on} = c_n S_s + \sum_{j=0}^2 c_{nj} S_{oj}, \quad (4.26)$$

where  $S_s$  represents the surface source impinging on the outer side of the absorber rod. It is computed from the source distribution in the moderator and the cross-

section data for this medium.

$c_{nj}$  represents the contribution to flux coefficient  $\phi_{on}$  from source neutrons distributed according to  $(\frac{r}{a})^{2j}$  (the inner source is developed in the same way as  $\phi_1$  (4.25)), and  $c_n$  is the contribution to flux coefficient  $\phi_{on}$  from the surface source, which is assumed to be isotropic.

The constants  $c_{nj}$  and  $c_n$  are tabulated as functions of the rod radius in mean free path units.

The following three conditions make it possible to find the moderator flux

1. equality of the fluxes at the interface

$$\phi_0(a) = \phi_1(a) ,$$

2. neutron conservation

$$\Sigma_1 \int_{V_1} \phi_1(r) dV = \int_{V_1} S_1(r) dV + \int_{V_0} S_0(r) dV - \text{collision rate in the rod ,}$$

3. the derivative of  $\phi_1(r)$  vanishes at the cell surface b

$$\frac{d}{dr} \phi_1(b) = 0 .$$

Absorption rates, etc. in the small group can be computed once the neutron fluxes are known. When the computations for one small group have been finished the results can be used in the treatment of the next group. The resonance integral for process  $z$  in material  $j$  is

$$RI_{zj} = \frac{\text{reaction rate } zj}{\phi_{\infty} N_j V_{\text{rod}}} \quad (4.27)$$

according to the definition given in sect. 2.1.2.

All our measurements described in this work concern unreflected single absorber rods. We therefore needed a special version of the RIFF RAFF code for computations on unreflected rods. This special code is indicated from now on by RIFF RAFF'. It was made by removing the moderator part, and introducing a surface source  $S_s$  which is constant for each lethargy unit. This means, of course, that the absorber rod is placed in an undisturbed

isotropic  $\frac{1}{E}$ -flux. Any other lethargy dependence of the surface flux can, however, be programmed too.

The code descriptions as they were given in sect. 4.1 and 4.2 are only schematic. For more complete information the reader is again referred to (30) (ERIC-II), (37) ERIDEL and (47) (RIFF RAFF).

#### 4.3. Comparison of the codes

##### 4.3.1. Discussion of some special computation results

A number of computations has been carried out on the 36.7 eV resonance in  $^{238}\text{U}$ . This resonance is interesting in view of its comparatively large neutron width, which is why neutron scattering within the resonance region is of notable importance. In all cases the partial resonance integral from 28 eV to 45 eV was determined for this resonance, using the following resonance data

$$\begin{aligned} E_R &= 36.7 \quad \text{eV} , \\ \Gamma_\gamma &= 0.025 \quad \text{eV} , \\ \Gamma_n &= 0.031138 \quad \text{eV} . \end{aligned}$$

Table 4.2. Partial resonance integrals for the 36.7 eV resonance in  $^{238}\text{U}$

temperature	computation number							
	1	2	3	4	5	6	7	8
293 K	1.584	1.645	1.635	1.460	1.460	1.454	1.406	1.468
793 K	1.612	1.673	1.663	1.494		1.487	1.439	1.513
$\Delta$	0.028	0.028	0.028	0.034		0.033	0.033	0.045

1 : RIFF RAFF'

2 : RIFF RAFF', but with flat-flux approximation

3 : ZUT

4 : RIFF RAFF', no interference, flat fluxes

5 : As 4, but  $\Delta u = 0.0002$  instead of 0.0010

6 : ZUT, no interference

7 : RIFF RAFF', no interference

8 : ERIDEL

Further data: radius of the  $^{238}\text{U}$  rod : 0.5 cm  
 number of atoms per  $\text{cm}^3$ :  $0.04749 \cdot 10^{24}$   
 small group width : 0.001 lethargy units  
 potential scattering  
 cross-section : 10.64 b

For the temperature effect  $\Delta$ , a good agreement is found between the results for the ZUT and RIFF RAFF' code, but the introduction of curved fluxes in RIFF RAFF' tends to reduce the partial resonance integrals at both temperatures by a few percent. This is in accordance with the results of Lewis (43), who also found an overestimation for the resonance absorption in flat-flux approximation in his computations on moderated rods. For the rather strongly scattering 36.7 eV resonance, neglect of the potential scattering-resonance scattering interference leads to a serious underestimation of the result. The agreement between the columns 4 and 8 is good for cold absorption, but an important difference, which will be discussed in sect. 4.3.2, is noted as to the temperature dependence.

In Table 4.3, the special "flat-flux, no-interference" version of RIFF RAFF' is further compared with ERIDEL and ZUT. This comparison is carried out for four specific resonances in a 0.422 cm radius  $^{238}\text{U}$  rod,  $\sigma_p = 10.64$  b,  $N = 0.04783 \cdot 10^{24}$  atoms/ $\text{cm}^3$ .

Apart from some smaller deviations, the most striking point in Table 4.3 is the pronounced effect of approximations A and B on the resonance integral of the lowest resonance of  $^{238}\text{U}$  (columns 1, 2 and 3). For this wide low-energy resonance the conditions necessary for the approximations to be correct are not fulfilled. In some codes which include these approximations this deviation is not immediately visible thanks to the selection of a suitable low cut-off energy (Sumner, (30)) or the addition of a properly selected  $\frac{1}{v}$ -contribution (Fillmore, (44)), in order to make the computed resonance integral of an isotope coincide with known data. In this respect, use can be made of computations for the non-shielded ("infinite dilution") resonance integral  $RI_\infty$  which can be made accurately. The phenomenon is clearly demonstrated in Table 5.1, too.

Table 4.3. Partial resonance integrals for four specific resonances  
in  $^{238}\text{U}$

		1	2	3	4	5
$E_R = 6.68$ eV						
$\Gamma_Y = 0.024$ eV						
$\Gamma_n = 0.00148$ eV	T = 293 K	5.030	4.803	4.607	4.547	4.953
RI 1-11 eV	T = 793 K	5.115	4.887	4.692	4.673	5.036
$\Delta u = 0.00196$	$\Delta$	0.085	0.084	0.085	0.126	0.083
$E_R = 81$ eV						
$\Gamma_Y = 0.024$ eV						
$\Gamma_n = 0.0021$ eV	T = 293 K	0.251	0.251	0.251	0.252	0.251 <sup>1</sup>
RI 65-87 eV	T = 793 K	0.329	0.329	0.329	0.329	-
$\Delta u = 0.0007$	$\Delta$	0.078	0.078	0.078	0.077	
$E_R = 103$ eV						
$\Gamma_Y = 0.024$ eV						
$\Gamma_n = 0.072$ eV	T = 293 K	0.412	0.411	0.409	0.436	0.424 <sup>1</sup>
RI 80-110 eV	T = 793 K	0.435	0.434	0.432	0.466	-
$\Delta u = 0.0002$	$\Delta$	0.023	0.023	0.023	0.030	
$E_R = 475$ eV						
$\Gamma_Y = 0.024$ eV						
$\Gamma_n = 0.005$ eV	T = 293 K	0.0434	0.0434	0.0434	0.0408	0.0431 <sup>1</sup>
RI 450-482 eV	T = 793 K	0.0516	0.0516	0.0516	0.0487	-
$\Delta u = 0.0002$	$\Delta$	0.0082	0.0082	0.0082	0.0079	

The codes and extra approximations used are:

- 1 : RIFF RAFF', flat-flux, no interference      4 : ERIDEL  
 2 : as in point 1 but with ERIC-II approximation B      5 : ZUT, no interference  
 3 : as in point 1 but with ERIC-II approximations A and B<sup>2</sup>

<sup>1</sup>T = 300 K, results from Nordheim (28)

<sup>2</sup>For approximations A and B see section 4.1

#### 4.3.2. Temperature dependence

A marked difference exists, especially for the low energy resonances, between the  $\Delta$  values for RIFF RAFF' and ERIDEL. This is only partly caused by the inclusion of scattering interference in RIFF RAFF' (Table 4.2), which type of interference is disregarded in ERIC-II as well as in ERIDEL (sect. 4.1). We will reconsider RIFF RAFF' and ERIDEL for the purpose of discussing this difference more thoroughly.

##### 4.3.2.1. ERIDEL temperature dependence

To throw some light on the relatively large temperature effects in the low-energy resonance absorption computed with ERIDEL it is useful to take into consideration the fact that both the Goldstein-Cohen parameter and the Bell-factor are computed from the unbroadened cross-sections ( $T=0$  K). These parameters are therefore independent of the sample temperature. At higher temperatures a resonance becomes broader, approaching the wide resonance concept for which  $\lambda$  is zero, and thus  $\lambda$  ought to have a lower value at elevated temperatures. If, for a specific resonance

$$\frac{\sigma_{\text{ex}}}{\sigma_{\text{p}}} < \frac{\Gamma_{\text{y}}}{\Gamma_{\text{n}}}, \quad (4.28)$$

then the NR-value for the resonance integral will be higher than the IM-value (32). For our samples Eq. (4.28) generally holds for the dominant resonances at lower energies, which can be verified considering the values of the resonance parameters and  $\sigma_{\text{p}}$  (see e.g. (7)), and  $\sigma_{\text{ex}}$  (which is equal to  $1/N\bar{l}$ ). Therefore a non-variable  $\lambda$  will result in a value which is too high for the resonance integrals at higher temperatures and thus in a too high value for the temperature effects. The constant Bell-factor will exert the same influence as can be concluded from Fig. 4.3. The general flattening of the absorption cross-sections at elevated temperatures will have no great effect on the Bell-factor at the top of most resonances where  $\Sigma_{\text{t}0}\bar{l} > 10$ . But, at the wings of the resonances, where the cross-sections increase at higher temperatures, the Bell-factor might have to be appreciably decreased. This would make  $\sigma_{\text{m}}$  smaller, resulting in a smaller resonance absorption. So the constancy of the Bell-factor might result in an *over-estimation of the temperature effect*. These phenomena are now being considered more quantitatively (45). This work is tire-

some due to the fact that with more complicated assumptions it becomes more and more difficult to solve Eq. (4.2) analytically.

#### 4.3.2.2. RIFF RAFF' temperature dependence

Many of the approximations involved in ERIDEL have been eliminated in RIFF RAFF'. In the remainder we are confronted with a most important problem as to whether the simple polynomial flux representation as given in Eq. (4.25) may be considered as sufficient under all conditions.

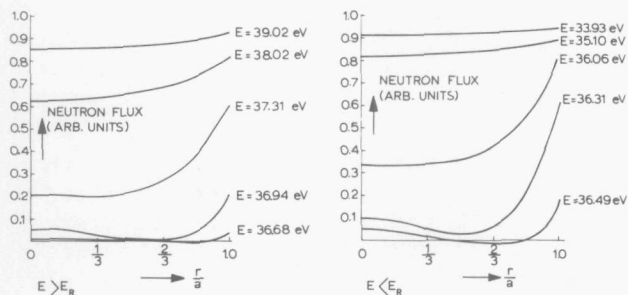


Fig. 4.4. Radial flux plots in a  $^{238}\text{U}$ -cylinder computed with RIFF RAFF'

It is obvious from Fig. 4.4, where computed flux plots are given for a number of energies in the 36.7 eV resonance of  $^{238}\text{U}$ , that the representation is far from exact. We consider here a  $^{238}\text{U}$  cylinder having a diameter of 1 cm. Under some circumstances the flux may even have a negative value (36.49 eV). This gives no reason for concern as the main demand for a proper computation of the absorption in the rod is that the integral neutron transport from group to group is described correctly. This is generally so for  $r < 5\lambda$  (42), where the flux plots indeed have an acceptable form. For higher absorption in the rod (quite normal in resonance peaks) the actual flux profile is much steeper near the rod boundary than the flux representation according to Eq. (4.25) can describe. Let us take as an example a very steep RIFF RAFF' flux distribution which would read

$$\phi = \phi_0 \left(\frac{r}{a}\right)^4, \quad (4.29)$$

where  $\phi_0$  is the flux on the rod boundary.

From Eq. (4.29) follows

$$\frac{d\phi}{dr} = 4 \phi_0 \frac{r^3}{a^4} \rightarrow \left(\frac{d\phi}{dr}\right)_{r=a} = \frac{4}{a} \phi_0$$

This may be compared to the flux distribution resulting from a mono-energetic flux bundle impinging perpendicular on a flat surface of a purely absorbing medium

$$\phi = \phi_0 e^{-\Sigma x} ,$$

$$\frac{d\phi}{dx} = -\Sigma \phi_0 e^{-\Sigma x} ,$$

$$\left|\frac{d\phi}{dx}\right|_{x=0} = \Sigma \phi_0 .$$

From this comparison, it may be roughly concluded that the flux representation can be approximately correct for values of  $\Sigma a$  smaller than 5, as was noted by Cady and Clark (42). For a 10 mm diameter  $^{238}\text{U}$  rod, however, the product  $\Sigma a$  reaches values of more than 100 in the resonance tops. When the RIFF RAFF' code is used for the computation of resonance absorption, it has to be noted that the flux representation in the resonance tops will be only slightly better than the flat-flux representation.

It is generally known that the usefulness of the flat-flux representation must be based partly on a cancelling of errors (28). The actual escape probability from the rod is larger than the computed one due to the flux peaking near the boundary. This leads to an overestimation of the flux in the absorber region, and thus of the resonance absorption. On the other hand an error of opposite sign is introduced in the codes by the supposition of isotropic scattering in the laboratory system. Anisotropic scattering would tend, especially in the case of a moderated rod, to top up the flux dips at resonance energies in the absorber. Thus the simplified scattering kernel causes an underestimation of the resonance absorption.

Where both approximations are of equal magnitude for reflected rods, the first one must be dominant in the case of bare absorber rods.

The phenomena are relatively small compared with the resonance integrals, as follows from the good agreement for bare absorber rods between measured and computed resonance integrals at room temperature (sect. 5.2.3). However, for the temperature dependence, which is quite small compared with the resonance integrals, the effect of the spatial flux approximation may be evident. As the effect diminishes at higher temperatures, where the cross-sections are not as high as in the case of room temperature we must expect an *under-estimation of the Doppler effect* for the RIFF RAFF' computations on bare absorber rods.



CHAPTER 5      CALCULATIONS OF RESONANCE INTEGRALS AND DOPPLER  
COEFFICIENTS; COMPARISON WITH REFERENCE VALUES

5.1. *Materials and rod dimensions which have been considered*

The experiments with the local oscillator which are described in Chapter 6 were performed on natural uranium metal rods (U), depleted (to 0.21%  $^{235}\text{U}$ ) uranium metal rods (UD), natural uraniumdioxide rods ( $\text{UO}_2$ ) and thorium rods. All cylinders were 90 mm long. The diameter in mm of each rod is mentioned in the codification after the material indication. The following samples were at our disposal:

U6, U8, U10, U12, U14, U16, U18, U20, U22, U24,  
UD10, UD16,  
 $\text{UO}_2$ 10,  $\text{UO}_2$ 12,  $\text{UO}_2$ 14,  $\text{UO}_2$ 16,  $\text{UO}_2$ 18,  $\text{UO}_2$ 20,  
Th10, Th12, Th14, Th16, Th18, Th20.

The computations generally concerned these sample rods. From the results graphs have been constructed which indicate empirical relations for the specific materials. As a by-product of the computations on U and  $\text{UO}_2$ , results for pure  $^{238}\text{U}$  and  $^{238}\text{UO}_2$  were obtained. These are quoted in this chapter as resonance integrals and Doppler coefficients which could be compared with reference results. They are not mentioned in Chapter 6 as chamber values because they could not be compared with local oscillator measurements.

## 5.2. Resonance integrals and Doppler coefficients for uranium, uraniumdioxide and thorium

### 5.2.1. Application of the codes

Above approximately 200 eV, the effect of most approximations in the described codes diminishes strongly. The resonances assume more and more an NR-character<sup>1</sup>, so  $\lambda$  approaches 1. In RIFF RAFF the flux representation becomes more and more correct when the resonances becomes lower and broader. This is illustrated in Table 5.1.

Table 5.1. Partial resonance integrals for U8

energy region (eV)	RI(barns)		$\Delta$ RI(barns) T=293 K $\rightarrow$ T=793 K	
	ERIDEL	RIFF RAFF	ERIDEL	RIFF RAFF
3.5 - 7.5	4.586	4.904	0.303	0.165
7.5 - 37.1	4.193	4.306		
37.1 - 183.6	2.672	2.666	0.322	0.290
183.6 - 408.7	0.874	0.886	0.171	0.164

The code RIFF RAFF consumes much computer time due to the very small lethargy groups which are used. Therefore it was decided to use RIFF RAFF<sup>1</sup> only in the interval 0.55 eV to 183.6 eV, in order to avoid the approximations A and B of ERIDEL in this region. Above 183.6 eV the computations could be made with the latter, more simple code<sup>2</sup>.

<sup>1</sup>This can be easily understood when we consider the fact that although the resonances become wider ( $\Gamma_n \sim \Gamma_{no} \sqrt{E}$ ), the mean energy loss per neutron collision increases relatively more rapidly with increasing neutron energy ( $\Delta E = \frac{E(1-\alpha)}{2}$ ).

<sup>2</sup>For the computations concerning gold-poisoned lead samples at room temperature (sects. 2.3 and 3.5.1) ERIDEL could be used from 37.1 eV on, mainly because the 4.9 eV resonance is dominating the results (contribution to the resonance integrals more than 75%).

The determination of Doppler coefficients was approached in two different ways, viz.:

1. with ERIDEL for the whole energy range;
2. with RIFF RAFF' from 0.55 eV to 183.6 eV and ERIDEL for the higher energies.

The temperature effects on the resonance integrals as determined in these two ways were divided by the cold resonance integrals computed by method 2 only. In the second case ERIDEL results contribute less than 20% to the resonance integrals, and far less to the chamber integrals.

Above 4 keV, for uranium as well as thorium, the resonance parameters are not yet known in sufficient detail in this the so-called "unresolved" region. We used the ERIC-II code here in its original form (30), which generates simulated resonance parameters on the basis of an assumed Porter-Thomas distribution of the neutron widths. The method is identical to that used in the well-known TUZ-code (27).

The isotope  $^{235}\text{U}$  needs special treatment because the resonance peaks of  $^{235}\text{U}$  are very close to each other (mean level spacing  $\bar{D} \approx 0.5$  eV). The one-level Breit-Wigner formula for the description of resonance cross-sections is less correct for this situation. Therefore we used numerical values for the  $^{235}\text{U}$  cross-sections, which were read in for RIFF RAFF' computations. Thus the results for  $^{235}\text{U}$ -absorption originate from this code exclusively. For the high energy region above 183.6 eV the infinitely diluted  $^{235}\text{U}$  resonance integral was used, because shielding effects will be small for  $^{235}\text{U}$  enrichments below 1%.

An illustration of the magnitude of the shielding of  $^{235}\text{U}$  at lower energies in a natural uranium rod is given in Table 5.2. If mutual shielding above 183.6 eV is disregarded, we find for the total resonance integrals, using values from Table 5.3, that  $^{238}\text{U}$  is shielded by  $^{235}\text{U}$  to about 0.6% and  $^{235}\text{U}$  by  $^{238}\text{U}$  to about 7.5%. This is in reasonable agreement with values used by Askew (46) who indicates a general value of about 10% for the  $^{235}\text{U}$  shielding by  $^{238}\text{U}$ , and 1%  $^{238}\text{U}$  shielding per percent  $^{235}\text{U}$  present in uranium (enrichments up to 3%). It may be noted that these results confirm the significance of an integrated code such as RIFF RAFF for this category of isotope mixtures.

Table 5.2. Partial resonance integrals between 0.55 eV and 183.6 eV for a 8 mm diameter, 90 mm length, natural uranium cylinder

$^{238}\text{U}$	"infinite dilution"	272.3	b
$^{238}\text{U}$	shielded by $^{238}\text{U}$	12.932	b
$^{238}\text{U}$	shielded by $^{235}\text{U}$ and $^{238}\text{U}$	12.836	b
$^{235}\text{U}$	"infinite dilution"	2.614	b/ $^{238}\text{U}$ -at.
$^{235}\text{U}$	shielded by $^{235}\text{U}$	2.535	b/ $^{238}\text{U}$ -at.
$^{235}\text{U}$	shielded by $^{238}\text{U}$ and $^{235}\text{U}$	2.326	b/ $^{238}\text{U}$ -at.

### 5.2.2. Input data

A lower cut-off of 0.55 eV was used for the resonance integrals (17). For the resonance parameters of  $^{238}\text{U}$ , the "recommended" set of Schmidt (47) was chosen. The contribution to the resonance integral of neutrons with energies between 0.55 eV and 3.5 eV was again exclusively computed with RIFF RAFF', in view of the limitations of ERIDEL for low energies (sect. 4.3); this contribution varied from 0.98 b to 0.94 b for the rods under consideration. Furthermore for high-energy contributions and p-wave resonances respectively 0.85 b and 0.83 b were added to the  $^{238}\text{U}$  resonance integral, as proposed by Foell and Connolly (48). The unresolved parameters used are (only s-wave)

$$\begin{aligned} \bar{I} &= 0, \quad l = 0, \quad J = \frac{1}{2}, \\ \bar{D} &= 35.4 \text{ eV}, \\ \text{SF} &= 9.10^{-5} \text{ eV}^{-\frac{1}{2}}, \\ \bar{\Gamma}_{\gamma} &= 0.025 \text{ eV}. \end{aligned}$$

For  $^{235}\text{U}$  the numerical cross-section values were taken from Schmidt (47).

For the thorium computations we used a parameter set which was very similar to the recommended values of BNL-325 (7). The bound-level parameters of Tirèn (49) were added, whilst for unknown gamma widths a value of 24.5 meV was assumed (50). An extra  $\frac{1}{v}$  cross-section of 0.91 b was necessary to reach the adopted absorption cross-section value of 7.56 b for 2200 m/s neutrons. This was attributed to distant bound levels. The low-energy region, where no ERIDEL computations

were made, extended for thorium from 0.55 eV to 16.7 eV. For p-wave and high-energy contributions Sehgal's values (51) were used. The  $^{232}\text{Th}$  unresolved parameters selected are (only s-wave)

$$\begin{aligned} \bar{I} &= 0, \quad l = 0, \quad J = \frac{1}{2}, \\ \bar{D} &= 35.2 \text{ eV}, \\ \text{SF} &= 7.10^{-5} \text{ eV}^{-\frac{1}{2}}, \\ \bar{\Gamma}_{\gamma} &= 0.0245 \text{ eV}. \end{aligned}$$

### 5.2.3. Room-temperature resonance integrals

For the computations the rods are considered to be infinitely long, with a mean chord length  $\bar{l}$  conforming to that of the real ones. This means that a fictive diameter  $d'$  is determined from

$$\bar{l} = d' = \frac{4V}{S} = \frac{4\pi r^2 l}{2\pi r^2 + 2\pi r l} = \frac{2rl}{r + l} \quad (5.1)$$

Our computed resonance integrals for pure  $^{238}\text{U}$  are given in Fig. 5.1, with error margins as follow from sect. 5.3.1.

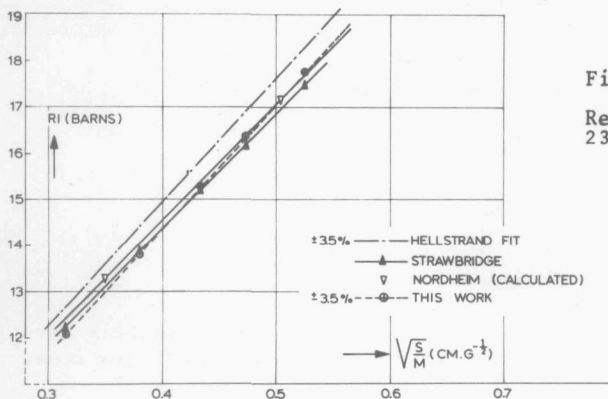


Fig. 5.1.  
Resonance integrals for  $^{238}\text{U}$ ,  $\frac{1}{v}$ -part included

A reasonable agreement is found with the "best fit to measurements" of Hellstrand<sup>1</sup>(72), Strawbridge's approximation formula (52) and calculations of Nordheim (53). In Fig. 5.2

<sup>1</sup>It is emphasised that this is a fit to a number of reported experimental results, and differs from Hellstrand's own measurements (8); the latter coincide in fact better with our computations.

for  $^{232}\text{Th}$  a good agreement is shown between the "fit to measurements" of Hellstrand (12) and Sehgal's computations

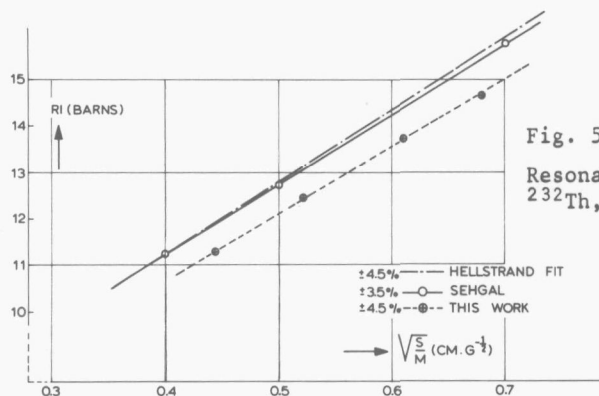


Fig. 5.2.

Resonance integrals for  $^{232}\text{Th}$ ,  $\frac{1}{v}$ -part included

(57). Our results, though having the same trend, are generally about 0.6 barn lower. This is probably due to the assumed mean  $\bar{\Gamma}$  value, as this parameter is subject to a possible error  $\gamma$  of circa 10% (53). A better agreement would be reached for  $\bar{\Gamma} = 0.027$  eV (Sehgal:  $\bar{\Gamma} = 0.0259$  eV), although for the  $\gamma$  low mean gamma width  $\gamma$  the error margins overlap too.

Values for  $^{238}\text{UO}_2$  are graphically represented in Fig. 5.3, showing a good agreement with other data.

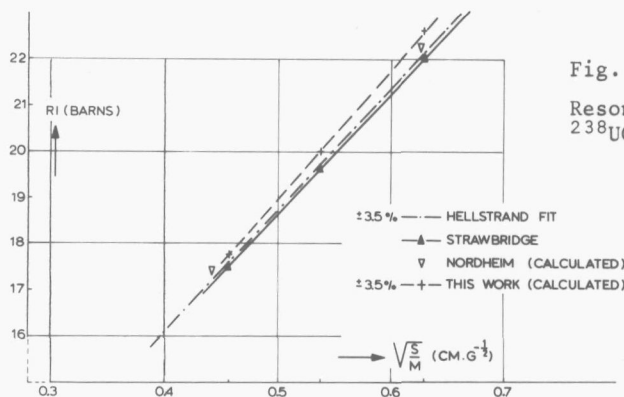


Fig. 5.3.

Resonance integrals for  $^{238}\text{UO}_2$ ,  $\frac{1}{v}$ -part included

For natural uranium metal rods the results are given in Table 5.3.

Table 5.3. Resonance absorption integrals for natural uranium rods

rod	RI 0.55 eV - 2 MeV (barns)		
	<sup>235</sup> U	<sup>238</sup> U	total
U8	2.795	17.773	20.57
U10	2.755	16.336	19.09
U12	2.721	15.291	18.01
U16	2.660	13.825	16.49
U24	2.563	13.094	15.66
UO <sub>2</sub> 10	3.301	22.592	25.89
UO <sub>2</sub> 14	3.263	19.995	23.26
UO <sub>2</sub> 20	3.191	17.777	20.97

These results indicate that the total absorption resonance integral for metal rods can be approximated by

$$RI = 5.8 + 28.1\sqrt{\frac{S}{M}} \text{ barns } \pm 5\% \quad , \quad (5.2)$$

for  $0.3 < \sqrt{\frac{S}{M}} < 0.55$ .

It should be noted that this formula includes the  $1/v$ -absorption, whilst mutual shielding is accounted for.

The computed resonance integrals for three natural uranium-dioxide rods are also presented in Table 5.3. The matching formula in this case is

$$RI = 7.9 + 28.6\sqrt{\frac{S}{M}} \text{ barns } \pm 5\% \quad , \quad (5.3)$$

For a discussion of the error margins, the reader is again referred to sect. 5.3.1.

#### 5.2.4. Doppler coefficients

The resonance integrals are computed for two temperatures, 293 K and 793 K. Doppler coefficients  $\beta_+$  are deduced from the results, assuming the validity of the common empirical formula for the temperature dependence of resonance absorption, which reads (53)

$$RI(T_1) = RI(T_0) \{1 + \beta_+(\sqrt{T_1} - \sqrt{T_0})\} \quad (5.4)$$

Generally the, non-temperature dependent,  $1/v$ -contribution is included, as indicated by the subscript + to  $\beta_+$ . This procedure is preferred, as often no clear  $1/v$ -part of a cross-section can be distinguished; therefore it seems to be somewhat far-fetched to maintain a separation. In Figs. 5.4 and 5.5 our computed (RIFF RAFF') resonance integrals of a natural uranium and a thorium rod are shown for four temperatures. A slight curvature, giving rise to smaller  $\beta_+$

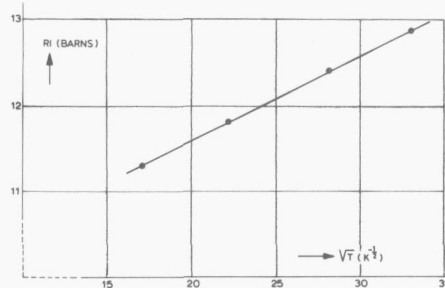


Fig. 5.4.

Computed temperature dependence of the resonance integral of U16 (RIFF RAFF')

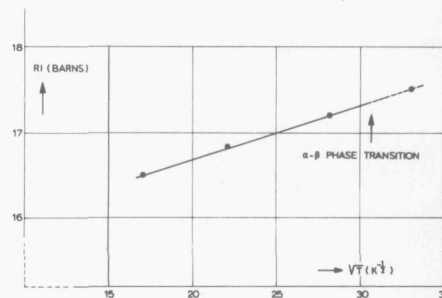


Fig. 5.5.

Computed temperature dependence of the resonance integral of Th20 (RIFF RAFF')

values at higher temperatures, may be noticed for the computed points in the graphs. However, a linear approximation of RI as a function of  $\sqrt{T}$  seems suitable for the rods and temperatures under consideration, which confirms the use of formula 5.4. Other rods and materials, as well as the use of the ERIDEL-code, gave similar results.

From activation experiments, several values for the Doppler coefficient of  $^{238}\text{U}$  in natural uranium are known. In Fig. 5.6 our computations are compared with experimental data from

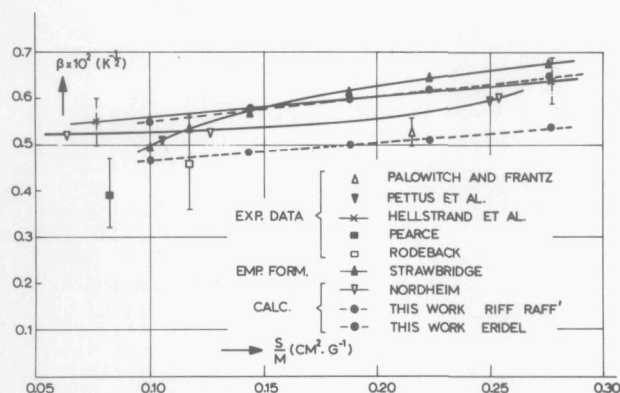


Fig. 5.6.  
Doppler  
coefficients  
for  $^{238}\text{U}$

Palowitch and Frantz (54), Pettus et al. (55), Hellstrand et al. (56), Pearce (57) and Rodeback (58), plus Nordheim's ZUT-TUZ computations (53), and Strawbridge's empirical formula (52). It should be noted that in this graph values of  $\beta$  are plotted which do not include  $1/v$ -absorption, as is customary for  $^{238}\text{U}$ . Use of the ERIDEL code over most of the energy region leads, as might have been expected (sect. 4.3.2.1), to higher values than the combination of ERIDEL and RIFF RAFF' does. From Fig. 5.6 it will be obvious that there is no preference for either of the computation methods.

Five thorium rods, with diameters ranging from 8 to 24 mm, were considered, the results being plotted in Fig. 5.7. Only two experimental points seem to be available for comparison (Pearce (57) and Rodeback (58)). Earlier computations by Nordheim and Kuncir (28) were corrected assuming a low-temperature value of the resonance integral in agreement with more up-to-date results of Sehgal (57). The computed temperature dependences were then converted into  $\beta_+$  values. The RIFF RAFF' and ERIDEL curves are less than 10% apart, which is probably due to the fact that  $^{232}\text{Th}$  has no pronounced resonances below 20 eV.

The situation is more complicated for natural uranium, as no Doppler-broadening procedure for numerical  $^{235}\text{U}$  cross-sections

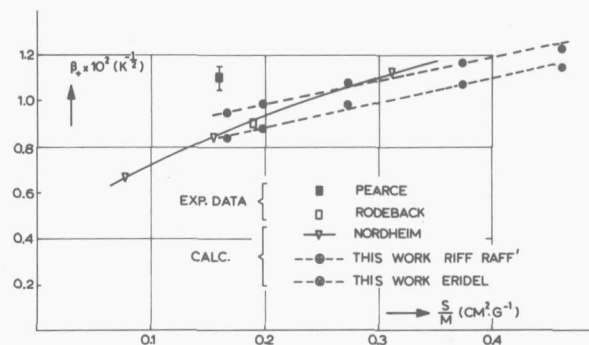


Fig. 5.7.  
Doppler  
coefficients  
for  $^{232}\text{Th}$

was included in RIFF RAFF'<sup>1</sup>. This is in fact not necessary for slightly enriched uranium, as will be demonstrated by the following estimate.

Although the  $^{235}\text{U}$  resonance peaks can be described only roughly with one-level Breit-Wigner contours, a number of parameter sets has been published. For an indicative computation concerning  $^{235}\text{U}$  we use again the "recommended" Schmidt parameter values (47). It is necessary to complete this set with one or two negative or "bound" resonance energy levels. As sufficient information about the parameters of these levels could not be obtained, we determined them ourselves. A least squares method was used, requiring a complete resonance parameter set to describe as accurately as possible the known  $^{235}\text{U}$  cross-sections at a number of energies between 1 eV and 10 eV. The bound level parameters which were found are quoted in Table 5.4.

Table 5.4. Bound-resonance parameters of  $^{235}\text{U}$

$E_R$ (eV)	$g$	$\Gamma_n$ (eV)	$\Gamma_\gamma$ (eV)	$\Gamma_f$ (eV)
- 2.05	0.5	0.0041	0.020	0.26
- 0.16	0.5	0.00002	0.044	0.24

With the complete parameter set, some computations were carried out on the partial resonance integrals between 0.4 eV and 37.1 eV of the natural uranium metal U8 cylinder (Table 5.5). For natural uranium, possible temperature effects in the  $^{235}\text{U}$  isotope will be most pronounced in this low-energy region, where a substantial

<sup>1</sup>A suitable procedure for the computation of Doppler broadening in numerical cross-section data may be found in (59).

**self-shielding effect exists.**

Table 5.5. Partial  $^{235}\text{U}$  resonance absorption integrals for the natural uranium metal rod U8

calculation data	RI 0.4 eV - 37.1 eV (barns)
U8, T = 293 K, res. parameters	275.0
U8, T = 793 K, res. parameters	275.5
infinite dilution, num. cross-sect.	325
U8, T = 293 K, num. cross-sect., $^{238}\text{U} \sigma_a = \sigma_{rs} = 0$	313
U8, T = 293 K, num. cross-sect.	287

From the first and the last line of Table 5.5 it can be seen that the partial resonance integral from parameter computation is about 4% lower than its numerical counterpart. This is not surprising in view of what was said earlier about the usability of the resonance contours (sect. 5.2.1). The last three results of Table 5.5 indicate that self-shielding in  $^{235}\text{U}$  is responsible for about one-third, and shielding by  $^{238}\text{U}$  for about two-thirds of the resonance integral decrease for  $^{235}\text{U}$  in the above-mentioned case.

An interesting conclusion is that according to the computations in this natural uranium rod, for a  $\frac{1}{E}$ -neutron spectrum, hardly any temperature dependence exists in the  $^{235}\text{U}$  absorption. The Doppler effect in  $^{235}\text{U}$ , which would already be small at this large dilution, is apparently partly compensated for by a temperature-dependent increase in the shielding by  $^{238}\text{U}$ . This might be different for other  $^{235}\text{U}$ -enrichments or other neutron spectra.

For the natural uranium rods which we considered (U6 to U24) the total resonance absorption integral for  $^{235}\text{U}$  varied only slightly (400 to 360 barns). This justifies the conclusion that for all of these rods the Doppler effect in  $^{235}\text{U}$  will be of minor importance. For the  $^{235}\text{U}$  absorption at higher temperatures we therefore introduced values identical to those computed for room temperature.

In Fig. 5.8 our results for the Doppler coefficient of natural uranium metal are presented. The curves can be described by

$$\beta_+ = \left(0.36 + 0.50 \frac{S}{M}\right) 10^{-2} \text{K}^{-\frac{1}{2}} \pm 15\% \quad (5.5)$$

Other computed results according to the Doppler effect in the neutron absorption of natural uranium are scarce, and experimental data mostly concern related quantities only. Activation experiments, for example, generally give information about the  $^{238}\text{U}$  effect only, simply because the  $^{238}\text{U}$  activation is being determined. In reactivity experiments, as made with global oscillators, the  $^{235}\text{U}$  in the natural uranium not only absorbs, but also produces neutrons. This is also true for the local pile oscillator, but here the "worth" of a fast fission neutron is practically zero. For a global oscillator the worth of a fast neutron resulting from fission in the sample is only slightly smaller than that of a low-energy neutron. This means that such a reactivity measurement contains no direct information according to the pure neutron absorption in the sample.

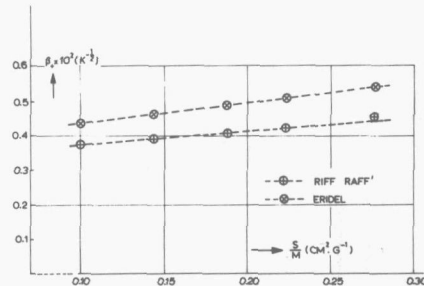


Fig. 5.8.

Doppler coefficients of natural uranium metal

The results of the computations on natural uraniumdioxide can be seen in Figs. 5.9 and 5.10. In the first graph our values

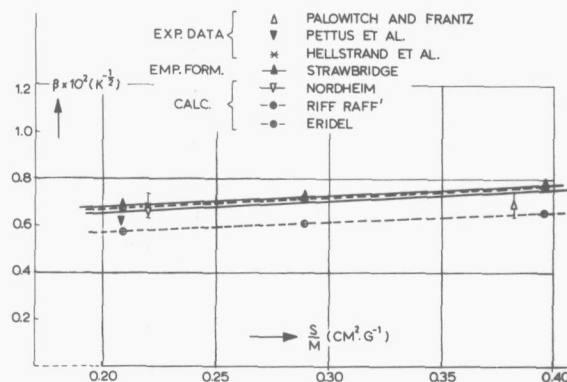
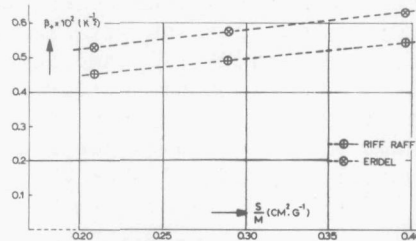


Fig. 5.9.

Doppler coefficients of  $^{238}\text{UO}_2$

Fig. 5.10.

Doppler coefficients of natural uraniumdioxide



for the Doppler coefficient of the  $^{238}\text{U}$  in this material (not including  $1/v$ ), are compared with those of Palowitch and Frantz (54), Pettus et al. (55), Hellstrand et al. (56), Strawbridge (52) and Nordheim (53). In Fig. 5.10 results for the  $\beta_+$  of the complete rod are presented. It is worth noting that  $\beta_+$  for a same S/M-ratio the Doppler coefficients of  $\text{UO}_2$  are slightly higher than those of the pure metal. The curves for  $\text{UO}_2$  can be approximated by

$$\beta_+ = (0.38 + 0.53 \frac{S}{M}) 10^{-2} \text{K}^{-\frac{1}{2}} \pm 15\% \quad (5.7)$$

### 5.3. Error margins

The uncertainties in the computed resonance integrals and Doppler coefficients have three sources

1. inadequacy of the Breit-Wigner one-level concept;
2. imperfections in the computer codes;
3. errors in the resonance parameter sets or numerical cross-section data.

Primarily for the discussion on points 2 and 3, we shall consider the computations on cold resonance integrals and Doppler coefficients separately.

#### 5.3.1. Resonance integrals at room temperature

As to the first error source, it is commonly accepted that the one-level concept is sufficient for materials with well separated resonances, as  $^{232}\text{Th}$  and  $^{238}\text{U}$  (53). Furthermore for  $^{235}\text{U}$  we used numerical cross-section values, which are not dependent on any model. Therefore we may consider errors due to point 1 to be relatively small.

Imperfections in computer codes, the second error source, can be studied by comparison with Monte Carlo results. This has been done by Levine (60) and Lewis (43), for moderated absorber rods. It becomes clear from their work that for low values of S/M flat-flux type computations will give excessively high values for the resonance integrals. A 1% error arises for U-metal and for UO<sub>2</sub> when  $\sqrt{S/M} \approx 0.3 \text{ cm g}^{-\frac{1}{2}}$ , resp.  $\approx 0.45 \text{ cm g}^{-\frac{1}{2}}$ . For higher values of  $\sqrt{S/M}$  the difference is smaller, probably due to cancellation of errors, as discussed in sect. 4.3.2.2. For thorium no direct comparison was found, but the same tendency may be expected.

Unfortunately, no Monte Carlo results could be detected for unreflected rods. As discussed in sect. 4.3.2.2 it is supposed that with bare rods the RIFF RAFF' cold resonance integrals might be too high. An indication of the order of magnitude involved is given by the percentage by which the cold RI's would have to be decreased in order to produce optimal agreement between computed and measured Doppler coefficients or, if measurements have not been carried out, to bring RIFF RAFF' and ERIDEL in agreement in this respect. This percentage is at most 1% for <sup>238</sup>U, and even less for the other absorbers.

Taking into account the magnitude of these phenomena and considering the good agreements for reflected rods, it was decided to arbitrarily include an error margin of 1.5% for <sup>238</sup>U and 1% for the other absorbers, to account for imperfections in the codes.

The individual resonance parameters build the third source of errors. The parameters quoted in literature show appreciable error margins, which may be as high as 10% to 20% for important low-energy resonances. This has a strong influence on single-peak resonance integrals as can be seen from Table 5.6. Here a number of results are given for four specific resonances in an infinitely long <sup>238</sup>U cylinder, radius 0.422 cm.

Table 5.6 may in part be compared with Table 12 in (28), where results of the ZUT-code are given. Noteworthy are the low ERIDEL resonance integrals for the 6.68 eV resonance (approximations discussed in sect 4.3) and for the 103 eV resonance (disregard of scattering interference), as well as the large differences in  $\Delta$ -values for these energies. The increase of the resonance integral depends in a rather complicated way on

the resonance properties, as can be seen for some cases in Table 5.6.

Before paying too much attention to details, however, it is useful to remember that for all resonance parameter sets a characteristic value (the infinite dilution resonance integral  $RI_{\infty}$ ) exists, to which a specific error region may be attributed. An appreciable amount of experimental investigation has been carried out to determine these  $RI_{\infty}$ 's.

Table 5.6. The influence of a 10% change in resonance parameters on the single-peak resonance integrals for  $^{238}\text{U}$  at 300 K and at 800 K

		6.68 eV resonance RI (barns) 1 - 11 eV			
		$\Gamma_Y$ (eV)	0.024	0.0264	0.024
		$\Gamma_n$ (eV)	0.00148	0.00148	0.001628
RIFF RAFF'	RI(800)	5.152	5.394	5.398	
	RI(300)	5.070	5.316	5.320	
	$\Delta$	0.082	0.078	0.078	
ERIDEL	RI(800)	4.673	4.869	4.871	
	RI(300)	4.547	4.751	4.750	
	$\Delta$	0.126	0.118	0.121	
		81 eV resonance RI (barns) 65 - 87 eV			
		$\Gamma_Y$ (eV)	0.024	0.0264	0.024
		$\Gamma_n$ (eV)	0.0021	0.0021	0.00231
RIFF RAFF'	RI(800)	0.338	0.342	0.346	
	RI(300)	0.259	0.264	0.266	
	$\Delta$	0.079	0.078	0.080	
ERIDEL	RI(800)	0.329	0.333	0.338	
	RI(300)	0.252	0.256	0.258	
	$\Delta$	0.077	0.077	0.080	

103 eV resonance RI (barns) 80 - 110 eV				
	$\Gamma_{\gamma}$ (eV)	0.024	0.0264	0.024
	$\Gamma_n$ (eV)	0.072	0.072	0.0792
RIFF RAFF'	RI(800)	0.510	0.544	0.523
	RI(300)	0.491	0.525	0.504
	$\Delta$	0.019	0.019	0.019
ERIDEL	RI(800)	0.466	0.497	0.481
	RI(300)	0.436	0.465	0.452
	$\Delta$	0.030	0.032	0.029
475 eV resonance RI (barns) 450 - 482 eV				
	$\Gamma_{\gamma}$ (eV)	0.024	0.0264	0.024
	$\Gamma_n$ (eV)	0.005	0.005	0.0055
RIFF RAFF'	RI(800)	0.0519	0.0528	0.0545
	RI(300)	0.0438	0.0446	0.0455
	$\Delta$	0.0081	0.0082	0.0090
ERIDEL	RI(800)	0.0487	0.0498	0.0513
	RI(300)	0.0408	0.0419	0.0427
	$\Delta$	0.0079	0.0079	0.0086

It is usual to compose parameter sets and contributions to  $RI_{\infty}$  from the unresolved region, "high energy", etc. so that they predict correctly the  $RI_{\infty}$ . Now in fact the determination of effective resonance integrals ( $RI_{eff}$ ) involves nothing more than multiplying the  $RI_{\infty}$  by a certain self-shielding factor, so we might suppose that the relative error in  $RI_{eff}$  is the same as that in  $RI_{\infty}$ . This argument is not completely correct, as the "weight" of specific resonances with their specific error margins is not the same in  $RI_{\infty}$  and  $RI_{eff}$ . For an approximate error estimation, however, it is acceptable as long as the "weight" shift is not extreme, which is the case in our computations. From literature

sources we find values for  $RI_{\infty}$  of the isotopes (Table 5.7).

Table 5.7. Infinite dilution resonance integrals

material	lit. values $RI_{\infty}$ (barns)	our $RI_{\infty}$	estimated error margin
$^{238}\text{U}$	$278.2 \pm 10$ (67), $283.2 \pm 8$ (66)	276	3.5%
$^{235}\text{U}$	$402 \pm 29$ (63), $432 \pm 29$ (64)	440	7%
$^{232}\text{Th}$	$82.5 \pm 3$ (62), $86 \pm 6$ (65)	82	6%

Now for the cold resonance integrals we arrive at the following error estimates:

$$\begin{array}{ll}
 ^{238}\text{U}, \text{ } ^{238}\text{UO}_2: & 1 + 3.5 & = 4.5\% \\
 \text{U}, \text{ } \text{UO}_2: & 1 + 0.8 \times 3.5 + 0.2 \times 7 & = 5\% \\
 \text{Th} & : 1 + 6 & = 7\%
 \end{array}$$

### 5.3.2. Doppler coefficients

A variation in resonance parameters may have a considerable influence on the Doppler coefficient for individual resonances (Table 5.6). However, since the  $RI_{\infty}$  of a specific absorber is a constant, the Doppler effect changes will partly cancel each other out. Furthermore much depends on the adequacy of the codes and this is sometimes questionable (sect. 4.3). Monte Carlo computations in this field can certainly be quite valuable. As long as these are not at our disposal in sufficient quantity, an error estimation on the computed Doppler coefficients will be difficult. An indication of what the errors could be follows from comparison between results from different codes and experimental values (sect. 5.2, Chapter 6). An error margin of about 15% is required to create agreement between the majority of results.

### 5.3.3. The influence of a non-zero Debye temperature

When deriving the formula for the Doppler-broadened cross-sections (sect. 4.1) the assumption is made that the absorber atoms have a Maxwellian distribution of velocities. This assumption will be valid if the absorber nuclei are in the

gaseous state, but for liquids or solids it is only a rough approximation. A somewhat more sophisticated model is that of Debye, which is discussed by Dresner (6). We will not consider this matter in detail, but will content ourselves with the fact that after introduction of the Debye model all formulas remain unchanged, except that the thermodynamic temperature  $T$  has to be replaced by

$$T^{\times} = \frac{3}{2} \theta_D \int_0^1 x^3 \coth(x\theta_D/2T) dx, \quad (5.8)$$

where  $\theta_D$  is the Debye temperature. Fig. 5.11 elucidates this formula.

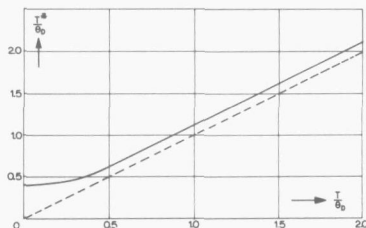


Fig. 5.11.

Relation between the thermodynamic temperature  $T$  and the "effective" temperature  $T^{\times}$  in the Debye model ( $\theta_D$ =Debye temperature) (67)

The qualitative conclusions that can be drawn from Fig. 5.11 are that for  $T > 0.4 \theta_D$ ,  $T^{\times}$  will be about  $0.15 \theta_D$  greater than  $T$ , resulting in an increase in the cold resonance integrals, and that in certain cases the thermodynamic temperature step will be higher than that in  $T^{\times}$ , resulting in a decrease in the Doppler effects. It is not easy to convert these qualitative considerations into quantitative numbers, because values for the Debye temperature  $\theta_D$  of the specific materials are not well known. It is generally accepted that for uranium and thorium  $\theta_D \ll 300$  K, the effect therefore being negligible at room temperature (Nordheim (53), however, mentions it as an explanation for certain deviations in experimental results for thorium). For a ceramic material such as  $UO_2$ , the estimations for  $\theta_D$  vary between 200 K and 600 K (67). In the latter, most unfavourable case our computed resonance integrals at room temperature would have been underestimated by about 1% and the Doppler effect for heating from 300 K to 873 K overestimated by roughly 7%. As long as no more specific data about Debye temperatures are at our disposal, we consider those

corrections as being "pro memoria"<sup>1</sup>.

<sup>1</sup>Schmidt evaluated a Debye temperature of 600 K for UO<sub>2</sub> (page D128, (47)). In the light of more recent experiments this value was reduced to 205 K (page D 62, same ref.).



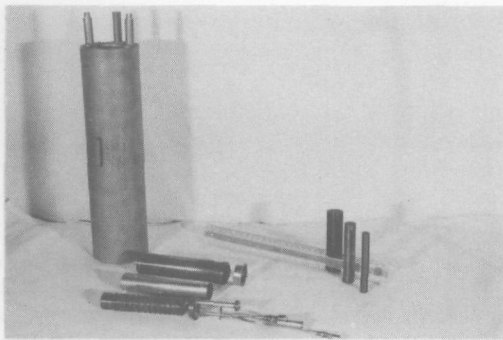


Fig. d.

Annular ionisation chamber,  
disassembled fuel furnace  
and three sample rods  
(length of ruler 30 cm)

## CHAPTER 6      COMPARISON BETWEEN COMPUTATION RESULTS AND LOCAL OSCILLATOR MEASUREMENTS

### 6.1. *Computation of chamber integrals and temperature coefficients*

There are two methods of comparing local pile oscillator measurements with computation results:

- a. for each material theoretical graphs are made, which convert measured chamber integrals and temperature effects into resonance integrals and Doppler coefficients (see Fig. 6.1).

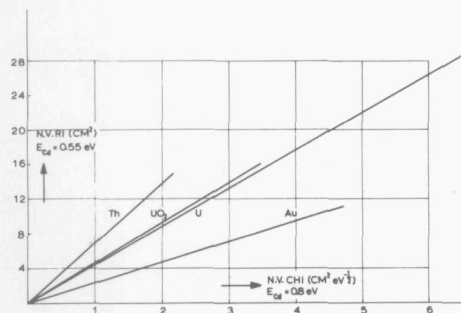


Fig. 6.1.

Macroscopic resonance integrals as functions of macroscopic chamber integrals for thorium, natural uranium dioxide, natural uranium and gold (computed results)

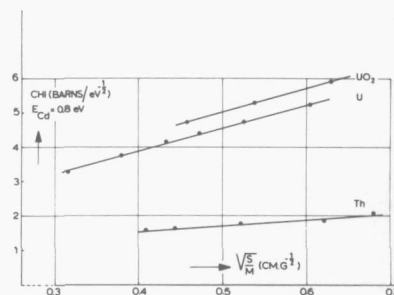
- b. for the rods to be measured the chamber results are computed directly and compared with experimental results.

We chose method b, which permits a more direct comparison, as was mentioned earlier (sect. 2.1.2). The computations were a simple variant on that which has been described in section 5.2. In ERIDEL the only difference was that the resonance integral for each specific resonance was divided by  $\sqrt{E_R}$ . In RIFF RAFF' the absorption rate in each small energy group was weighed with  $1/\sqrt{E}$ . Fig. 6.2 presents some computed results for the chamber integrals of a number of sample rods. The experimental check of these computations with oscillator measurements is reported in this Chapter (sect. 6.3, Figs. 6.3 and 6.4). From Fig. 6.2 it is clear that the empirical relation which generally holds for resonance integrals, viz.

$$RI = A + B \sqrt{\frac{S}{M}} \quad (6.1)$$

Fig. 6.2.

Chamber integrals for thorium, natural uraniumdioxide and natural uranium (computed results)



will also be valid, although with other coefficients, for chamber integrals. The relations which follow from Fig. 6.2 are quoted numerically in the next section.

For the Doppler coefficients the empirical relation was of the form

$$\beta = C + D \frac{S}{M} \quad (6.2)$$

or

$$\frac{RI(T) - RI(T_0)}{RI(T_0)(\sqrt{T} - \sqrt{T_0})} = C + D \frac{S}{M} .$$

It will be obvious from the computations of this quantity that such a relation is also useful for the "chamber Doppler coefficients". The results of these computations are graphically shown in Figs. 6.6, 6.9 and 6.11 for a direct comparison with experimental results (including thermal expansion).

It must be noted that a particular chamber integral can correspond to quite different resonance integrals, depending on which material is considered (Fig. 6.1). This is also true for the connection between "chamber Doppler effects" and Doppler coefficients. In general the relative temperature effect in the chamber integrals will be 20% to 50% lower than that in the resonance integrals, due to the domination of the lower-energy peaks which exhibit a lower temperature dependence (see also (53)).

### 6.2. Thermal expansion effect

In order to make a proper comparison between calculation and experiment it is necessary to account for the effect of thermal expansion in the samples. This can be done by using the empirical formula

$$CHI = A + B \sqrt{\frac{S}{M}} . \quad (6.3)$$

Since  $\frac{S}{M}$  increases at higher temperatures, a  $\Delta CHI$  can be computed which must be added to the temperature effect originated by the Doppler-broadening process. The following formulas (see also Fig. 6.2) and linear expansion coefficients have been used:

$$\begin{aligned} \text{natural uranium} \quad CHI &= 1.14 + 6.81 \sqrt{\frac{S}{M}} & (6.4) \\ \lambda &= 24 \times 10^{-6} / ^\circ\text{C} \end{aligned}$$

<sup>1</sup> Crystals of  $\alpha$ -uranium exhibit a very anisotropic thermal expansion: expansion coefficients in the three main directions are  $36.7 \times 10^{-6}$ ,  $-9.3 \times 10^{-6}$ , and  $34.2 \times 10^{-6}$  per  $^\circ\text{C}$ . This phenomenon causes a certain surface roughening at elevated temperatures in rods which like our samples consist of a mixture of crystals without a common orientation. This surface roughening may even become permanent after a prolonged period of thermal cycling, because the crystals have moved somewhat with respect to each other (19). It is difficult to determine which  $\lambda$  will properly describe the increase of  $\sqrt{\frac{S}{M}}$  as a function of temperature. Our choice is subject to an  $\frac{S}{M}$  uncertainty of at least 20%.

$$\text{thorium} \quad \text{CHI} = 0.82 + 1.78 \sqrt{\frac{S}{M}} \quad (6.5)$$

$$\lambda = 12 \times 10^{-6} / ^\circ\text{C} \quad (19)$$

$$\text{natural} \quad \text{CHI} = 1.60 + 6.85 \sqrt{\frac{S}{M}} \quad (6.6)$$

$$\text{uraniumdioxide} \quad \lambda = 11 \times 10^{-6} / ^\circ\text{C} \quad (19)$$

An impression of the non-negligible influence of the expansion effects on chamber integrals is given in section 6.4. The effect is computed for each rod and added to the computed chamber Doppler effect. This was done because the expansion effect is always interwoven with the Doppler effect and has a similar influence on the reactivity.

At this point it may be worthwhile to emphasise the fact that for relations of the type (6.1) and (6.2) no direct physical argumentation can be given. These are just empirical relations which describe the resonance absorption phenomena quite accurately at certain intervals; they are therefore extremely useful.

### 6.3. Room temperature chamber integrals

Cold chamber integrals have been measured of a number of materials such as uranium metal and oxide, thorium, gold-lead mixtures, boron-lead mixtures, titanium, etc. There was no really significant deviation from a linear relationship between the oscillator result normalised on reactor power O/P and the computed volume integrated chamber integrals (Figs. 6.3 and 6.4). From a specific oscillator result, the experimental volume integrated chamber integral of the sample can be found with the calibration line in Figs. 6.3 and 6.4. The calibration line in these graphs is the best fit for a number of measurements on Pb-Au rods. The O/P values of these cylinders are represented at the N.V. CHI-values which belong to the N.V. RI-value (Fig. 6.1), that was determined by activation measurements (Chapter 3). This calibration line for oven measurements is therefore comparable to the calibration line in Fig. 3.2 which was used for work with two samples. The bigger the absorber, the better the reproducibility of the oscillator result, varying from  $\pm 2\%$  for N.V.  $\text{CHI} > 4 \text{ cm}^2 \text{ eV}^{-\frac{1}{2}}$  to  $\pm 10\%$  for N.V.  $\text{CHI} \sim 1 \text{ cm}^2 \text{ eV}^{-\frac{1}{2}}$ . This reproducibility margin is indicated in the graphs, which means that possible systematic errors (gold calibration,  $\frac{1}{E}$ -spectrum deviations) are not taken into consideration in this margin.

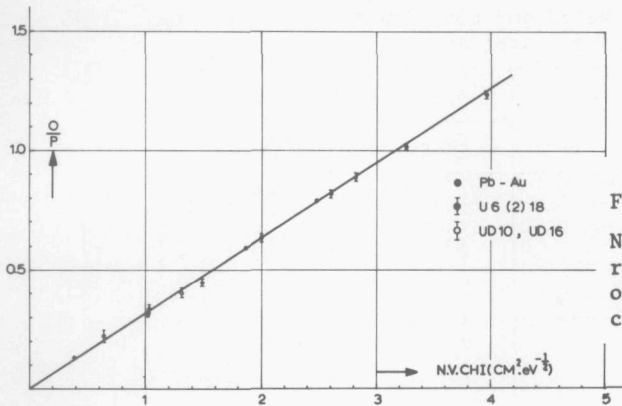


Fig. 6.3.

Normalised oscillator results as a function of computed macroscopic chamber integrals

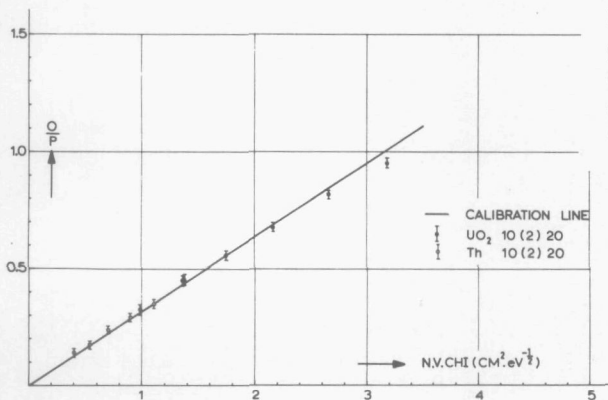


Fig. 6.4.

Normalised oscillator results as a function of computed macroscopic chamber integrals

Measured and computed chamber integrals are compared for a number of characteristic rods in Table 6.1. It may be mentioned that whilst uranium and thorium were used in the form of massive rods, the uraniumdioxide samples were composed of 15 to 20 mm thick pellets.

From Table 6.1, two important conclusions may be drawn:

1. the combination of resonance absorption codes predicts adequately the experimental results on chamber integrals.

Table 6.1. Measured and computed volume integrated chamber integrals

rod identification	N.V.CHI ( $\text{cm}^2 \text{eV}^{-\frac{1}{2}}$ )	
	computed	measured
U8	1.03±5%	1.07(±8%)
U10	1.48 -	1.42
U12	2.01 -	2.00
U16	3.24 -	3.21(±3%)
UD10	1.31 -	1.29
UD16	2.82 -	2.81
Th10	0.40±7%	0.44(±10%)
Th14	0.71 -	0.75
Th20	1.37 -	1.39(±6%)
UO <sub>2</sub> 10	1.00±5%	1.03±8%
UO <sub>2</sub> 14	1.75 -	1.75
UO <sub>2</sub> 20	3.19 -	3.00±3%

2. the linearity of the relation between O/P and N.V. CHI, already predicted by the Pb-Au measurements, is confirmed.

#### 6.4. Temperature dependence

The temperature dependence of the resonance absorption has been measured by heating each sample to about 600°C (873 K). Both, room temperature and high temperature are maintained for about 30 minutes. Heating and cooling require about 5 minutes. Three to six cycles are completed whilst the mean jump in the absorption is considered as the final result. Fig. 6.5 illustrates this procedure. Furthermore for UO<sub>2</sub>10 and Th10 the chamber integrals are determined step by step at 300, 490, 680, 870 and 1060 K, to verify the applicability of a constant  $\beta$ -factor (Eq. 6.2). This has not been done for U-metal, firstly because the maximum heating temperature is limited by the first phase transition (941 K), and secondly since the relatively small Doppler effect prevents accurate measuring over small temperature steps.

##### 6.4.1. Natural uranium

Fig. 6.6 records the measured absorption increase in eight

Fig. 6.5.  
Measuring record for U16

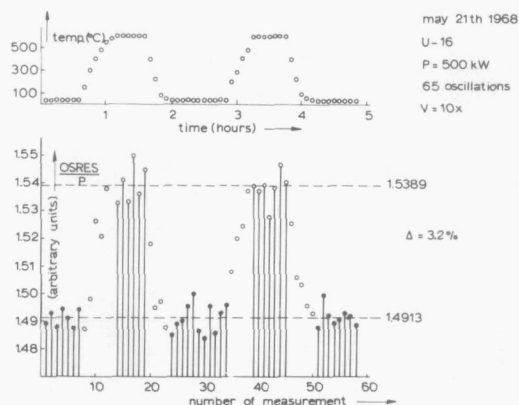


Table 6.2. Temperature effects in uranium metal

rod identification	chamber integral increase (%), 300-873 K			
	theoretical			experimental
	expansion	total		
		RIFF RAFF <sup>1</sup>	ERIDEL	
U6	1.08	4.07	5.62	5.07
U8	1.04	3.49	4.81	4.23
U10	1.01	3.15	4.25	3.98
U12	0.99	2.91	3.83	3.54
U14	0.96	2.71	3.57	3.30
U16	0.95	2.59	3.32	2.98
U18	0.93	2.50	3.20	2.88
U20	0.92	2.41	3.08	2.68
UD10	1.11	3.48	4.84	4.35
UD16	1.05	2.89	3.70	3.25

natural uranium rods, together with calculated results. In Table 6.2 numerical values are given; two other rods are included which were depleted to a 0.21%  $^{235}\text{U}$  content. The large discrepancy between the two codes is caused almost completely by the first three resonance peaks, which phenomenon makes the difference more pronounced than would

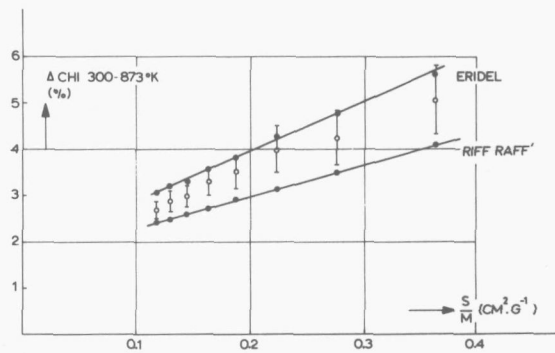


Fig. 6.6. Temperature effects in uranium metal

be the case for resonance integral computations (sect. 4.3.2).

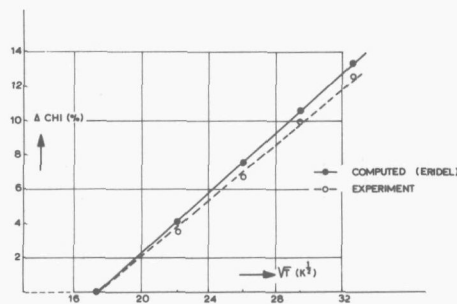


Fig. 6.7.  
Temperature dependence of the  
chamber integral of Th10

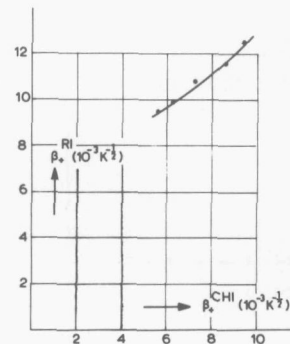


Fig. 6.8.  
Doppler coefficient as a  
function of chamber Doppler  
coefficient for  $^{232}\text{Th}$   
(computed results)

#### 6.4.2. Thorium

Fig. 6.7 shows the chamber integral increase in four steps for Th10 (expansion effect subtracted), as a function of  $\sqrt{T}$ . The curve can be approximated by

$$\text{CHI}(T) = \text{CHI}(T_0) \{1 + 0.0081 (\sqrt{T} - \sqrt{T_0})\} . \quad (6.7)$$

The factor 0.0081 is called the "chamber Doppler coefficient",

$\beta_+^{\text{CHI}}$ . We may conclude from Fig. 6.7 that an empirical relation of this kind is useful for the measurements concerned. The quantity  $\beta_+^{\text{CHI}}$  is comparable to the common Doppler coefficient  $\beta_+$  (sect. 5.2.4). In Fig. 6.8 computed results (ERIDEL) for the relation between  $\beta_+^{\text{CHI}}$  and  $\beta_+$  are plotted. It is possible to determine  $\beta_+^{\text{CHI}}$  experimentally, and to find  $\beta_+$  with the aid of Fig. 6.8, which could then be compared again to other experimental or theoretical values (Fig. 5.7). We will not consider this procedure even though it would not lead to controversial results for our measurements, firstly because the weight of high-energy absorption is too low in the chamber results, and secondly because the use of Fig. 6.8 would introduce an appreciable influence of the computations on the "experimental"  $\beta_+$ . Therefore we will restrict ourselves to comparing theoretical and experimental chamber results.

Table 6.3 lists further thorium results which are represented in Fig. 6.9. The results obtained with the two code combinations differ appreciably less than for uranium, which is partly a consequence of the fact that thorium has no resonances below 20 eV. A preference for one of the codes cannot be made.

Table 6.3. Temperature effects in thorium

rod identification	chamber integral increase (%), 300-873 K		$\beta_+^{\text{CHI}} (\text{K}^{-1/2})$		
	theoretical		experimental		
	expansion	total			
		RIFF RAFF'	ERIDEL		
Th10	0.40	9.8	10.9	11.1	$0.87 \cdot 10^{-2}$
Th12	0.38	8.9	9.9	10.8	$0.84 \cdot 10^{-2}$
Th14	0.37	8.3	9.3	8.5	$0.66 \cdot 10^{-2}$
Th16	0.36	7.5	8.7	8.0	$0.62 \cdot 10^{-2}$
Th18	0.35	6.9	8.2	7.5	$0.58 \cdot 10^{-2}$
Th20	0.34	6.5	7.9	6.8	$0.53 \cdot 10^{-2}$

#### 6.4.3. Uraniumdioxide

The usability of a formula of the type (6.7) for  $\text{UO}_2$  can be judged from Fig. 6.10. Although the  $\sqrt{T}$ -approximation is satisfactory, a certain curvature in the "experiment" graph may be noticed, which might be attributed to crystal binding

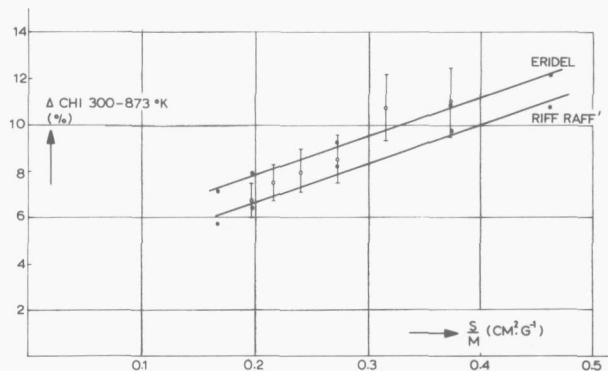


Fig. 6.9. Temperature effects in thorium metal

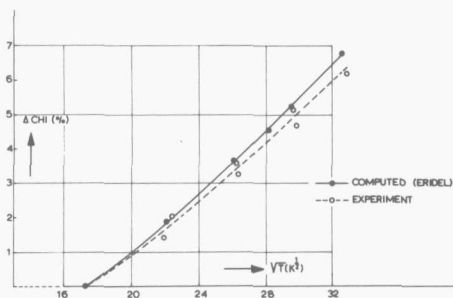


Fig. 6.10.

Temperature dependence of  
the chamber integral of  $UO_2$

effects as discussed in sect. 5.3.3. These may be accounted for in the computations by replacing the real temperatures by slightly higher fictitious ones (Fig. 5.11). However, in the uncorrected computations a similar curvature appears already. This points to the fact that the curvature observed in the measurements is not a direct consequence of the non-zero Debye temperature of  $UO_2$ , but is rather caused by the fact that a formula like (6.7) can not describe the phenomena perfectly in this case. This is not surprising, as this formula is an empirical one, not based on theoretical considerations.

In Table 6.4 other results are given for  $UO_2$ . From Fig. 6.11 it can be seen that although there is still a noticeable discrepancy, ERIDEL and RIFF RAFF' results agree somewhat

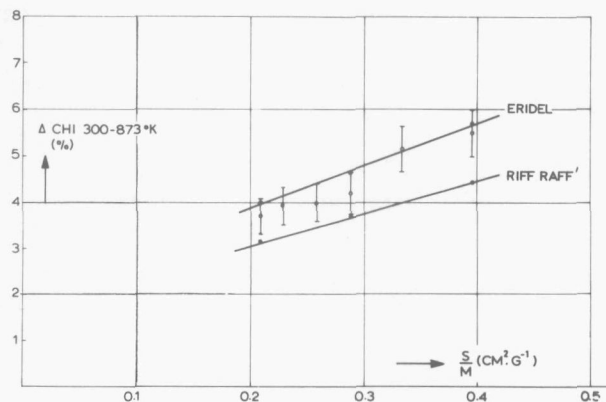


Fig. 6.11. Temperature effects in  $UO_2$

Table 6.4. Temperature effects in  $UO_2$

rod identification	chamber integral increase (%), 300-873 K			
	theoretical			experimental
	expansion	total		
		RIFF RAFF'	ERIDEL	
$UO_2$ 10	0.47	4.44	5.69	5.51
$UO_2$ 12	0.46	4.00	5.10	5.14
$UO_2$ 14	0.45	3.69	4.66	4.21
$UO_2$ 16	0.44	3.45	4.40	3.98
$UO_2$ 18	0.43	3.25	4.15	3.92
$UO_2$ 20	0.42	3.11	3.97	3.69

better than in the case of uranium metal. This must be a result of the smoothening effects of oxide scattering and the dilution of the uranium atoms, which make the flux dips relatively less deep.

#### 6.5. Some controls

A number of checks has been carried out, in order to verify whether any systematic error might influence the results.

### 6.5.1. Leakage as a yardstick for absorption

The absorption of neutrons is determined in the computations. Experimentally however, the change in leakage of neutrons from the sample region is decisive. Whether the latter is really representative of the neutron absorption, can be verified with the code RIFF RAFF'. A balance equation is drawn up for the leakage from the region where a sample is present:

leakage change = undisturbed leakage - leakage when sample is present

$$\text{Hence } \Delta L = S_s - (S_s \cdot P_s + \sum_{i=0}^2 B_i \cdot S_i \cdot P_{oi}), \quad (6.8)$$

where  $S_s$  = number of neutrons impinging on the surface of the rods ( $s^{-1}$ ),  
 $P_s$  = direct escape probability for neutrons impinging on the rod,  
 $B_i = \frac{\pi r^2}{i+1}$  ( $cm^2$ ),  
 $S_i$  = source of neutrons in  $i_{th}$  mode ( $cm^{-2}s^{-1}$ ),  
 $P_{oi}$  = first flight escape probability for neutrons in  $i_{th}$  mode.

$$\text{Or } \Delta L = S_s(1-P_s) - \sum_{i=0}^2 B_i \cdot S_i \cdot P_{oi} \quad (6.9)$$

$$= F_s - L_c,$$

where  $F_s$  = collision rate of impinging neutrons ( $s^{-1}$ ),  
 $L_c$  = leak of collided neutrons ( $s^{-1}$ ).

The quantity  $\Delta L/\sqrt{E}$ , indicating the change in detector response to be expected, can be computed for each small group and summed up over the whole spectrum. For the sample UO<sub>2</sub>14, we find

CHI (7.5 - 0.8 eV, 293 K) = 3.344	b/eV <sup>1/2</sup>
CHI ( " " , 793 K) = 3.402	"
Δ	0.058
ΔL/√E ( " " , 293 K) = 3.319	n/s.eV <sup>1/2</sup>
ΔL/√E ( " " , 793 K) = 3.377	"
Δ	0.058

There is only a small discrepancy at least for the absorption in the first resonance. From this, and a number of similar computations it seems likely that the measurement of leakage decrease from the sample is a proper way to determine the neutron absorption therein. Fig. 6.12 illustrates the phenomena. In fact in this method we have in principle a way to determine theoretically the moderation correction as is needed for  $\text{UO}_2$ . This requires, however, a detailed knowledge of the neutron spectrum around the cadmium cut-off energy, which is a troublesome point. We therefore preferred to apply the experimental correction (sect. 2.2.2).

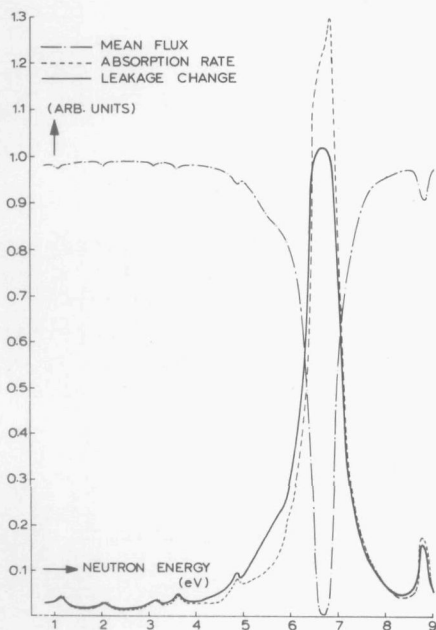


Fig. 6.12.  
Mean flux, absorption rate  
and leakage change for  $\text{UO}_2$

#### 6.5.2. On possible electrical errors

The signal of the oscillator main ionisation chamber is amplified and filtered after which it passes through a special gate and is then integrated. One could imagine that during this process some systematic error is introduced, which might influence the results. This is controlled by using a different independent system of data acquisition, based on the multiscaler analysis of the digitalised signal (see section 2.2.1, Fig. 2.11).

An increasingly noise-free representation of the dips in the main ionisation chamber current is built up in the analyser memory during the oscillations (Fig. 2.12). The surface of the dips, being a measure for the absorption in the samples, can be numerically determined from the known contents of the analyser channels. The method has no obvious disadvantages compared with the analogous integrating that was normally applied, except that of the handling of a comparatively large amount of data. This disadvantage can be overcome by the use of an on-line computer.

With the analyser method the Doppler measurement on U8 was repeated, the result of which showed no significant difference to the original measurements. It was concluded that no systematic errors exist in the signal treatment. This could also be expected from the linearity of the graphs in Fig. 6.3 and 6.4.

### 6.5.3. *On possible anisotropy effects*

Anisotropy in the neutron flux or the detector efficiency may lead to systematic errors in the interpretation of the experimental results. The effects disappear when spherical absorbers are used. Even an appreciable decrease of rod length would be significant in this respect. We oscillated a UO<sub>2</sub>20 rod with a length of 20 instead of 90 mm. The results were:

$$\begin{aligned} O/P &= 0.233 \\ \Delta CHI_{300-873} &= (4.5 \pm 0.6)\% \end{aligned}$$

Knowing that  $\frac{S}{M} = 0.282 \text{ cm}^2 \text{ g}^{-1}$  and that the computation result for N.V. CHI is  $0.76 \text{ cm}^2 \text{ eV}^{-\frac{1}{2}}$ , we can see from Figs. 6.4 and 6.11 that these results agree with the other measurements. The conclusion may be drawn that in our experiments anisotropy effects did not have a significant influence on the results.

### 6.6. *Discussion of the results and conclusions*

For the room-temperature measurements no exceptions from a good agreement between theory and experiment have been found. It is concluded that the codes are applicable for the experimental situation, although in the case of ERIDEL care must be taken with several approximations at low-energy.

In the Doppler measurements an encouraging reproducibility in

comparison with reference experiments could be realised. Nevertheless error margins remained to be considerable in both experimental and computed results. The experimental values are generally within the computed predictions: RIFF RAFF' on the lower and ERIDEL on the upper side. Several reasons for these deviations between the code results have been discussed in sect. 4.3.2.1 and 4.3.2.2. In ERIDEL the temperature-independent computation of the Goldstein-Cohen parameter and the Bell-factor will give rise to an overestimation of the Doppler effect. In RIFF RAFF' the oversimplified description of the space-dependence of the flux might have the opposite effect. A distinct preference for one of the codes can not be determined from the measurements. In these considerations the appreciable contribution to the error margins in the code predictions resulting from nuclear data uncertainties must also be recognised. It has to be emphasised that ERIDEL as well as RIFF RAFF' agree with the experimental results within the respective error limits.

From the work described here two conclusions may be drawn:

1. the local pile oscillator is a useful tool for neutron-absorption measurements in the epithermal energy range;
2. the existing numerical codes for resonance absorption give a reliable description of low-energy resonance absorption, but several approximations limit the accuracy of Doppler-effect computations.

#### 6.7. *Possible future work*

The local epithermal pile oscillator is an instrument which can be used for the study of special resonance phenomena at relatively low neutron energies. The reproducibility is sufficient for a comparison with computer code results to lead to a better understanding as to where the application of certain approximations in the codes is allowed. In this thesis, some experiments in this respect were described. We might further consider investigations on moderated absorber rods, resonance interference effects, more complicated geometries, etc.

As has already been mentioned (sect. 1.1), the most desirable expansion of the scope of the measurements would, however,

be realised by changing the spectrum characteristics such that *Doppler effects in spectra of fast and intermediate reactors* can be studied. This is even more desirable as the reliability of nuclear data and therefore of computer results decreases for these spectra. The main problem that has to be solved before these measurements can be carried out is that of the *unfavourable energy dependence in the response of the boron-lined ionisation chambers*. This problem could be solved by using global oscillation (reactivity measurements), which technique, however, does not have the advantages of the relatively simple local-oscillation method. Another possibility is that of designing a more suitable local neutron detector. Some possibilities in this respect will be mentioned.

#### 1. proton recoil detection

The efficiency of a large proton recoil detector depends on the scattering cross-section of hydrogen, which only slightly varies up to high neutron energies. Therefore the efficiency of such a counter is of the same order of magnitude up to several hundredths of keV's. Below about 5 keV, however, the counter is no longer useful because the discrimination for gamma rays becomes problematic.

#### 2. fission chamber detection

A second possibility is the use of a fission chamber, the temperature of which is oscillated. As the energy release in a fission event is practically independent of the kinetic energy of the neutrons causing fission, this method can be used to determine Doppler effects in fission. An associated problem is that the fissionable material must be in the form of a thin coating.

#### 3. oscillation in a flux bundle

The sample is oscillated in a flux bundle of neutrons with the desired spectrum. Having passed through the oscillation region the neutrons are detected in a "black" detector: a  $B_4C$ -slab, for example, with scintillation tank. In this case the neutron-scattering effects - which will probably occur - are disadvantageous.

#### 4. neutron detection with a subcritical assembly

A neutron detector with the desired response is created by an ionisation chamber which is placed in a subcritical assembly where the effective multiplication constant, the fast-neutron non-leakage probability and the resonance escape probability are not far from 1. The assembly acts as an amplifier amplifying the neutron-source intensity. The amplification will be more or less independent of the source-neutron energies.

Whether these detecting methods are useful or not can be proved only by further experimental investigations and/or calculations.



## APPENDIX

In this appendix some flux-and collision density plots are shown, which resulted from computations. Although these do not have a direct bearing on the foregoing, they illustrate characteristic phenomena in resonance absorption.

In Fig. A1 the depression of the mean neutron flux around the first  $^{238}\text{U}$ -resonance is shown for two natural uranium rods, computed with RIFF RAFF'. The small but more frequent  $^{235}\text{U}$ -resonances can be clearly distinguished from the 6.68 eV  $^{238}\text{U}$ -resonance. The 10.25 eV  $^{238}\text{U}$ -resonance is, for this isotope, extremely small. Perhaps it is a low-energy p-wave resonance (47).

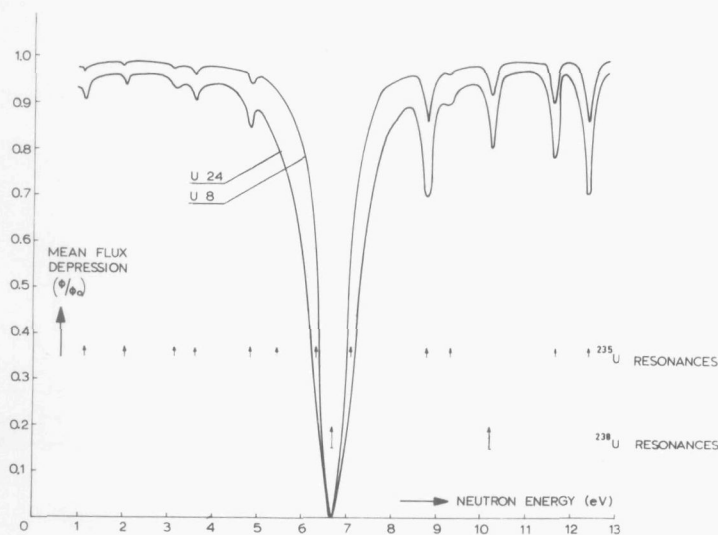


Fig. A1. Flux plots for two natural uranium rods at 293 K (RIFF RAFF')

In Fig. A2 the interference between two  $^{232}\text{Th}$ -resonances can be seen. The computations, again made with RIFF RAFF', are summarized in Table A1.

The following resonance parameters were used:

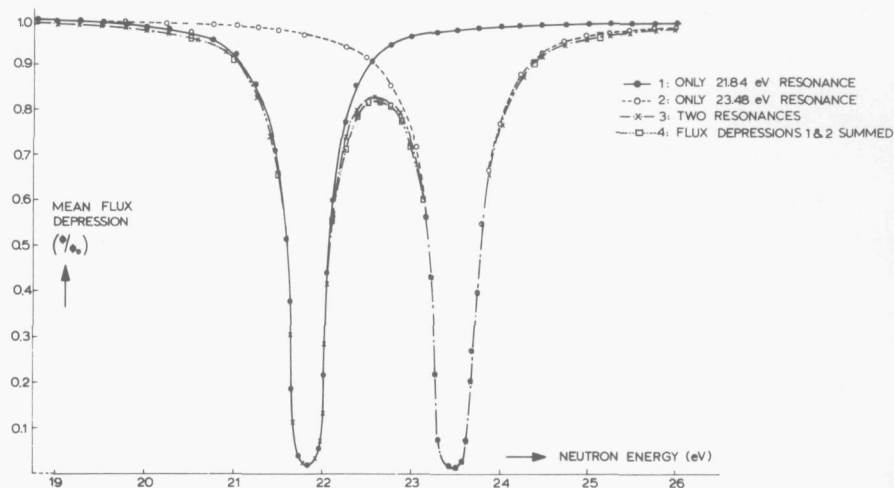


Fig. A2. Flux plots for Th10 at 293 K (RIFF RAFF')

$$E_R = 21.84 \text{ eV}, \Gamma_\gamma = 0.030 \text{ eV}, \Gamma_n = 0.0024 \text{ eV};$$

$$E_R = 23.48 \text{ eV}, \Gamma_\gamma = 0.030 \text{ eV}, \Gamma_n = 0.0040 \text{ eV}.$$

Table A1. Partial resonance integrals from 15 to 30 eV for Th10

	293 K	793 K	temp. effect
21.84 eV single res.	1.562 b	1.738	
23.48 eV single res.	1.761	1.911	
	----- +	----- +	
	3.323	3.649	9.8%
interfering resonances	3.206	3.417	9.7%
interference effect	3.7%	3.8%	

In Fig. A3 the typical flux rise accompanying strong scattering resonances is presented for the 190 eV-resonance of  $^{238}\text{U}$  in a U8 rod. The parameters of this resonance are:

$$E_R = 190 \text{ eV}, \Gamma_\gamma = 0.0226 \text{ eV}, \Gamma_n = 0.149 \text{ eV}.$$

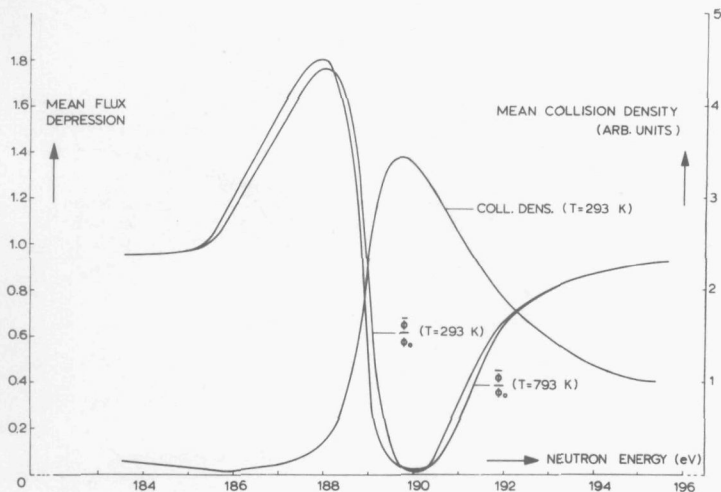


Fig. A3. The 190 eV  $^{238}\text{U}$ -resonance in U8 (RIFF RAFF')

The neutron flux reaches its maximum at an energy which is about 0.9 eV lower than that of the top of the collision density. This has to be compared with a mean energy loss per collision of  $\frac{E(1-\alpha)}{2} \approx 1.6$  eV. The flux rise is greatly favoured by the interference between potential and resonance scattering, which reduces the scattering cross-section at energies near the flux top.

Finally in Fig. A4, some results for the 36.7 eV  $^{238}\text{U}$ -resonance in a 10 mm diameter rod are shown at 293 K and 793 K (see also sect. 4.3, Table 4.2). In the ERIDEL as well as in the RIFF RAFF' computation the interference between potential and resonance scattering is disregarded. With the ERIDEL code the flux dip becomes essentially symmetrical, resulting in a too low flux in the left wing of the resonance. Doppler broadening is clearly visible, due to the logarithmic divided ordinate. It is not advisable to attach too much importance to details of the temperature dependence in the collision density, for instance, as the computation model of ERIDEL in particular is rather approximate, as has been discussed already.

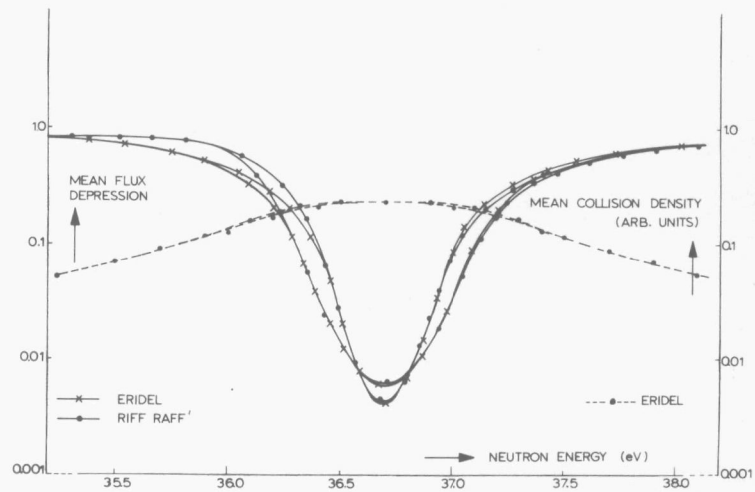


Fig. A4. RIFF RAFF' and ERIDEL results for the 36.7 eV  $^{238}\text{U}$ -resonance in U10 at 293 K and 793 K

#### REFERENCES

- (7) W.C. Redman (Chairman), "Proc. of the Int. Conf. on Fast Critical Experiments and their Analysis", ANL 7320, page 57 (W.G. Davey) ANL (1966).
- (2) E. Creutz et al., J. Appl. Phys. 26, 257 (1955).
- (3) E. Creutz et al., J. Appl. Phys. 26, 271 (1955).
- (4) E. Creutz et al., J. Appl. Phys. 26, 276 (1955).
- (5) E.P. Wigner et al., J. Appl. Phys. 26, 260 (1955).
- (6) L. Dresner, "Resonance absorption in reactors", Pergamon Press, Oxford (1960).
- (7) J.R. Stehn et al., BNL 325, Sec. Edition, Suppl. no. 2, Vol III (1965).
- (8) E. Hellstrand and G. Lundgren, Nucl. Sci. Eng. 12, 435 (1962).
- (9) W. Pettus et al., BAW - 1286, B&W (1963).
- (10) W.K. Foell, IDO - 16986, Phillips Petr. Co. (1965).
- (11) P.G.F. Moore, S.K. Pattenden and R.B. Tattersall, Reactor Sc. and Technol., 16, p. 335 (1962).
- (12) A.J. Goodjohn and G.C. Pomraning (eds), "Reactor physics in the resonance and thermal regions", Vol II, page 151 (E. Hellstrand), M.I.T. Press, Cambridge, U.S.A. (1966).
- (13) A.L. Dekker and H.R. Kleijn, Nucl. Instr. and Meth. 55, 87 (1967).
- (14) J.I. Hoover et al., Phys. Rev. 74, 864 (1948).
- (15) V.G. Small and A.H. Spurway, AERE RP/R 1439, UKAEA (1956).
- (16) W.J. Price, "Nuclear radiation detection", McGraw-Hill Book Company, New York (1964).
- (17) H. Goldstein et al., EANDC-12 "U" (1961).

- (18) A.L. Dekker and A.H. Koetsier, Nucl. Instr. and Meth. 62, 301 (1968).
- (19) W. Epprecht, "Werkstoffkunde der Kerntechnik", Birkhäuser Verlag, Basel (1961).
- (20) A.L. Dekker and J.L. Grashuis, Nukleonik 10, 5, 278 (1967).
- (21) J.L. Grashuis, A.L. Dekker and H.R. Kleijn, Trans. Am. Nucl. Soc. 11, 2 (1968).
- (22) J. Julien et al., Nucl. Phys. 76, 391 (1966).
- (23) M.M. Levine, Nucl. Sci. Eng. 16, 271 (1963).
- (24) J.E. Olhoeft et al., Conf. on safety, fuels and core design in large fast power reactors, ANL (1965).
- (25) G. Smith et al., Nucl. Sci. and Eng. 8, 449 (1960).
- (26) W.H. Arnold and R.A. Dannels, Trans. Am. Nucl. Soc. 3, No. 1, 229 (1960).
- (27) G.F. Kuncir, GA-2525, General Atomic (1961).
- (28) L.W. Nordheim, GA-2527, General Atomic (1961).
- (29)<sup>\*</sup> A.H. Koetsier, "ZUT code rapport", THD-H-RF-120, THD (1968).
- (30)<sup>\*</sup> H.M. Sumner, AEEW-R 323, UKAEA (1964)  
and  
A.L. Dekker and F. de Kruijf, "ERIC-II-Delft", THD-H-RF-125, THD (1967).
- (31) L.M. Case et al., "Introduction to the theory of neutron diffusion", U.S. Gov. Printing Off., Wash. D.C. (1953).
- (32) R. Goldstein and E.R. Cohen, Nucl. Sci. Eng. 13, 132 (1962).
- (33) V.W. Nather and L.W. Nordheim, GA-2460, General Atomic (1961).
- (34) H.J. Amster, Nucl. Sci. and Eng. 11, 343 (1961).
- (35) J.H. Ferziger et al., GEAP 3923, General Electric Company (1962).
- (36) D.M. O'Shea and H.C. Thacher, Jr, Trans. Am. Nucl. Soc. 6, No. 1, 36 (1963).
- (37)<sup>\*</sup> F. de Kruijf, "ERIDEL-1. An improved analytical calculation of resolved resonance integrals", THD-H-RF-119, THD (1968).
- (38) G.I. Bell, LA-2327, Los Alamos University (1959).
- (39) D.C. Leslie et al., Nucl. Sci. Eng. 22, 78 (1965).
- (40) C.N. Kelber, Nucl. Sci. Eng. 22, 244 (1965).
- (41) P.H. Kier, Nucl. Sci. Eng. 26, 230 (1966).
- (42) K.B. Cady and M. Clark, Nucl. Sci. Eng. 18, 491 (1964).

- (43) E.E. Lewis, "A Boltzmann integral equation treatment of resonance absorption in reactor lattices", Ph.D. Thesis, U. of Illinois (1965).
- (44) F.L. Fillmore and B.D. O'Reilly, NAA-SR-MEMO-8889, Atomic International (1963).
- (45) F. de Kruijf, personal communication (1968).
- (46) A.J. Goodjohn and J.C. Pomraning (eds), "Reactor physics in the resonance and thermal regions", Vol II, page 395 (J.R. Askew), M.I.T. Press, Cambridge, U.S.A. (1966).
- (47) J.J. Schmidt, KFK 120 (1966).
- (48) W.K. Foell and W.J. Connolly, Nucl. Sci. and Eng. 26, 399 (1966).
- (49) L.I. Tirèn and J.M. Jenkins, AEEW-R 163, UKAEA (1962).
- (50) M. Asghar, Nucl. Phys. 76, 196 (1966).
- (51) B.R. Seghal, Nucl. Sci. Eng. 27, 95 (1967).
- (52) L.E. Strawbridge, Nucl. Sci. Eng. 27, 142 (1967).
- (53) T.J. Thompson and J.G. Beckerly (eds), "The technology of nuclear reactor safety", Vol I, Chapter 4 (L.W. Nordheim), page 205, M.I.T. Press, Cambridge, U.S.A. (1964).
- (54) B.L. Palowitch and F.S. Frantz, Jr, Nucl. Sci. Eng. 15, 146 (1963).
- (55) W. Pettus et al., BAW-1244, B&W (1962); and private communication to Hellstrand (72) (1965).
- (56) E. Hellstrand et al., Nucl. Sci. Eng. 8, 497 (1960).
- (57) R.M. Pearce, J. Nucl. Eng. A, 11, 136 (1960).
- (58) G.W. Rodeback, NAA-SR-1641, North American Aviation (1956).
- (59) A.W. Solbrig, Jr, IDO-17120, Phillips Petr. Co. (1965).
- (60) A.J. Goodjohn and J.C. Pomraning (eds), "Reactor physics in the resonance and thermal regions", Vol II, page 85 (M.M. Levine), M.I.T. Press, Cambridge, U.S.A. (1966).
- (61) N.P. Baumann and D.J. Pellarin, Trans. Am. Nucl. Soc. 7, No. 1, 27 (1964).
- (62) J. Hardy, Nucl. Sci. Eng. 22, 121 (1965).
- (63) G.C. Hanna and W.H. Walker, EANCD (Can.)-20 "L" (1963).
- (64) L.J. Esch et al., Trans. Am. Nucl. Soc. 7, No. 1, 78 (1964).
- (65) M.R. Bhat and R.E. Chrien, Phys. Rev. 155, 1362 (1967).
- (66) J. Hardy et al., Nucl. Sci. Eng. 14, 358 (1962).

- (67) R. Froelich and K. Ott, Nukleonik 8, 137 (1966).
- (68) E.R. Cohen, Gen. Conf. 1955, P/611, Vol V, page 405.
- (69) R.B. Tattersall et al., J. Nucl. Eng. A, 12, 32 (1960).
- (70) H.R. Kleijn, "On the determination of microscopic reactor parameters using exponential assembly", PhD Thesis, Delft Technol. Univ. (1965).

\*The THD-reports mentioned in this reference list can be obtained from the Reactor Physics Group, Reactor Institute, Delft, The Netherlands.

LIST OF ABBREVIATIONS

AEEW	Atomic Energy Establishment Winfrith
AI	Atomics International
ANL	Argonne National Laboratory
APDA	Atomic Power Development Associates
BNL	Brookhaven National Laboratory
BNWL	Battelle-Northwest Laboratory
B & W	Babcock and Wilcox
EANDC	European-American Nuclear Data Committee
GA	General Atomic
GE	General Electric
HOR	Hoger Onderwijs Reactor
KFK	Kernforschungszentrum Karlsruhe
LASL	Los Alamos Scientific Laboratory
MIT	Massachusetts Institute of Technology
NAA	North American Aviation
THD	Technische Hogeschool Delft (Delft University of Technology)
UKAEA	United Kingdom Atomic Energy Authority
W	Westinghouse



## SUMMARY

This thesis contains an analysis of the usability of a "local reactor oscillator" for the measurement of epithermal-neutron absorption, the so-called resonance absorption, in fissionable and fertile materials. The principle of the local reactor oscillator is that the magnitude of the local depression of the neutron flux as "transported" by a moving absorber is correlated with the neutron absorption in the sample. Experimental investigations concerning resonance absorption have hitherto been carried out mainly by activation methods and with reactivity analysis, which methods are discussed in Chapter 1.

The reason for initiating the investigations, apart from the continued interest in resonance absorption phenomena in thermal systems, was mainly the importance of the temperature dependence of the resonance absorption - the nuclear Doppler effect - in neutron spectra characteristic for fast and intermediate reactors. The theoretical and experimental knowledge accumulated in the investigations described will be a basis for extrapolating this or other methods towards measurements in media with the desired spectra.

A number of computer programs in the field of resonance absorption was developed, partly by transcription of existing FORTRAN versions into ALGOL, in order to guide the experimental work theoretically. Since it was shown during the experiments that with the measuring equipment, the "L(ocal) O(scillator) in the E(pithermal) R(egion)", a sensitive detection of resonance absorption at room temperature was possible, whilst the course of dependence on the temperature could be traced with reasonable accuracy, it became possible to extend the work towards an experimental verification of the available computer codes.

The major activities can be summarised as follows:

1. The design and building of a local oscillator in the thermal column of the Hoger Onderwijs Reactor at Delft (sect. 2.1) and the calibration of it by means of gold-lead rods (Chapter 3).

2. The determination of the epithermal-neutron spectrum in the oscillator channel with very thin foils obtained by vacuum evaporation and consisting of nuclides with pronounced resonances at specific neutron energies (sect. 2.3, 2.4). Single foils as well as multi-material ("plural") foils were used.
3. The development of a number of computer programs in the field of epithermal-neutron absorption. The codes ERIC-II (Sumner, U.K.), ZUT (Nordheim and Kuncir, U.S.A.) and RIFF RAFF (Kier, U.S.A.) were transcribed into ALGOL - to adapt them to our TR-4 computer - and were further elaborated resulting in ERIDEL and RIFF RAFF' (sect. 4.1, 4.2). The codes were compared with each other (sect. 4.3).
4. The computation of resonance integrals and Doppler coefficients for neutron absorption in  $^{238}\text{U}$ , natural uranium metal,  $^{238}\text{UO}_2$ , natural uraniumdioxide and thorium metal and the comparison of the results thereof with data from literature sources (sect. 5.1, 5.2, 5.3). Furthermore the recomputation of these values taking into account the efficiency characteristic ( $1/\sqrt{E}$ ) of the detector (sect. 6.1).
5. The determination of the oscillator results at room temperature and for a temperature rise from 300 up to 900 or 1100 K for three series of sample rods (natural uranium, thorium and natural uraniumdioxide) each set consisting of 6 to 8 specimens (Chapter 6).

The results of the investigations can be summarised as follows:

1. The epithermal-neutron spectrum in the oscillator channel can be described by

$$\phi(E) \div 1/E^{0.99 \pm 0.04} .$$

2. The computed resonance integrals agree with those reported in the literature to within the respective error limits. As to the Doppler coefficients a difference exists between the ERIDEL and RIFF RAFF' results: the former are somewhat higher than the latter. For neither code, however, a clear discrepancy with the reference

data could be observed beyond the generally appreciable error margins. No data suitable for comparison could be traced for the computations concerning natural uranium metal and natural uranium dioxide. Some results were:

$$U : RI = 5.8 + 28.1 \sqrt{\frac{S}{M}} \text{ barns } (\pm 5\%) \quad \beta_+ = (0.36 + 0.50 \frac{S}{M}) 10^{-2} K^{-\frac{1}{2}} (\pm 15\%)$$

$$UO_2 : RI = 7.9 + 28.6 \sqrt{\frac{S}{M}} \text{ barns } (\pm 5\%) \quad \beta_+ = (0.38 + 0.53 \frac{S}{M}) 10^{-2} K^{-\frac{1}{2}} (\pm 15\%)$$

3. For the absorber rods studied, a simple linear relationship could be established between the observations with the local oscillator and the computed resonance integrals weighed with the detector efficiency.
4. The measuring results of the oscillator at room temperature showed a good agreement with the computed values. As to the Doppler effect our measurements too gave values between the predictions of both codes. Because the experimental results as well as the computations have error margins of 10 to 20%, no disagreements were noticed.

For high-energy resonances the code results show less and less discrepancy thanks to the fact that several approximations are of an increasing degree of correctness. The phenomenon can be seen from our computations on thorium metal, which nuclide has a lowest resonance at an energy above 20 eV. This means that as long as the suppositions related to the description of the cross-sections with the one-level Breit-Wigner formula are justified both codes in principle are applicable in the case of fast spectra.

In conclusion it is stated that the usability of the resonance absorption programmes considered - which are representative of what is available in this field, and applicable for non-1/E spectra - is confirmed by the experiments described. In order to increase the understanding of the exact influence of specific approximations in the codes, the Monte Carlo method ("experiment in the computer") has to be included in the investigations. The local pile oscillator has proved to be a useful tool for measurements concerning neutron absorption at epithermal

energies. An extension of this investigation to different neutron spectra may be considered.

## SAMENVATTING

Dit proefschrift bevat een analyse van de gebruiksmogelijkheden van een "lokale reactoroscillator" voor het verrichten van metingen op het gebied van de absorptie van epithermische neutronen, de zogenaamde resonantie-absorptie, in splijt- en kweekstoffen. Bij een lokale reactoroscillator wordt de omvang van de plaatselijke depressie van de neutronenflux zoals die door een bewegende absorber wordt "meegevoerd", gecorreleerd aan de absorptie van neutronen in het monster. Het experimentele onderzoek aan resonantie-absorptie vond tot op heden slechts plaats met behulp van activeringsmethoden of reactiviteitsanalyse, welke bestaande methoden in Hoofdstuk 1 besproken worden.

De aanleiding tot het verrichten van het onderzoek was, behalve de nog steeds bestaande belangstelling voor resonantie-absorptie in thermische systemen, in het bijzonder het belang van de temperatuurafhankelijkheid van de resonantie-absorptie - het nucleaire doppler effect - in neutronenspectra kenmerkend voor snelle en intermediaire reactoren. De theoretische en experimentele kennis zoals die bij het onderhavige onderzoek werden verzameld, vormen een basis waarop kan worden voortgebouwd bij het extrapoleren van deze of andere methoden naar media met de gewenste karakteristieken.

Ten einde het experiment theoretisch te begeleiden, werd een aantal rekenprogramma's op het gebied van resonantie-absorptie ontwikkeld, deels door omzetting van bekende FORTRAN versies in ALGOL. Bij het experimentele werk bleek, dat met de ontwikkelde meetopstelling, "L(ocal) O(scillator) in the E(pithermal) R(egion)" gedoopt, een gevoelige detectie van resonantie absorptie bij kamertemperatuur mogelijk is, terwijl tevens de temperatuurafhankelijkheid ervan met een redelijke mate van nauwkeurigheid gevolgd kan worden. Daarmee werd het mogelijk verder te gaan, en te trachten de beschikbare codes experimenteel te verifiëren.

De voornaamste activiteiten die aan de orde kwamen, kunnen als volgt puntsgewijs worden samengevat:

1. Het ontwerp en de bouw van een geschikte opstelling in de thermische kolom van de Hoger Onderwijs Reactor (sect. 2.1), en de calibratie hiervan door middel van goud-lood

staafjes (Hfst. 3).

2. Het bepalen van het epithermisch neutronenspectrum in het oscillatorkanaal met behulp van uiterst dunne, opgedampte, folies van nucliden met geprononceerde resonanties bij bepaalde neutronenenergieën (sect. 2.3, 2.4). Zowel het gebruik van enkel- als van meervoudige folies kwam aan de orde.
3. Het ontwikkelen van rekenprogramma's op het gebied van de epithermische neutronenabsorptie. Hiertoe werden de codes ERIC-II (Sumner, U.K.), ZUT (Nordheim en Kuncir, U.S.A.) en RIFF RAFF (Kier, U.S.A.) in ALGOL omgezet - zodat ze op de TR-4 computer van de T.H.-Delft gebruikt konden worden - en verder uitgewerkt tot ERIDEL en RIFF RAFF' (sect. 4.1, 4.2). De resultaten van de codes werden onderworpen aan onderlinge vergelijking (sect. 4.3).
4. Het berekenen van de resonantie-integralen en dopplercoefficiënten voor absorptie van neutronen in  $^{238}\text{U}$ , natuurlijk uranium metaal,  $^{238}\text{UO}_2$ , natuurlijk uraniumdioxide en thorium metaal, en het vergelijken van de verkregen resultaten met literatuurgegevens (sect. 5.1, 5.2, 5.3). Voorts het herberekenen van deze waarden met verdiscontering van de efficiëntie karakteristiek ( $1/\sqrt{E}$ ) van de detector (sect. 6.1).
5. Het waarnemen van de oscillator resultaten bij kamertemperatuur en voor temperatuurstijging van 300 tot 900 à 1100 K, voor een drietal series proefstaafjes (natuurlijk uranium, thorium en natuurlijk uraniumdioxide), elk bestaande uit 6 tot 8 exemplaren (Hfst. 6).

De resultaten die het werk heeft opgeleverd kunnen in de volgende punten worden samengevat:

1. Voor het epithermisch neutronenspectrum in het oscillatorkanaal geldt

$$\phi(E) \div 1/E^{0.99 \pm 0.04}$$

2. Van de berekende resonantie-integralen bleek dat deze binnen de foutenmarges veelal in overeenstemming waren met de uit de literatuur bekende referentiegegevens. Voor wat betreft de doppler coëfficiënten bestond enig

verschil tussen de ERIDEL en de RIFF RAFF' resultaten, waarbij de eerste aan de hoge, de tweede daarentegen aan de lage kant lagen. Dit echter zonder dat voor een van beide van een duidelijke discrepantie met de, veelal van ruime foutenmarges voorziene, referentiegegevens sprake was.

Voor de berekeningen betreffende natuurlijk uranium metaal en natuurlijk uraniumdioxide was geen referentie materiaal aanwezig. Enkele resultaten hiervan luiden:

$$U : RI = 5.8 + 28.1 \sqrt{\frac{S}{M}} \text{ barns } (\pm 5\%) \quad \beta_+ = (0.36 + 0.50 \frac{S}{M}) 10^{-2} K^{-\frac{1}{2}} (\pm 15\%)$$

$$UO_2 : RI = 7.9 + 28.6 \sqrt{\frac{S}{M}} \text{ barns } (\pm 5\%) \quad \beta_+ = (0.38 + 0.53 \frac{S}{M}) 10^{-2} K^{-\frac{1}{2}} (\pm 15\%)$$

3. Tussen de meetresultaten met de oscillator en de met de detectorefficiëncy gewogen berekende resonantie-integralen kon, voor de beschouwde absorber staven, een eenvoudig lineair verband worden vastgesteld.
4. De meetresultaten met de locale oscillator bij kamertemperatuur kwamen goed overeen met de berekende waarden. Wat betreft het doppler effect bleek dat ook onze metingen zich tussen de door de beide rekencodes aangegeven waarden bewogen. Doordat zowel de experimentele resultaten als de berekeningen foutenmarges van 10 à 20% bevatten, kan van overeenstemming gesproken worden tussen de metingen en elk van beide codes.

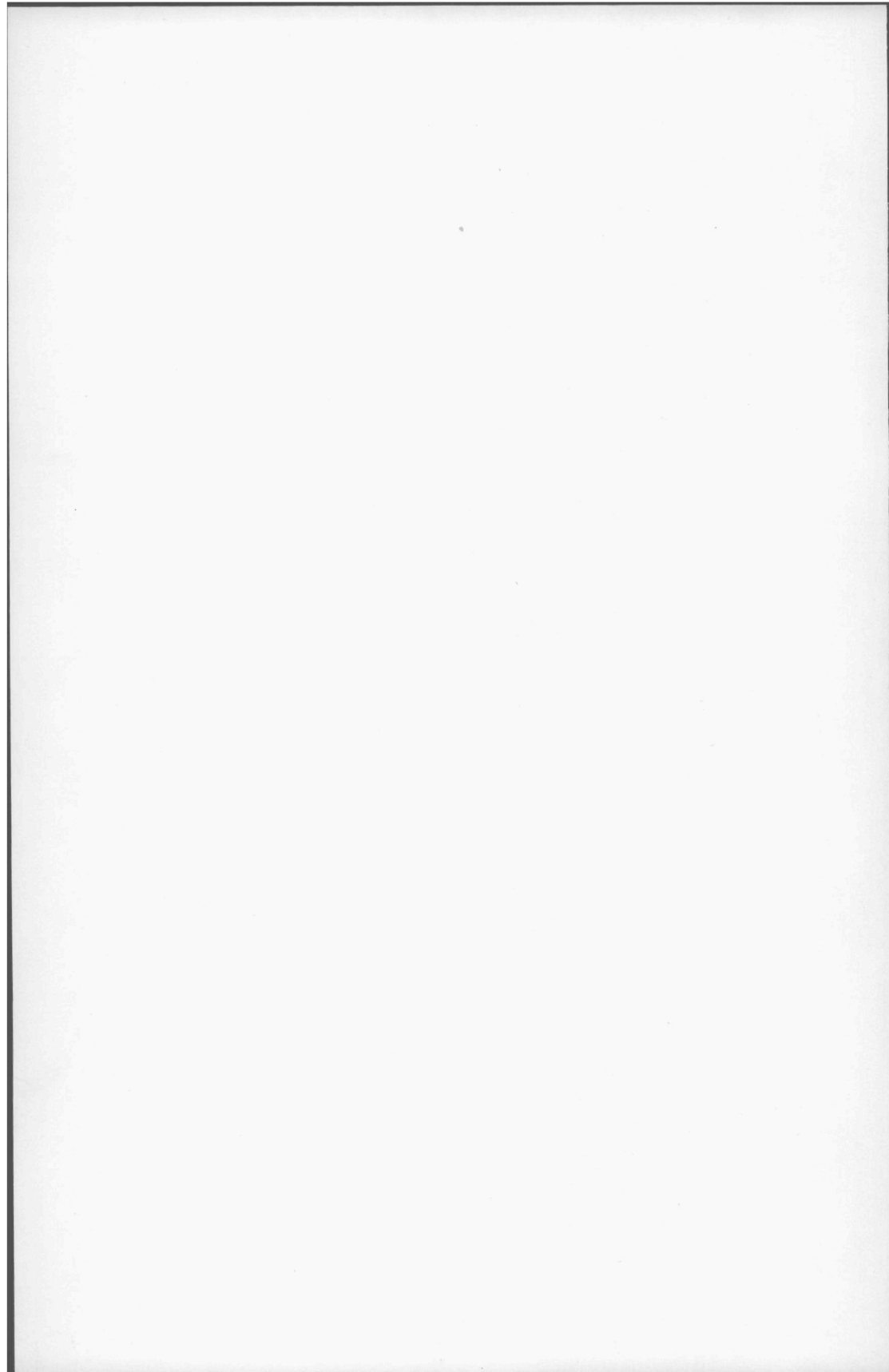
Bij resonanties van hogere energie naderen de code uitkomsten elkaar, doordat diverse benaderingen beter opgaan. Dit is reeds zichtbaar aan onze berekeningen aan thorium, in welk metaal de laagst-energetische resonantie nog boven 20 eV ligt. Dit betekent dat, zolang de gemaakte veronderstelling omtrent de beschrijving van de werkzame doorsneden met behulp van één-niveau Breit-Wigner formules opgaat, beide codes in principe geschikt zijn voor berekeningen betreffende "snelle" spectra.

Samenvattend kan worden vastgesteld dat de bruikbaarheid van de onderzochte resonantie-absorptie programma's - die representatief zijn voor wat momenteel op dit gebied bestaat, en ook in niet-1/E spectra toepasbaar - door de verrichte expe-

riminten grotendeels wordt ondersteund. Teneinde het begrip aangaande de invloed van allerlei benaderingen verder te vergroten, heeft het zin bij voortgezet werk naast het experiment en de benaderende theorie ook het "experiment in de rekenmachine", de Monte Carlo methode, toe te passen. De lokale reactoroscillator is een bruikbaar instrument gebouwd voor onderzoek op het gebied van de absorptie van neutronen bij epithermische energieën. Een uitbreiding van het onderzoek naar andersoortige neutronenspectra kan worden overwogen.

#### ACKNOWLEDGEMENTS

A. van Dort, J.L. Grashuis, J.E. Hoogenboom, A.H. Koetsier and F. de Kruijf participated as students in various parts of this study while fulfilling the requirements for the degree of Natuurkundig Ingenieur. Their contribution is gratefully acknowledged. I am furthermore indebted to Dr. H.R. Kleijn and other members of the Reactor Physics Group for valuable discussions and to J. Rooimans for skillful experimental assistance. Finally I like to thank Drs. J.J.M. de Goey for advice in chemical questions, miss H.J. Prins for typing this book and the Direction of the Reactor Institute for making the facilities of their laboratory available to me.



## STELLINGEN

### I

De splitsing van resonantie-absorptie in een oppervlakte- en een volume-component is niet alleen fysisch gezien dubieus, maar leidt bovendien bij lichtvaardig gebruik gemakkelijk tot onjuiste conclusies.

### II

Een toenemend deel van het experimentele werk op natuurkundig gebied zal door simulatie binnen computersystemen kunnen worden gerealiseerd.

### III

Indien de exces resonantie-integraal wordt gedefinieerd als aangegeven door Park, Kim en Yoon, dan geldt niet meer dat de „Westcott parameter” s voor een  $1/v$ -absorber de waarde nul aanneemt.

H. I. Park, I. K. Kim en B. G. Yoon, AERI P/R-6 (1963).

### IV

Als Grant aan Uhrig de suggestie toeschrijft dat er een verband zou bestaan tussen de materiële bollingsfactor in een subkritisch ensemble en de positie van de neutronenbron, gaat hij voorbij aan het feit dat laatstgenoemde auteur in het betreffende artikel duidelijk het tegendeel stelt.

R. M. Grant, Acad. Proefschrift Delft, Stelling V (1964)

R. E. Uhrig, Nucl. Sci. Eng. 5, 120 (1959).

### V

Wanneer de begrippen resonantie-integraal en dopplercoëfficiënt gehanteerd worden, dienen deze betrekking te hebben op de epithermische neutronenabsorptie inclusief de  $1/v$ -bijdrage. Is deze laatste component buitengesloten — het geen overigens zelden zinvol is — dan dient dit in de notatie te worden aangegeven.

H. Goldstein et al., EANDC-12 "U" (1961).

## VI

Rondom een continu op hoog vermogen werkende bassinreactor kunnen onderzoek en onderwijs op het gebied van de reactorfysica zich niet optimaal ontplooiën; daartoe zijn meer flexibele neutronenbronnen nodig.

H. R. Kleijn, Acad. Proefschrift Delft, Stelling VIII (1966).

## VII

De interpretatie die Brinkman geeft van zijn onderzoek aan een Geiger-Müller detector met behulp van de „twee bronnen” methode, kan verbeterd worden. Er zal dan tot een minder sterke daling van de dode tijd bij stijgende telsnelheid moeten worden geconcludeerd.

G. A. Brinkman, Radiochim. Acta 2, 41 (1963).

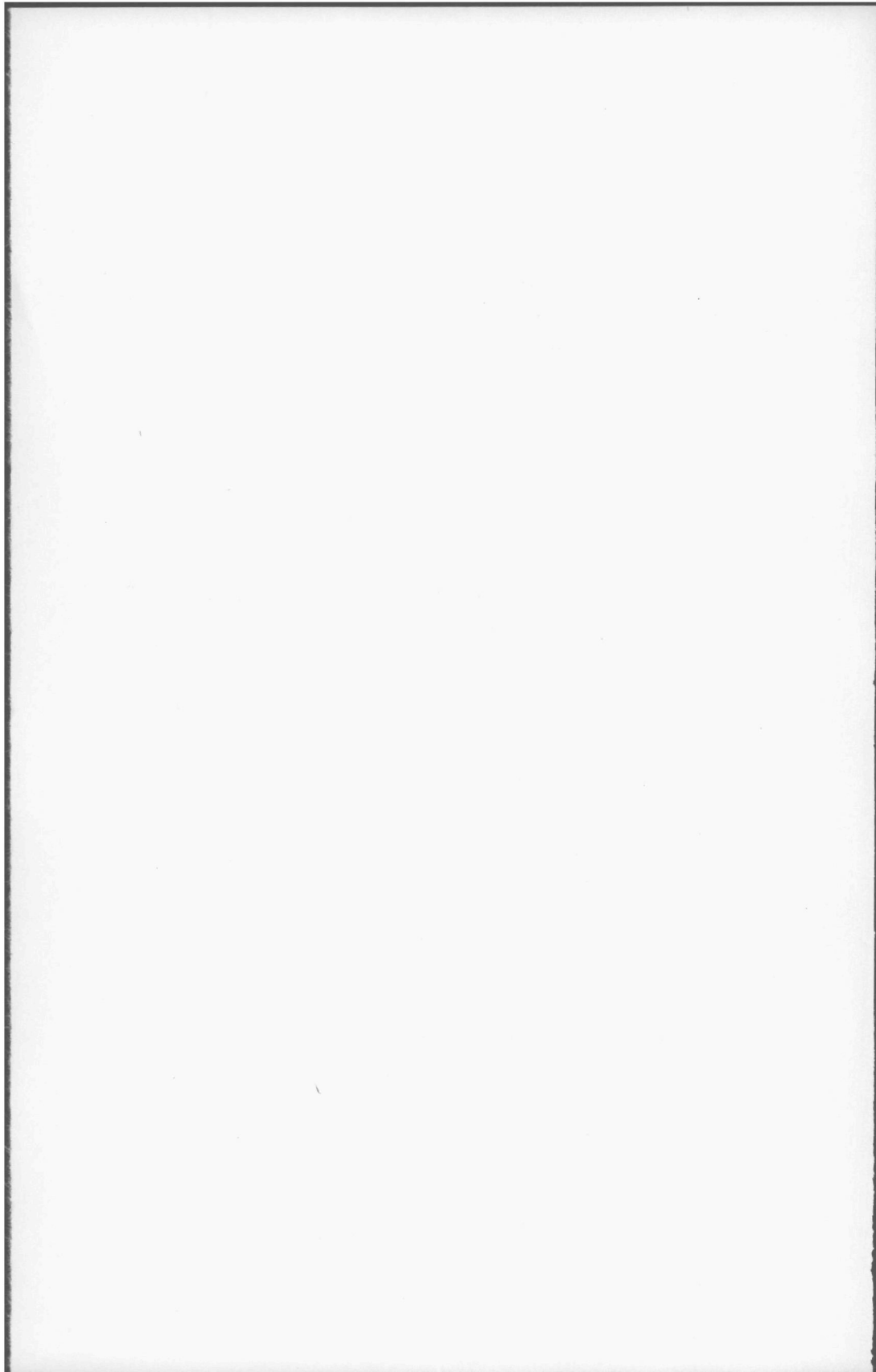
## VIII

Met drie technische hogescholen is voor ons land het optimale aantal van dit soort instellingen in hun huidige vorm bereikt of gepasseerd. Ook het nut van een verdere uitbreiding van het aantal medische faculteiten moet betwijfeld worden.

## IX

Het moet opmerkelijk genoemd worden dat curatoria en besturen van universiteiten en hogescholen, die blijkens vele uitlatingen „democratisering” voorstaan, zich konden en kunnen verenigen met de Gemeenschappelijke Regeling betreffende een onlangs opgericht Interuniversitair Reactor Instituut. In dit besluit immers wordt over enigerlei medebeslissingsrecht van personeel of studenten gezwegen, terwijl zowel het Algemeen Bestuur als het Dagelijks Bestuur in handen van curatoren en senaatsleden worden gelegd die hun mandaat direct of indirect van buiten genoemd instituut hebben verkregen.

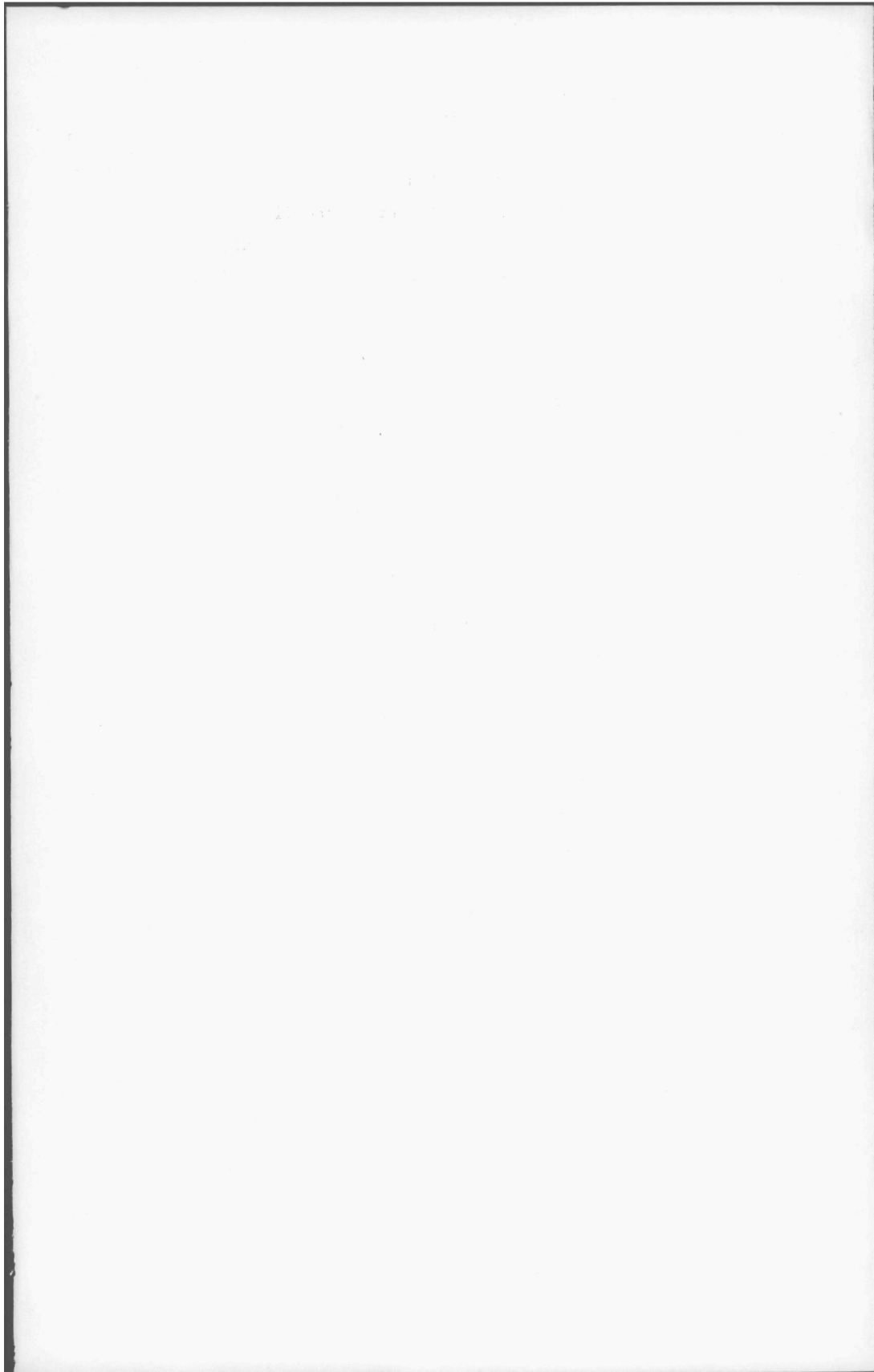
R	reaction rate	$\text{cm}^{-3} \cdot \text{s}^{-1}$
RI	resonance integral	b
$RI_{\infty}$	infinite dilution resonance integral	b
$R_{\text{Cd}}$	cadmium ratio	
r	position vector	cm
S	neutron-source strength	$\text{cm}^{-3} \cdot \text{s}^{-1}$
	surface area	$\text{cm}^2$
SF	strength function	$\text{eV}^{-1/2}$
T	temperature	K
$T_{1/2}$	radioactive half-life	s
u	lethargy	
V	volume	$\text{cm}^3$
x	see Eq. (4.17)	
$\alpha$	$(A-1)^2/(A+1)^2$	
$\beta$	Doppler coefficient	$\text{K}^{-1/2}$
$\beta_+$	Doppler coefficient, including $1/v$ -absorption	$\text{K}^{-1/2}$
$\beta_+^{\text{CHI}}$	chamber Doppler coefficient, including $1/v$ -absorption	$\text{K}^{-1/2}$
$\beta'$	see Eq. (4.21)	
$\Gamma$	level width	eV
$\Gamma_{\text{no}}$	reduced neutron width	eV
$\Delta$	Doppler width of a resonance difference	eV
$\epsilon$	efficiency	
$\theta_{\text{D}}$	Debye temperature	K
$\lambda$	Goldstein-Cohen parameter linear expansion coefficient	$^{\circ}\text{C}^{-1}$
$\xi$	see Eq. (4.17) mean lethargy gain per collision	
$\Sigma(2200)$	macroscopic cross-section for 2200 m/s neutrons	$\text{cm}^{-1}$
$\sigma$	cross-section	b
$\sigma_{\text{ex}}$	$1/\bar{N}$	b

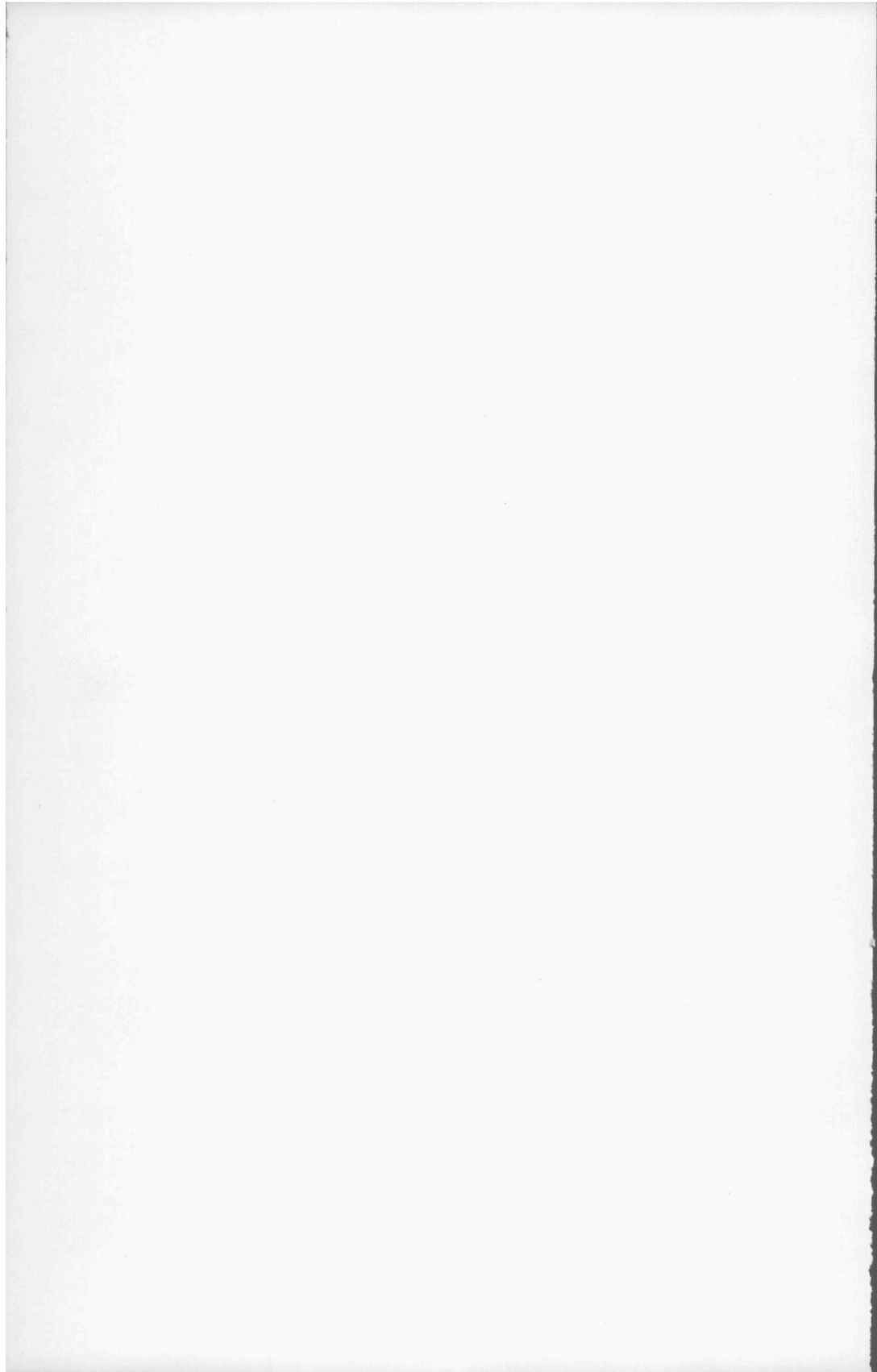


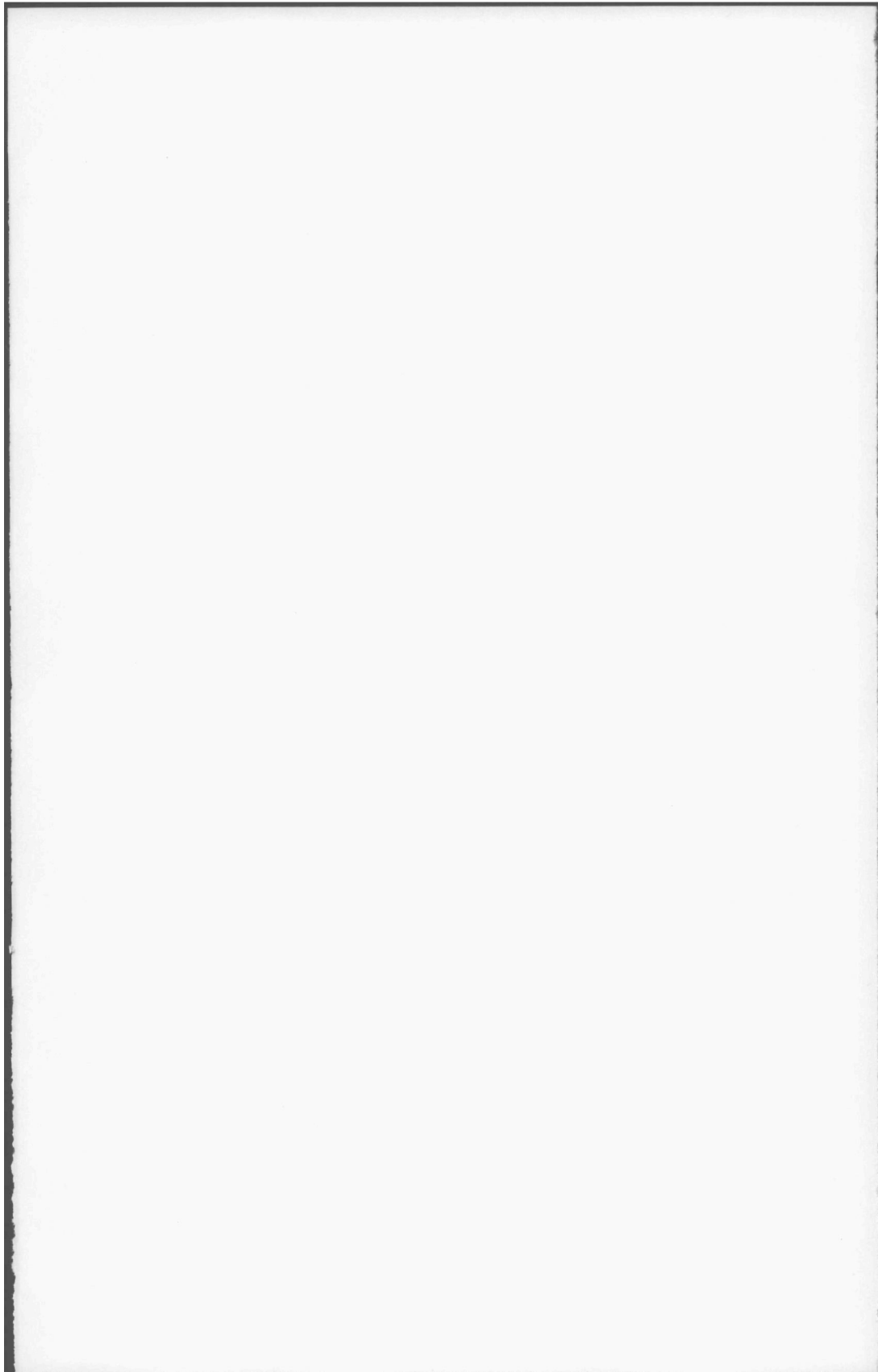
$\sigma_0$	resonance top cross-section	b
$\Phi$	neutron flux	cm <sup>-2</sup> .s <sup>-1</sup>
$\Phi_\infty$	asymptotic neutron flux	cm <sup>-2</sup> .s <sup>-1</sup>
$\chi$	anti-symmetric Doppler-broadened line-shape function	
$\psi$	symmetric Doppler-broadened line-shape function	

*Index*      *refers normally to*

a	absorber/absorption
act	activation
c	collision
f	fission
int	interference
m	moderator/moderation
n	neutron
p	potential scattering
rs	resonance scattering
R	resonance
s	scattering/sample/surface
t	total
th	thermal
$\gamma$	capture
0	absorber region
1	moderator region
$\infty$	infinitely diluted







## LIST OF SYMBOLS

A	mass number	
	activation	$s^{-1}$
$A(\Sigma_{to} \bar{I})$	Bell-function	
a	Bell-factor	
	rod radius	cm
$B_i$	$\pi a^2/(i+1)$	$cm^2$
b	cell radius	cm
CHI	chamber integral	$b.eV^{-1/2}$
$c_n$	surface source-flux coefficient	
$c_{nj}$	source-flux coefficient	cm
$\bar{D}$	mean level spacing	eV
d	diameter	cm
E	energy	eV
$E_{Cd}$	cadmium cut-off energy	eV
F	collision density	$cm^{-3}.s^{-1}$
$F_{Cd}$	cadmium correction factor	
g	statistical spin factor	
$g(T)$	Westcott parameter	
I	nuclear spin quantum number, target nucleus	
J	nuclear spin quantum number, compound nucleus	
$J(\xi, \beta)$	Doppler broadening function	
k	Boltzmann constant	$eV.K^{-1}$
	multiplication factor	
L	neutron-leakage rate	$s^{-1}$
l	length	cm
$\bar{l}$	mean chord length	cm
M	mass	g
N	atom density	$cm^{-3}$
O	oscillator-output voltage	V
P	escape probability	
	reactor power	W

